Three-Dimensional Spherical Modeling of the Mantles of Mars and Ceres: Inference from Geoid, Topography and Melt History

Pavithra Sekhar

Dissertation submitted to the faculty of the Virginia Polytechnic Institute and State University in partial fulfillment of the requirements for the degree of

Doctor of Philosophy
In
Geosciences

Scott D. King, Committee Chair
Robert P.Lowell
Ying Zhou
Erin Kraal

February 7th, 2014
Blacksburg, VA

Keywords: Mars, Ceres, Melt history, Three-dimensional modeling, Geoid and Topography

Three-Dimensional Spherical Modeling of the Mantles of Mars and Ceres: Inference from Geoid, Topography and Melt History

Pavithra Sekhar

ABSTRACT

Mars is one of the most intriguing planets in the solar system. It is the fourth terrestrial planet and is differentiated into a core, mantle and crust. The crust of Mars is divided into the Southern highlands and the Northern lowlands. The largest volcano in the solar system, Olympus Mons is found on the crustal dichotomy boundary. The presence of isolated volcanism on the surface suggests the importance of internal activity on the planet. In addition to volcanism in the past, there has been evidence of present day volcanic activity. Convective upwelling, including decompression melting, has remained an important contributing factor in melting history of the planet. In this thesis, I investigate the production of melt in the mantle for a Newtonian rheology, and compare it with the melt needed to create Tharsis. In addition to the melt production, I analyze the 3D structure of the mantle for a stagnant lithosphere. I vary different parameters in the Martian mantle to understand the production of low or high degree structures early on to explain the crustal dichotomy. This isothermal structure in the mantle contributes to the geoid and topography on the planet. I also analyze how much of the internal density contributes to the surface topography and areoid of Mars. In contrast to Mars, Ceres is a dwarf planet in the Asteroid belt. Ceres is an icy body and it is unclear if it is differentiated into a core, mantle and crust yet. However, studies show that it is most likely a differentiated body and the mantle consists of ice and silicate. The presence of brucite and serpentine on the surface suggests the presence of internal activity. Being a massive body and also believed to have existed since the beginning of the solar system, studying Ceres will shed light on the conditions of the early solar system. Ceres has been of great interest in the scientific community and its importance has motivated NASA to launch a mission, Dawn, to study the planet. Dawn will collect data from the dwarf planet when it arrives in 2015. In my modeling studies, I implement a similar technique on Ceres, as followed on Mars, and focus on the mantle convection process and the geoid and topography. The silicate-ice mixture in the mantle gives rise to a non-Newtonian

rheology that depends on the grain size of the ice particle. The geoid and topography observed for different differentiated scenarios in my modeling can be compared with the data from the Dawn mission when it arrives at Ceres in 2015.

ACKNOWLEDGEMENTS

Firstly I would like to thank my advisor, Scott D. King for his continuous support, motivation, patience, valuable time and guidance all through my PhD. He provided the encouragement and helped direct me towards achieving my goal. I am also grateful to my committee members: Bob P. Lowell, Ying Zhou and Erin Kraal for their immense support and advice. I would like to thank the Geosciences Department for all the support and especially Connie Lowe for her understanding, encouragement and advice.

Special thanks to all my friends who been there for me through good and difficult times and helped maintain my sanity (most of the times) especially Kate Craft, Lindsay Kolbus, Aida Farough, Shvetha Soundararajan, Sushrutha Vigraham, Joshua Valentino, Dave Mercier, Hector Lamadrid, John Wyatt, Ken O'Donnell, John Henley, Kannikha Kolandaivelu, Tannistha Maiti, Karina Cheung, Kristie Dorfler, Tony Giuffre, Sharmin Shamsalsadati, Kaavya Giridhar, Karthik Ganesan, Kashyap Sridhar and Astha Thakur. I would like to express thanks to my friends around the world for their constant encouragement and support, especially Shuba Venkateswaran, Sumeetha Venkatesan, Ashwini Ramesh and Mahalakshmi Ramachandran.

I would like to mention that my achievement would not have been possible without the unconditional love of my family and for their constant faith and tremendous support, financially and mentally, including: my parents, C.R Sekhar and Geetha Sekhar, my brother Prakash Sekhar and my sister-in-law, Aarthi Venkataraman. A special mention to my niece Tanvi Prakash, who provided laughter, innocence and a well-needed distraction. I also appreciate the support of my extended family, near and far.

This research was supported by the NASA Mars Data Analysis Program grant NNX08AD07G.

TABLE OF CONTENTS

LIST OF FIGURES

Chapter 1

Chapter 2 (Manuscript)

Chapter 3

LIST OF TABLES

Chapter 2 (Manuscript)

Chapter 3

Chapter 4

Chapter 1

Introduction

The internal structure of a planetary body sheds light on the thermal history of the planet and reflects the composition and the conditions under which the planetary body formed. Geological features including topographic swells, wrinkle ridges fan faults and volcanic features on the surface are the result of heat transfer from the interior of the planet through the crust as the planet cools. In addition to surficial feature, the magnetic and gravity fields can be used to constrain the subdivision of the internal structure of a planetary body, for example, whether the interior differentiated of undifferentiated. The structure of the gravitational field provides information about the lateral density variation inside a planetary body.

Within planetary bodies, solid-state convection in the mantle is driven by internal heat sources including: accretional heat, radioactive decay, gravitational potential energy and tidal heating. Based on the material within the planetary body, the importance of a specific type of heat sources varies. For rocky terrestrial planets, radiogenic and accretional heat sources are usually the main heat sources. In cases where the planetary body is in resonance, tidal heat can be equally significant. On the other hand, icy bodies are driven by accretional and tidal heat. Radiogenic elements are generally found within silicate minerals; hence radiogenic heating is less prominent in icy bodies. Indicators of internal activity suggest a dynamic interior, which behaves like a viscous fluid. As a result of internal convection, there are signatures on the surface that relate to geological activity such as volcanoes.

Mars and Ceres are two interesting bodies in the solar system that display evidence of internal activity and will be the focus of this thesis. The largest volcano in the solar system, Olympus Mons is found on Mars. Mars has a rocky mantle with an iron core (*Solomon et al.,* 2005). Ceres interior is composed of a mixture of ice and silicate, much like the Jovian satellites Ganymede and Callisto (*McCord and Sotin*, 2005; *Thomas et al.,* 2005; *Li et al.,* 2006; *Castillo-Rogez and McCord,* 2010; *McCord et al.,* 2011).

Hydrothermally altered clays have been detected on the surface of Ceres, suggesting the presence of internal activity (*Milliken and Rivkin*, 2009). Seismic studies provide compositional information on the crust and upper mantle of Earth. On Mars, the InSight mission will deliver a single seismic station to Mars (*Panning et al.,* 2012). However, this is a future possibility on Mars and not yet a possibility on Ceres. Therefore, to understand the internal structure of planetary bodies, I proceed with numerical modeling of the interior coupled with gravity, topography, and geological surface features. To validate the modeling, results from the calculations must be compared with the geophysical observation of planetary bodies by the numerous space missions and probes.

1.1 Mars

Mars is the fourth planet is the solar system. It is a terrestrial planet that is half the diameter of Earth. The geological features on the surface of Mars include volcanoes, valleys, deserts and polar ice caps. The presence of recent volcanic activity (*Plescia*, 1990; *Hartmann et al.,* 1999; *Hartmann and Berman*, 2000; *Neukum et al*., 2004; *Wenzel et al.,* 2004; *Hartmann,* 2005; *Schumacher and Breuer,* 2007; *Hartmann et al.,* 2008; *Hauber et al.,* 2011) makes Mars a very interesting planet to study.

1.1.1 Martian Geological Features

The crustal dichotomy is one of the most prominent and the oldest geological feature on the surface of Mars (*McGill and Squyres*, 1991; *Nimmo and Tanaka*, 2005; *Carr*, 2006) (Figure 1.1). The crustal dichotomy divides the planet into the northern and southern hemisphere based on difference in elevation, crustal thickness and crater density (*Carr and Head*, 2010). The relative and absolute age of the highlands and lowlands have been determined by impact cratering studies (*Tanaka et al.,* 1992; *Lenardic et al.,* 2004; *Werner*, 2009) and the stratigraphic age of each stage has been analyzed (*Tanaka*, 1986; *Anderson et al.,* 2001) (Figure 1.2). The southern highlands are 5.5 km higher in elevation than the northern lowlands (*Zuber et al.,* 2000; *Aharonson et al.,* 2001; *Wenzel et al.,* 2004; *Carr and Head,* 2010) and the crust is 30 km thick in the northern hemisphere (*Zuber et al.,* 2000; *Wenzel et al.,* 2004) while it is 60 km thick in the

southern hemisphere (*Neumann et al.,* 2004; *Breuer and Spohn*, 2006). The visible crater density does not represent the difference in age between the two hemispheres (*Wilhelms and Squyres*, 1984; *Scott and Tanaka,* 1986; *Greeley and Guest*, 1987; *Tanaka and Scott,* 1987; *Smith et al.,* 1999b; *Frey et al.,* 2002; *Nimmo and Tanaka*, 2005; *Solomon et al.,* 2005; *Carr and Head*, 2010). Even though the northern hemisphere appears to be lightly cratered (*Mutch et al.,* 1976; *Carr,* 1981; *Smith et al.,* 1999b; *Wenzel et al.,* 2004), quasi-circular depressions reveal the presence of a very old basement beneath the cover of the northern lowlands (*Frey et al.,* 2002; *Frey,* 2006). Analysis of the quasi-circular depressions along with the observed craters in the northern lowlands shows that the lowlands are as old as the southern hemisphere.

The crustal dichotomy must have formed after the crust formation, which is dated at around 4.5 Gyr ago (*Werner*, 2009). It is also believed that the crustal dichotomy formed prior to the oldest impact crater, Utopia or Chryse, around 4.0 Gyr ago (*Frey*, 2003) which places the age of the dichotomy between 4.5 Ga and 4.0 Ga. However, the formation of the crustal dichotomy is still not clearly understood. There have been multiple hypotheses put forward to explain the formation of the crustal dichotomy. The age, size and shape of the dichotomy suggests that a large impact could have formed the dichotomy (*Wilhelms and Squyres,* 1984; *Andrews-Hanna et al.,* 2008; *Jaumann et al.,* 2008; *Marinova et al.,* 2008; *Nimmo et al.,* 2008) however the absence of rim around the basin and the absence of crustal thinning lead to the hypothesis that it was formed by internal mantle convection (*Wise et al.,* 1979; *Zhong and Zuber,* 2001; *Neumann et al.,* 2004). Mars Global Surveyor (MGS) gravity and topographic data is consistent with the hypothesis that the crustal dichotomy formed by large-scale convection (*Zuber et al.,* 2000). Gravity investigations of the basin beneath Tharsis are consistent with an oblique impact forming the dichotomy (*Andrews-Hanna et al.,* 2008; *Marinova et al.,* 2008).

There are other large-scale features on Mars that provide information that can constrain the thermal evolution of Mars. Tharsis and Elysium rises are two morphologically distinct volcanic provinces that sit 120 degrees apart near the crustal dichotomy boundary (*Werner*, 2009). Tharsis rise is one of the most prominent features of Mars, covering almost one quarter of the surface area of the planet. The largest known

shield volcano of the solar system, Olympus Mons, is found on Tharsis, along with other shield volcanoes like Alba Patera, Arsia Mons, Pavonis Mons and Ascraeus Mons (Figure 1.1). The Tharsis region comprises of two rises: the northern rise which consists of Alba Patera and the southern rise from 40^{o}S to 20^{o}N is the Tharsis Montes which consists of Arsia Mons, Pavonis Mons and Ascraeus Mons. Olympus Mons is located off the western edge of the Tharsis rise (*Smith et al.,* 1999b) and has a relief of 22 km with a complex caldera structure. Elysium, the second largest volcanic province is located on the northern lowlands and consists of three volcanoes: Elysium Mons, Hecates Tholus and Albor Tholus.

High-resolution images from the ESA Mars express mission along with images from Viking and Mars Orbiting Laser Altimeter (MOLA) provided insight into the morphology, topography and evolution of the shield volcanoes on Mars (*Werner,* 2009). In the northern rise, Alba Patera is larger than Olympus Mons in width but lower in height. In the southern rise, the Tharsis Montes is comprised of three volcanoes from northernmost to southernmost: Ascraeus Mons, Pavonis Mons and Arsia Mons. The surface age increases towards the southernmost volcano making Arsia Mons the oldest (*Plescia and Saunders*, 1979; *Neukum and Hiller*, 1981). The morphology, caldera complexity and slope steepness shows that Arsia Mons has shallow slopes and a simple large caldera compared to the younger, more complex caldera and steeper slopes of the others. Arsia Mons is the second largest volcano, in size, next to Olympus Mons. The middle volcano, Pavonis Mons was formed early in Martian history but also shows recent volcanic activity (*Werner*, 2009). Ascraeus Mons has a much more complex caldera structure making estimates of the surface age more difficult (*Werner,* 2009). Crater counting can only provide the surface ages of the youngest volcanic activity and shows that Ascraeus Mons was active until the recent past. In the Elysium province, Elysium Mons is the largest volcano. The northernmost volcano is Hecates Tholus while the southernmost volcano is Albor Tholus, which has a much younger caldera (*Werner*, 2009) (Figure 1.2).

1.1.2 Volcanic Activity and Thermal History

The surface features of Mars are divided into Noachian, Hesperian and Amazonian based on impact craters and intersection relations (*Scott and Carr*, 1978; *Tanaka,* 1986). Noachian era begins from the heavy bombardment era till 3.7 Gyr ago. Hellas basin is believed to have formed around 4.1 Gyr to 3.8 Gyr ago, which sets the timing for the Noachian period. This period is followed by the Hesperian period between 3.7 Gyr and 3.0 Gyr (*Hartmann and Neukum,* 2001; *Ivanov,* 2001). Finally, there is the Amazonian period, which starts at 3.0 Ga to present day.

For the pre-Noachian period, there is no record of the geological surface features as they have been completely erased. Volcanic activity has been extensive on the planet from the Noachian through the Hesperian period, causing resurfacing and volcanism reduced by a factor of ten during the Amazonian period. During the Noachian period, most of the volcanic activity was localized to Tharsis (*Hiller et al.,* 1982) giving rise to 9 km high structure approximately 5000 km wide by the end of the Noachian period (*Phillips et al.,* 2001). The rate of resurfacing during this period was dominated by impact cratering, however the primary volcanic deposits were preserved (*Squyres et al.,* 2007). There was widespread volcanism continuing in the Hesperian period (*Neukum et al.,* 2004; *Werner et al.,* 2004; 2005) and some lava plains that surrounds the central Tharsis and Elysium volcanoes is almost certainly Hesperian in age but is overlain by Amazonian plains (*Tanaka et al.,* 1988). Some of the smaller shield volcanoes in the Tharsis region are probably Hesperian or even older in age that have been buried underneath younger flow as Tharsis was formed, including Olympus Mons (*Carr and Head,* 2010). Volcanism during the Amazonian period was mostly focused on Tharsis and Elysium but it was in moderation and episodic in nature (*Neukem et al.,* 2004, 2007; *Schumacher and Breuer,* 2007; *Werner,* 2009) (Figure 1.3).

The slope of Tharsis rise determines the direction of the valley outflow channels (*Phillips et al.,* 2001), suggesting that Tharsis was in place after the formation of crustal dichotomy (*Werner,* 2009; *Carr and Head,* 2010). The Noachian age suggests that the lithospheric structure underneath the Tharsis region has remained pretty stable through Mars's evolution (*Anderson et al.,* 2001). The most recent loading is observed under the

Tharsis province due to its thick lithosphere and this suggests recent volcanic activity (*Tanaka et al.,* 1992; *Zuber et al.,* 2000). Therefore, while most of Tharsis rise was in place by end of the Noachian period, studies have indicated recent volcanic activity (*Plescia,* 1990; *Hartmann et al.,* 1999; *Hartmann and Berman*, 2000; *Neukum et al.,* 2004; *Hartmann,* 2005; *Hartmann et al.,* 2008; *Hauber et al.,* 2011). Atleast one volcano on Tharsis swell, Arsia Mons (*Hartmann et al.,* 1999; *Wenzel et al.,* 2004; *Schumacher and Breuer,* 2007), has been active within the last 10-30 Myr. The existence of young volcanism implies that adiabatic decompression melting and hence, upwelling convective flow in the mantle still plays an active role on Mars.

Heat transfer through the planet is controlled by mantle convection and I focus on plumes as the main mode of convection on Mars. Plume theory suggests that the location of Tharsis rise and the crustal dichotomy is coincidental. A number of researchers have suggested that one or more plumes upwellings are responsible for the volcanoes on Tharsis rise (*Harder and Christensen*, 1996; *Kiefer,* 2003; *Roberts and Zhong,* 2004; *Li and Kiefer,* 2007; *Grott and Breuer,* 2010). In addition to analyzing the plume structure, I will calculate the amount of melt produced in these calculations and compare this with the volcanic material on the surface. Melting on Mars can be constrained by a number of factors through time, including: past melt generated, the amount of melt required to make Tharsis and also sufficient melt to explain the present day volcanism.

Another factor that plays an important role in the melting history of a planet is radioactive decay. Partitioning of radioactive elements between crust and mantle must have happened early in Mars history. If the heat producing elements are uniformly distributed throughout the mantle, it would lead to a very high temperature in the lower mantle early in Martian history, which would cause widespread melting of the lower mantle and result in a molten mantle (*Kiefer,* 2003). This provides one constraint on the melt production during the early stages of Mars' formation. The formation of Tharsis rise places another constraint on the timing of melt production and thus, the thermal history of Mars. There must be sufficient melt to create Tharsis rise by the end of the Noachian era but then melt production should taper off rapidly. This will be examined in Chapter 2.

1.1.3 Areoid and Surface Topography

A number of studies have used gravity and topography to understand the Martian lithosphere (c.f., *Turcotte et al.,* 1981; *Sleep and Phillips*, 1985; *Anderson and Grimm,* 1998) and determine crustal thickness (*Neumann et al.,* 2004). Mars Orbiter Laser Altimeter (MOLA) (*Smith et al.,* 2001) and Mars Global Surveyor (MGS) provide global topographic and gravity data (*Smith et al.,* 1999a) which can be used to study the interior and thermal evolution of Mars. The gravity and topographic data from Mars Global Surveyor showed that the present day crustal thickness is approximately 50-120 km (*Neumann et al.,* 2004). The Martian areoid (geoid) is dominated by two large highs, one over Tharsis and the other approximately 180 degrees away (*Smith et al.,* 1999a) (Figure 1.4). The prominent long-wavelength topographic structures are related to the Tharsis Rise and the crustal dichotomy (*Zhong and Roberts,* 2003), where the Tharsis rise may be associated with a deeper mantle component (*Redmond and King,* 2004). According to *Kiefer et al.* (1996), a significant fraction of the topography and geoid, up to spherical harmonic degree 10, is supported by mantle convection. *Kiefer et al.* (1996) specifically note that degrees 2 through 4 of the geoid and topography are inconsistent with an isostatic model and require deep mantle structure. The anti-Tharsis geoid high may be due to elastic deformation of the crust, which in turn may be due to the load created by Tharsis (*Hauck and Phillips,* 2002) as expected by the topographic loading on a spherical elastic shell (*Phillips et al.,* 2001). While Martian surface topography is dominated by the hemispherical dichotomy and Tharsis rise (*Zuber et al.,* 2000) by construction, gravity models have no degree-1 component. However, due to the non-uniqueness of gravity, there is a tradeoff between Moho topography and internal structure of the mantle. This will be examined in Chapter 3.

1.2 Ceres

Ceres was discovered by Giuseppe Piazzi in Italy on January/February 1801 while he was searching for a planet located at 2.8 AU from the Sun predicted by Titus-Bode law (*Piazzi*, 1802; *Encyclopedia Britannica*, 2004). Meanwhile, a German team who was

also searching for a planet found the asteroid Vesta. The large mass of Jupiter may have disrupted the formation of a planet in the region of the asteroid belt.

1.2.1 Geological Features and Volcanic Activity

Ceres is the largest object, and the only dwarf planet, in the asteroid belt and it contains majority of the mass in the asteroid belt (*McCord et al.,* 2011). It is spherical in shape and is believed to have a differentiated structure of core and mantle composed of a rock-ice mixture (*Castillo-Rogez and McCord,* 2010; *McCord et al.,* 2011). Ceres is similar to the icy moons of the Jovian and Saturnian systems because of the presence of water alteration on the surface and differs from rocky asteroids due to a higher percent of water in the mantle (*Li et al.,* 2006; *Carry et al.,* 2008; *Castillo-Rogez and McCord,* 2010; *McCord et al.,* 2011). Ceres is also believed to have undergone an evolution process similar to planets. Studying Ceres is important for the understanding of planetary evolution, because it is considered to be a protoplanet that existed since the formation of the solar system (*Carry et al.,* 2008). Ceres may also hold the key to understanding the importance of volatiles, early on in the solar system (*Carry et al.,* 2008). Hence, understanding the internal process within Ceres would shed light on the convection process on Ceres.

The comparatively small size of Ceres suggests that it should have cooled early in its formation and should be geologically inactive. However, the surface shows the presence of brucite and serpentine, which suggests cryovolcanic activity occurred on the surface at some time in the recent past (*Rivkin et al.,* 2006; *Carry et al.,* 2008; *Milliken and Rivkin*, 2009). When warm water interacts with olivine rich elements, it undergoes serpentinization. The presence of brucite suggests that Ceres has been hydrothermally active (e.g., *Wilson et al.,* 1999; *Young,* 2001; *Milliken and Rivkin,* 2009). Material from the mantle can be propagated to the surface through plumes and mantle convection. This, along with the geoid and topography, will be examined in the Chapter 4.

1.2.2 Geoid and Topography

The surface of Ceres lacks large-scale topographic features (*Carry et al.,* 2008; *Castillo-Rogez and McCord,* 2010) but based on Hubble Space Telescope images, a number of craters have been observed. The surface is expected to have fewer craters with majority of the craters being erased by dynamic processes (*Castillo-Rogez and McCord,* 2010). The origin and nature of many of the surface features have yet to be explained.

NASA launched the Dawn space probe to study the asteroid Vesta and the dwarf planet Ceres. The discovery of Vesta and Ceres by the German and Italian teams makes them important contributors to the Dawn mission (*McCord and Sotin,* 2005). Dawn was launched in 2007 and first approached and orbited Vesta in 2011. Dawn will arrive at Ceres in 2015. The Dawn spacecraft instrumentation includes a framing camera, a visual and infrared spectrometer, and a gamma ray and neutron detector. Dawn is designed to provide insight into the bulk density (< 1%), surface images, abundance of rock-forming elements, gravity field with a half wavelength resolution ≤ 90 km (for Vesta) and ≤ 300 km (for Ceres) and topographic maps covering ≥ 80% of the surface (*Rayman et al.,* 2006). Upon Dawn's arrival at Vesta, studies have shown the global crater distribution (*Marchi et al.,* 2012), the presence of large impact basin (*Jaumann et al.,* 2012; *Schenk et al.,* 2012), many eroded gullies on the surface suggesting the possibility of flowing water. The size of Vesta's core was estimated to be around 220 km consisting of metal iron. After collecting data on Vesta, Dawn set out to explore Ceres in 2012.

Once Dawn arrives at Ceres, it will examine Ceres's shape, mineralogy and elemental composition. In addition, studies on the shape and surface features such as topography will shed more light into the internal structure and evolution of the dwarf planet. My modeling studies on the mantle structure and geoid and topography can help correlate with the data collected by Dawn and suggest the various probabilities and possibilities about its evolution.

1.3 Modeling

In this work, mantle convection simulations are performed using finite element program CitcomS (*Zhong et al.,* 2000, 2008; *Tan et al.,* 2006), which stands for California Institute of Technology Convection in the Mantle, from the Computational Infrastructure for Geodynamics initiative (CIG). It is available at http://www.geodynamics.org/cig/software/citcoms. CitcomS is used to model thermal convection calculations in a 3D spherical shell (Figure 1.5). It consists of a global mesh with 12 caps and uses 216 cores on a cluster (Figure 1.6). Thermal convection calculations are governed by equation of conservation of mass, energy and momentum. These models depend on the initial condition, boundary conditions and many other parameters, some of which are not well defined. The computation work was carried out on HESS (for High – performance Earth System Simulator), a powerful supercomputers at Virginia Tech. HESS is a 96-node dual quad-core system using the Intel clovertown processor. Each node has 8 cores, 12 GB of memory and is connected via DDR infiniband.

I generate an areoid map of Mars using the geoid data file jgm95j01.sha obtained from the Mars Global Surveyor (MGS) spacecraft (Figure 1.4), which was accessed from the website: http://ppi.pds.nasa.gov/data/MGS-M-RSS-5-SDP-V1.0/DATA/RS_SHA/ on January 21, 2014. JGM95 is a gravity model with a maximum spherical harmonic degree of 95 (*Neumann et al.,* 2004; *Konopliv et al.,* 2006; *Wieczorek,* 2007). The geoid and topography maps in this thesis are generated using GMT, for Generic Mapping Tools, a software created by *Wessel and Smith* (2001). It is a free software used for mapping studies and data processing on a global scale. It can be customized to the user's needs and represents 3-dimensional data in 2-dimensions. GMT is also freely available software for download at this website: http://gmt.soest.hawaii.edu/.

1.3.1 Martian Rheology

Mantle convection models can be used to study the generation of melt on Mars through time. The main mode of heat transfer at present day in the Martian mantle is the stagnant lid convection (*Grasset and Parmentier*, 1998; *Spohn et al.,* 2001). The

computational grid used for previous Mars melting studies (*Kiefer,* 2003) was an axisymmetric, hemispherical shell rather than a full, 3D spherical shell. Kiefer's work showed that present day melting would be restricted to the heads of hot mantle plumes that rise from core-mantle boundary, consistent with the spatially localized distribution of recent volcanism on Mars (Figure 1.7).

The calculations in this thesis are performed in a 3D spherical shell with a cold free-slip upper boundary and a free-slip core mantle boundary. I use time-dependent, rather than steady state, stagnant lid, incompressible convection calculations. I implement a temperature-dependent Newtonian rheology based on the creep properties of olivine (e.g., *Karato and Wu,* 1993) and a layered viscosity structure that includes a viscosity increase by a factor of 8 and 25 at a depth of 996 km (*Roberts and Zhong,* 2006). This depth corresponds to the pressure of the phase transition between olivine and spinel and the pressure at which a viscosity increase on Earth is needed to explain the long wavelength geoid (*Hager and Richards,* 1989). Due to Mars' lower gravity, this phase transition occurs in the mid-mantle in comparison to the upper mantle on Earth. Hence a viscosity jump might be expected at this depth (*Roberts and Zhong*, 2006). I consider both a constant heating rate and heating rate that decreases with time due to the decay of long-lived radioactive isotopes. I implement latent heat of melting and also a decreasing core mantle boundary temperature following *Hauck and Phillips* (2002) for decaying heat source models. Inclusion of latent heat of melting and core cooling affects the production of melt and the thickness of the boundary layer at the core-mantle boundary.

I altered the finite element code to implement radiogenic elements that decay with time, latent heat of melting and core cooling. I also included a section in the code to analyze the melt production on a global scale and how I calculate it is given in the next section.

1.3.2 Melt Calculation

I follow *Kiefer's* (2003) method to calculate the melt from the resulting pressure and temperature fields of my calculations. Figure 1.8 depicts the solidus temperature as a function of pressure, and the best-fit line was a third-order polynomial using the values of

the high-pressure solidus of the Martian mantle from *Bertka and Holloway* (1994). *Bertka and Holloway* (1994) calculated the partial melting using the mantle composition of *Wanke and Dreibus* (1994). *Bertka and Holloway* (1994) had the lowest dry melting solidus for a Mars-analogue composition.

Because there are few constraints on the production of melt above the solidus at high pressure, I assume that melt productivity varies linearly with temperature above the solidus. Based on terrestrial peridotite studies by *Takahashi et al* (1993) and Martian meteorite studies at high pressures by *Agee and Draper* (2004), I assume the average melt productivity to be about 0.5% per degree ($0.005K^{-1}$) above the solidus (*Kiefer,* 2003).

I begin the calculations at 4.3 Ga to focus on the melt production required for volcanism alone not on the melt required to create the crust. Based on data, I calculate the melt required to create Tharsis on the surface. I also assume that approximately 10% of the melt created in the mantle reaches the surface, based on mid-ocean ridge calculations (*Klein and Langmuir,* 1987). Using this assumption, I re-calculate how much melt is required in the mantle to create Tharsis. In my modeling, I remove the melt produced at every step instantaneously and consider the melt productivity at each individual time step. A more complete melting model would track the parcel of mantle that had been melted and consider the impact of re-melting this material.

1.3.3 Ceres Rheology

Mantle convection models can also be used to study the evolution of Ceres through time. Ceres is still comparatively new and unexplored and has not been extensively modeled in 3D. Previous work involved a 1D finite difference code (*McCord and Sotin*, 2005). *McCord and Sotin* (2005) consider different internal structures depending on the timing of the formation of Ceres.

Compared to 1D modeling, I proceed with 3D mantle convection modeling. I consider a non-Newtonian viscous rheology for a creeping incompressible fluid consistent with water ice rheology. Based on the grain-boundary sliding deformation

mechanism for Ice-1, water ice rheology is strongly dependent on temperature and stress (Figure 1.9). I consider a stagnant lid convection model with a cold upper boundary and a free slip core mantle boundary. I vary ratios of ice and silicate in the mantle with no core cooling. In my work, this ratio constraints the critical mantle shell thickness and the state of the differentiated structure of the mantle. The constraint on the fraction of silicate is 74% by mass and water fraction is 26% mass (*Castillo-Rogez and McCord,* 2010). I analyze the critical grain size of ice particles and the viscosity of the mantle is always dominated by ice (strain-rate dependent).

1.4 Conclusion

The difference between volcanoes on Earth and Mars is the low gravity of the planet and the absence of present day tectonic plates on Mars (*Sleep*, 1994; *Spohn et al.,* 2001) that lead to larger volcanoes with higher eruption rates (*Basaltic Volcanism Study Project (BSVP),* 1981). But why is volcanism so prevalent in two specific regions of Mars? And is it correct for us to assume degree-1 structure for the Martian mantle (*Roberts and Zhong*, 2006) when we have recent volcanism on both Tharsis and Elysium? In Chapter 2, I analyze the melt production from 3D spherical mantle convection calculations in order to explain volcanism on Mars and the probability of a low-degree structure to explain the isolated volcanic activity on the surface. Core cooling and latent heat of melting are important in the evolution of a planet and CitcomS has been altered to implement these changes in the code. Latent heat of melting removes the excessive temperatures produced in the mantle and in turn reduces the melt production. The decrease in core mantle heat flow with time strongly influences the formation of mantle plumes. Mantle upwelling could provide a correlation with the Martian geoid and the recent volcanism (*Steinberger et al.,* 2009).

In Chapter 3, I will analyze the geoid and topography of Mars comparing many of the models from Chapter 2 with the observed geoid and topographic models from the Mars Global Surveyor mission. Along with dynamic topography, I use gravitational potential or geoid, rather than free-air gravity following *Hager* (1984) and *Richards and Hager* (1984) to study the distribution of internal density within the Martian mantle. The gravitational potential falls off as $1/r$ rather than $1/r^2$, thus is more sensitive to deeper

denser structures than gravity (c.f., *Hager and Clayton*, 1989). Identifying the mantle contribution to gravity and topographic will indicate how much mantle density anomalies impact the crustal structure. Comparing the gravity and topography from convection calculations to the observed gravity and topography fields from the MGS and Mars Odyssey missions provides us the opportunity to test Martian mantle models such as the degree-1 mantle structure and viscosity layering in the mantle.

The final chapter is the study of Ceres. In the case of an icy body like Ceres, I analyze the effect that grain size has on the convective solution for varying mantle shell thickness. My results indicate a wide-range of parameters where convection within Ceres persists to present day. I estimate surface deformation, topography, geoid, and heat flow from these calculations, which can be compared with observational data when Dawn arrives at Ceres in 2015.

References

Agee, C.A. and D.S. Draper (2004). Experimental constraints on the origin of Martian meteorites and the composition of the Martian mantle, *Earth and Planetary Science Letters*, 224, 415-429.

Aharonson, O., Zuber, M.T. and D.H. Rothman (2001). Statistics of Mars' topography from the Mars orbiter laser altimeter: slopes, correlations, and physical models. *Journal of Geophysical Research*. Vol 109, 723-723 23, 735.

Anderson, S., and R. E. Grimm (1998). Rift processes at the Valles Marineris, Mars: Constraints from gravity on necking and rate-dependent strength evolution, *Journal of Geophysical Research*. Vol 103, 11,113 11,124.

Anderson, R.C. et al (2001). Primary centers and secondary concentrations of tectonic activity through time in the western hemisphere of Mars, *Journal of Geophysical Research*. Vol 106, 20563 -20585.

Andrews-Hanna, J.C., Zuber, M.T. mad W.B. Banerdt (2008). The Borealis basin and the origin of the Martian crustal dichotomy. *Nature* Vol 453, 1212–1215.

Basaltic Volcanism Study Project (1981). Basaltic Volcanism on the Terrestrial Planets. *Pergamon Press, Inc., New York*. 1286 pp.

Bertka, C.M. and J.R. Holloway (1994). Anhydrous partial melting of an iron-rich mantle I: Sub solidus phase assemblages and partial melting phase relationships at 10 to 30 kbar, *Contributions to Mineralogy and Petrology* Vol 115, 313-322.

Breuer, D. and T Spohn (2006). Viscosity of the Martian mantle and its initial temperature: Constraints from crust formation history and the evolution of the magnetic field, *Planetary and Space Science* Vol 54, 153-169.

Carr, M.H. (1981). The Surface of Mars, *Yale Univ. Press*, New Haven, CT.

Carr, M.H. (2006). The Surface of Mars. *Cambridge University Press*. 307 pp.

Carr, M.H. and J.W. Head III (2010). Geologic history of Mars, *Earth and Planetary Science Letters* Vol 294, 185-203.

Carry, B., et al (2008). Near-infrared mapping and physical properties of the dwarf-planet Ceres. *Astronomy and Astrophysics* Vol 478, 235–244.

Castillo-Rogez, J and T.B. McCord (2010). Ceres' evolution and present state constrained by shape data. *Icarus* Vol 205, 443-459.

Draper D. S., Xirouchakis D., and C. B Agee (2003). Trace element partitioning between garnet and chondritic melt from 5 to 9 GPa: Implications for the onset of the majorite transition in the Martian mantle. *Physics of the Earth and Planetary Interiors* 139:149– 169.

Encyclopedia Britannica (2004). Giuseppe Piazzi, Chicago, Ill. (Available at http://www.britannica.com/search?query=Giuseppe+Piazzi&ct=)

Frey, H.V. et al (2002). Ancient lowlands on Mars, *Geophysical Research Letters* Vol 29, 10, 1384.

Frey, H.V. (2003). Buried impact basins and the earliest history of Mars. *Lunar Planet. Sci*. Vol 35, 3104 abstract.

Frey, H. V. (2006). Impact constraints on, and a chronology for, major events in early Mars history, *Journal of Geophysical Research*. Vol 111, E08S91.

Grasset, O. and E.M., Paramentier (1998). Thermal convection in a volumetrically heated, infinite Prandtl number fluid with strongly temperature-dependent viscosity: Implications for planetary thermal evolution, *Journal of Geophysical Research*. Vol 103, B8, 18,171-18,181.

Greeley, R. and J. E. Guest (1987). Geological map of the eastern equatorial region of Mars, *U.S. Geol. Surv., Misc. Invest. Series, Map 1-1802-B*.

Grott, M. and D. Breuer (2010). On the spatial variability of the Martian elastic lithosphere thickness: Evidence for mantle plumes? *Journal of Geophysical Research*. Vol 115.

Hager, B. H (1984). Subducted slabs and the geoid; constraints on mantle rheology and flow. *Journal of Geophysical Research*. Vol 89, 6003-60015.

Hager, B. H., and R. W, Clayton (1989). Constraints on the structure of mantle convection using seismic observations, flow models, and the geoid. In: Peltier, W R (ed.) *Mantle Convection*. 658-753.

Hager, B. H. and M.A Richards (1989). Long-wavelength variations in Earth's geoid: Physical models and dynamical implications, *Phil. Trans. R. Soc. Lond. A* Vol 328, 309– 327.

Harder, H. and U. Christensen (1996). A one-plume model of Martian mantle convection, *Nature*, Vol. 380, 507-509.

Hartmann, W. K. (2005). Martian cratering 8: Isochron refinement and the chronology of Mars, *Icarus* Vol. 174, 294–320.

Hartmann, W.K. et al (1999). Evidence for recent volcanism on Mars from crater counts, *Nature* Vol 397, 586–589.

Hartmann, W.K. and D.C. Berman (2000). Elysium Planitia lava flows: crater count chronology and geological implications. *Journal of Geophysical Research*. Vol 105, 15011–15026.

Hartmann, W. K., Neukum, G. and S. Werner (2008). Confirmation and utilization of the "production function" size frequency distributions of Martian impact craters, *Geophys. Res. Lett.* Vol. 35.

Hartmann, W.K. and G. Neukum (2001). Cratering chronology and the evolution of *Mars. Space Sci. Rev.* Vol 96, 165–194.

Hauber, E., et al (2011). Very recent and wide-spread basaltic volcanism on Mars. *Geophysical Research Letters* Vol 38.

Hauck, S. A. II, and R. J. Phillips (2002). Thermal and crustal evolution of Mars, *Journal of Geophysical Research*. Vol 107, E5052.

Hiller, K.H. et al (1982). Mars—Stratigraphy and gravimetry of Olympus Mons and its aureole. *Journal of Geophysical Research*. Vol. 87, 9905–9915.

Ivanov, B.A. (2001). Mars/Moon cratering rate ratio estimates. *Space Sci. Rev.* Vol 96, 87–104.

Jaumann, R. et al (2008). Mega-impact formation of the Mars hemispheric dichotomy. *Nature* Vol 453, 1216–1219.

Jaumann, R. et al (2012). Vesta's Shape and Morphology. *Science* 336, 687.

Karato, S., and P. Wu (1993). Rheology of the upper mantle: A synthesis, *Science*, Vol. 260, 771-778.

Kiefer, W.S., B.G. Bills and R.S. Nerem (1996). An inversion of gravity and topography for mantle and crustal structure on Mars, *Journal of Geophysical Research*. Vol 101, 9239-9252.

Kiefer, W. S. (2003). Melting in the Martian mantle: Shergottite formation and implications for present-day mantle convection on Mars, *Meteoritics*, Vol 38, 1815 1832.

Klein, E.M. and C.H Langmuir (1987). Global Correlations of Ocean Ridge Basalt Chemistry with Axial Depth and Crustal Thickness, *Journal of Geophysical Research*. Vol 92, 8089–8115.

Konopliv, A. S. et al (2006). A global solution for the Mars static and seasonal gravity, Mars orientation, Phobos and Deimos masses, and Mars ephemeris, *Icarus*, Vol. 182, 23–50.

Lenardic, A., Nimmo, F. and L. Moresi (2004). Growth of the hemispheric dichotomy and the cessation of plate tectonics on Mars, *Journal of Geophysical Research*. Vol 109.

Li, J.Y., et al (2006). Photometric analysis of 1 Ceres and surface mapping from HST observations. *Icarus* Vol. 182, 143–160.

Li, Q., and W.S. Kiefer (2007). Mantle convection and magma production on present-day

Mars: Effects of temperature-dependent rheology, *Geophys. Res. Lett.* Vol 34.

Marchi S et al (2012). The Violent Collisional History of Asteroid 4 Vesta. *Science* Vol 336, 690.

Marinova, M. M., O. Aharonson, and E. Asphaug (2008). Mega-impact formation of the Mars hemispheric dichotomy. *Nature*, Vol. 453, doi:10:1038/nature07070, 1216-1219.

McCord, T.B. and C. Sotin (2005). Ceres: Evolution and current state. *Journal of Geophysical Research*. Vol 110. E05009.

McCord, T.B., Castillo-Rogez, J. and A. Rivkin. (2011). Ceres: Its Origin, Evolution and Structure and Dawn's Potential Contribution, *Space Sci Rev*, DOI 10.1007/s11214-010-9729-9.

McGill, G.E. and S.W., Squyres (1991). Origin of the Martian crustal dichotomy: evaluating hypotheses. *Icarus* Vol 93, 386–393.

Milliken, R.E. and A.S. Rivkin (2009). Brucite and carbonate assemblages from alteration of olivine-rich materials on Ceres. *Nat. Geosci*. Vol 2, 258–261.

Mutch, T.A. et al (1976). The Geology of Mars, *Princeton Univ. Press, Princeton, NJ*.

Neukum, G. and K, Hiller (1981). Martian ages. *Journal of Geophysical Research*. Vol 86, 3097–3121.

Neukum, G., et al. HRSC Co-Investigator. (2004). Recent and episodic volcanic and glacial activity on Mars revealed by the High Resolution Stereo Camera. *Nature* Vol 432, 346–351.

Neukum, G., et al. the HRSC Co-Investigator Team. (2007). The geologic evolution of Mars: episodicity of resurfacing events and ages from cratering analysis of image data and correlation with radiometric ages of Martian meteorites. *Lunar and Planetary Science Conference XXXVIII*, p. 2271. Abstract.

Neumann, G.A. et al (2004). Crustal structure of Mars from gravity and topography. *Journal of Geophysical Research*. Vol. 109. doi:10.1029/2004JE002262.

Nimmo, F. and K. Tanaka (2005). Early crustal evolution of Mars. *Ann. Rev. Earth Planet. Sci*. Vol 33, 133–161.

Nimmo, F. et al (2008). Implications of an impact origin for the Martian hemispheric dichotomy. *Nature* Vol 453, 1220–1223.

Panning, P. et al (2012). InSight: Single station broadband seismology for probing Mars' interior. *Lunar and Planetary Science Conference (LPSC)*.

Phillips, R.J., et al (2001). Ancient geodynamics and global-scale hydrology on Mars. *Science* Vol 291, 2587–2591.

Piazzi, G., 1802. Della scoperta del nuovoplanetaCerereFerdinandea, Palermo Observ., Palermo, Italy.

Plescia, J.B., Saunders, R.S., 1979. The chronology of the Martian volcanoes. *Lunar Planet. Sci*., 2841–2859.

Plescia, J.B., 1990. Recent flood lavas in the Elysium region for Mars. *Icaru*s Vol 88, 465–490.

Rayman, M. D et al (2006). Dawn: A mission in development for exploration of main belt asteroids Vesta and Ceres. *Acta Astronautica* Vol 58, 605 – 616.

Redmond, H. L. and S.D. King (2004). A numerical study of a mantle plume beneath the Tharsis Rise: Reconciling dynamic uplift and lithospheric support models, J *Journal of Geophysical Research*. Vol, 109, E09008.

Richards, M. A., and B. H. Hager (1984). Geoid anomalies in a dynamic earth, *Journal of Geophysical Research*. Vol 89 5987-6002.

Rivkin, A.S., Volquardsen, E.L. and B.E. Clark (2006). The surface composition of Ceres: Discovery of carbonates and iron-rich clays. *Icarus* Vol 185 563–567.

Roberts, J.H. and S. Zhong (2004). Plume-induced topography and geoid anomalies and their implications for the Tharsis rise, *Journal of Geophysical Research*. Vol 109, E03009.

Roberts, J.H. and S. Zhong (2006). Degree-1 convection in the Martian mantle and the origin of the hemispheric dichotomy, *Journal of Geophysical Research*. Vol 111.

Schenk, P. et al. (2012). The geologically recent giant impact basins at Vesta's south pole. *Science* Vol 336, 694.

Schumacher, S. and D. Breuer, D. (2007). An alternative mechanism for recent volcanism on Mars. *Geophys. Res. Lett.* Vol 34, 14202–14206.

Scott, D.H., and M.H., Carr (1978). Geologic map of Mars. *U.S. Geological Survey Misc. Inv. Map I-1083.*

Scott, D. H. and K.L., Tanaka, (1986). Geologic map of the western equatorial region of Mars, *U. S. Geol. Surv. Misc. Invest. Series, Map I-1802-A*.

Sleep, N. H., and R. J. Phillips (1985). Gravity and lithospheric stress on the terrestrial planets with reference to the Tharsis region of Mars, *Journal of Geophysical Research*. Vol 90, 4469-4489.

Sleep, N.H. (1994). Martian plate tectonics. *Journal of Geophysical Research*. Vol 99, 5639–5655.

Smith, D.E., et al (1999a). The gravity field of Mars; results from Mars Global Surveyor, *Science*, Vol 286, 94- 97.

Smith, D.E. et al (1999b). The Global Topography of Mars and Implications for Surface Evolution, *Science* Vol. 284 (5419), 1495-1503.

Smith, D. E. et al (2001). Mars Orbiter Laser Altimeter: Experiment summary after the first year of global mapping of Mars, *Journal of Geophysical Research*. Vol 106, 23,689-23,722.

Solomon, S. C et al (2005). New perspectives on Ancient Mars, *Science* Vol 307 (5713), 1214–1220.

Sotin, C et al (2008). Convection in icy satellites: Models and constraints from laboratory experiments. *Science of Solar System Ices*

Spohn et al (2001). Geophysical constraints on the evolution of Mars. *Space Science Reviews* Vol 96, 231-262.

Steinberger, B., Werner, S.C. and T.H. Torsvik (2009). Deep versus shallow origin of gravity anomalies, topography and volcanism on Earth, Venus and Mars. *Icarus*, submitted for publication.

Squyres, S.W. et al (2007). Pyroclastic activity at home plate in Gusev Crater, Mars. *Science* Vol 316, 738–742.

Takahashi, E. et al (1993). Melting Study of a Peridotite KLB-1 to 6.5 GPa, and the Origin of Basaltic Magmas, *Philosophical Transactions of the Royal Society of London, A* Vol 342 (1663) 105-120.

Tan, E., Choi et al (2006) .Geo Framework: Coupling multiple models of mantle convection within a computational framework, *Geochemistry Geophysics Geosystems* 7 (6).

Tanaka, K.L. (1986). The stratigraphy of Mars. Proc. Lunar Planet. Sci. Conf. 17, *Journal of Geophysical Research*. Vol 91, E139–E158.

Tanaka, K. L. and D.H., Scott (1987). Geological map of the polar regions of Mars*, U. S. Geol. Sum., Misc. Invest. Series, Map 1-1802-C*.

Tanaka, K.L. et al (1988). The resurfacing history of Mars: a synthesis of digitized, Viking-based geology. *Proc. Lunar Planet. Sci. Conf.*18, 665–678.

Tanaka, K. L., Scott, D.H. and R. Greeley (1992). Global stratigraphy, in Mars, edited by H. H. Kieffer et al., chap. 11, 345–382, Univ. of Ariz. Press, Tucson.

Thomas, C., et al (2005). Differentiation of the asteroid Ceres as revealed by its shape. *Nature* Vol 437, 224–226.

Turcotte, D. L. et al (1981). Role of membrane stresses in support of planetary topography, *Journal of Geophysical Research*. Vol 86, 3951-3959.

Wanke, H. and G. Dreibus (1994). Chemistry and Accretion History of Mars, *Philosophical Transactions: Physical Sciences and Engineering* Vol 349 (1690) 285-293.

Wenzel, M. J., Manga, M. and A. M. Jellinek (2004). Tharsis as a consequence of Mars dichotomy and layered mantle. *Geophys. Res. Lett.,* Vol 31, L04702.

Werner, S.C., G. Neukum, The HRSC Co-Investigator Team (2004). New insights into the evolutionary history of the major volcanic constructs from Mars Express HRSC data. *Bull. Am. Astron. Soc. 36*.

Werner, S.C. and G. Neukum, The HRSC Co-Investigator Team (2005). Major volcanic constructs seen from Mars Express HRSC—New insights into their evolutionary history. *In: Proc. Lunar Sci. Conf*. 36. No. 1766.

Werner, S. C. (2009). The global Martian volcanic evolutionary history, *Icarus* Vol 201, 44-68.

Wieczorek, M. A. (2007). Gravity and Topography of the Terrestrial Planets, in *Treatise on Geophysics*, T. Spohn and G. Schubert (eds.), Vol. 10, 165-206, Elsevier.

Wilhelms, D.E. and S.W. Squyres, (1984). The Martian hemispheric dichotomy may be due to a giant impact. *Nature* Vol 309, 138–140.

Wilson, L. et al (1999). Early aqueous alteration, explosive disruption, and re-processing of asteroids. *Meteorit. Planet. Sci*. Vol 34, 541–557.

Wise, D.U., Golombek, M.P. and G.E. McGill (1979). Tectonic evolution of Mars. *Journal of Geophysical Research*. Vol 84, 7934–7939.

Young, E.D. (2001). The hydrology of carbonaceous chondrite parent bodies and the evolution of planet progenitors. *Phil. Trans. Roy. Soc. Lond. A* Vol. 359, 2095–2110.

Zhong, S. et al (2000). Role of temperature-dependent viscosity and surface plates in spherical shell models of mantle convection, *Journal of Geophysical Research*. Vol 105 (B5), 11063–11082.

Zhong, S., and M.T. Zuber (2001). Degree-1 mantle convection and the crustal dichotomy on Mars. *Earth Planet. Sci. Lett.* Vol 189, 75–84.

Zhong, S., and J. H. Roberts (2003). On the support of the Tharsis rise on Mars, *Earth Planet. Sci. Lett.,* Vol 214, 1–9.

Zhong, S. et al (2008). A benchmark study on mantle convection in a 3-D spherical shell using CitcomS, *Geochem. Geophys. Geosyst*., 9.

Zuber, M.T. et al (2000). Internal structure and early thermal evolution of Mars from Mars Global surveyor topography and gravity. *Science* Vol 287, 1788–1793.

Figures

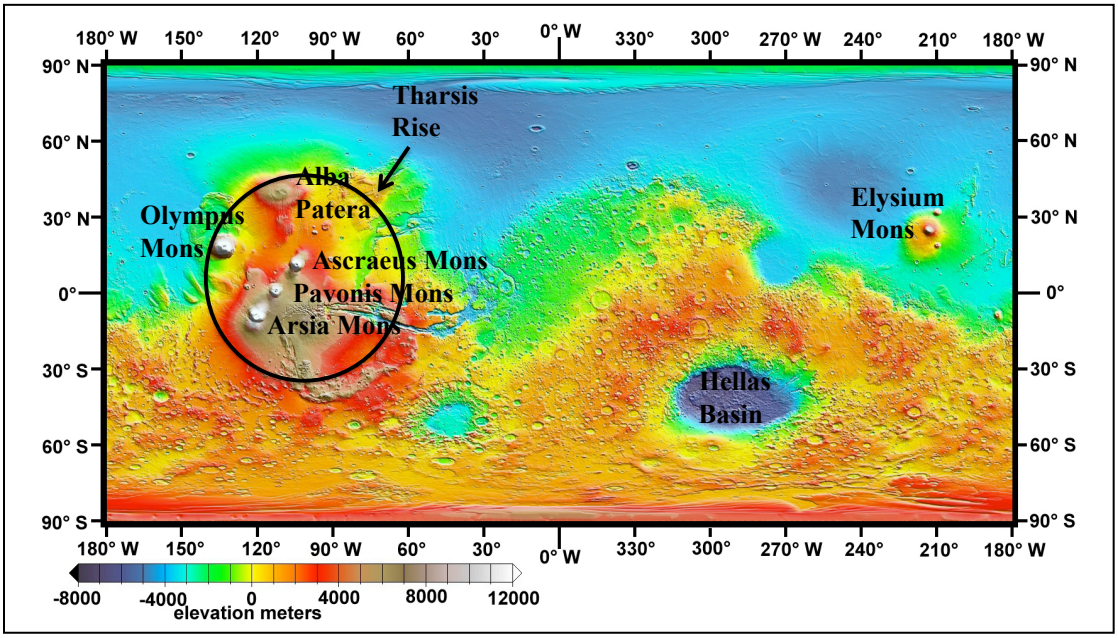

Figure 1.1 Crustal Dichotomy of Mars (after *Smith et al.,* 1999b) based on the MOLA data.

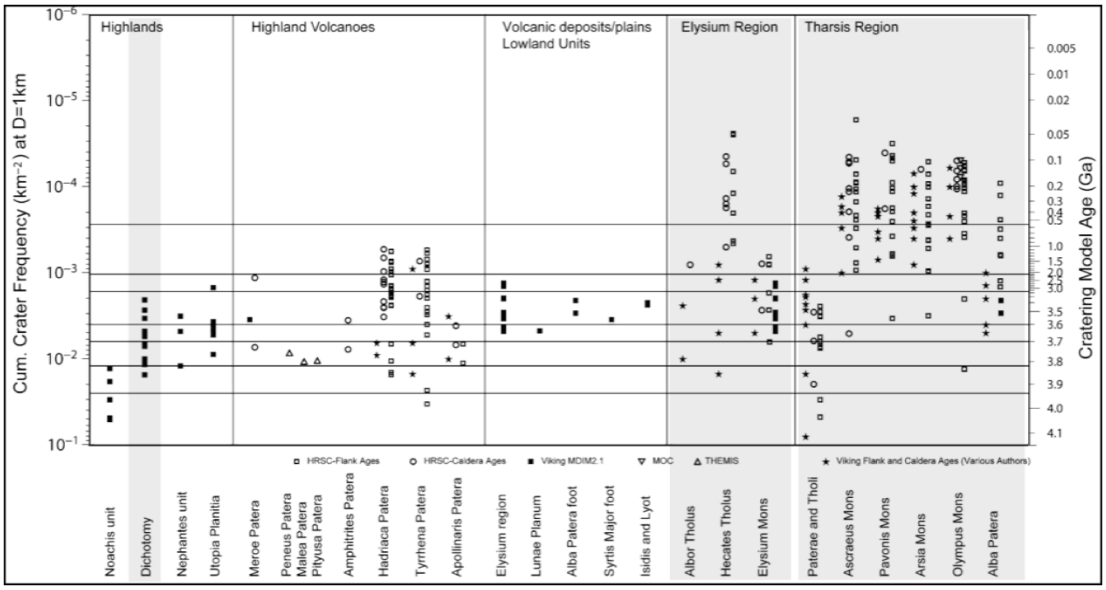

Figure 1.2 Cratering age of the individual volcanoes of the Tharsis and Elysium province, including the global dichotomy (after *Werner*, 2009).

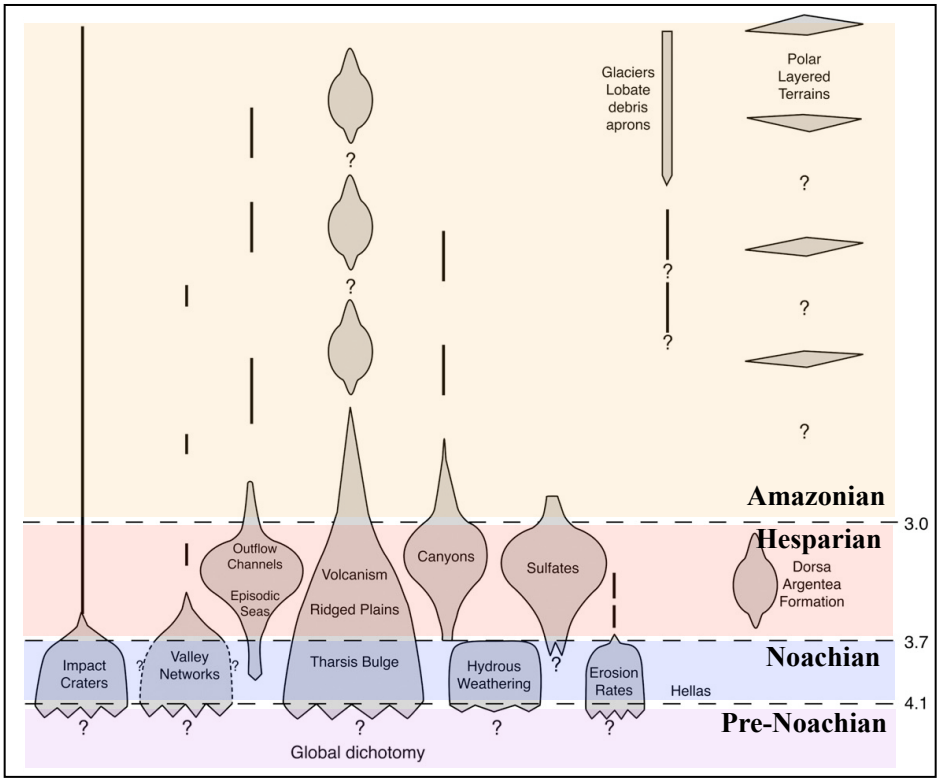

Figure 1.3 Volcanism during the three main time periods: Noachian, Hesparian and Amazonian periods (after *Carr and Head*, 2010).

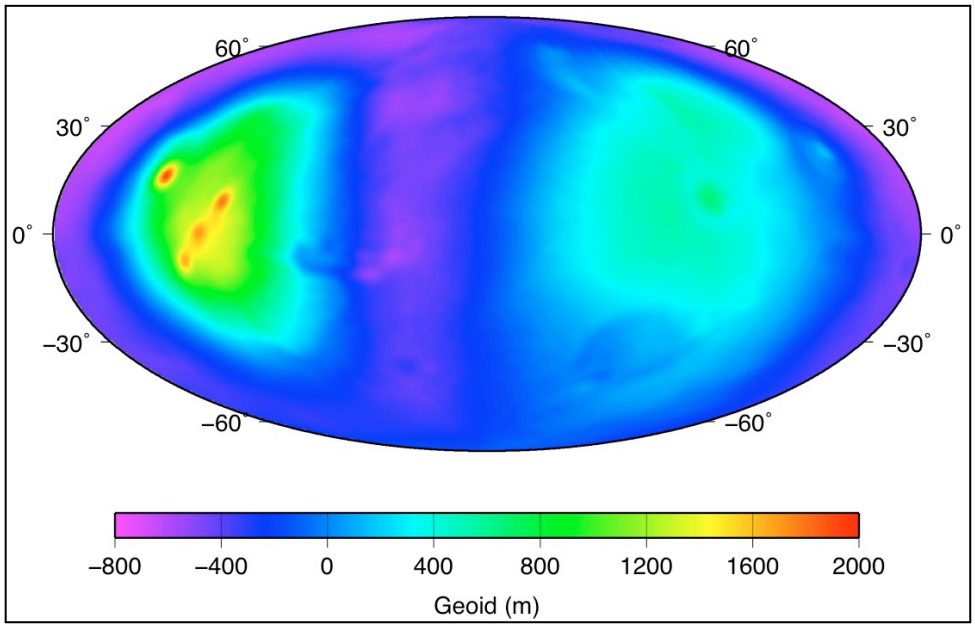

Figure 1.4 The Martian areoid (geoid) is dominated by two large highs. The geoid map was generated from geoid data file jgm95j01.sha.

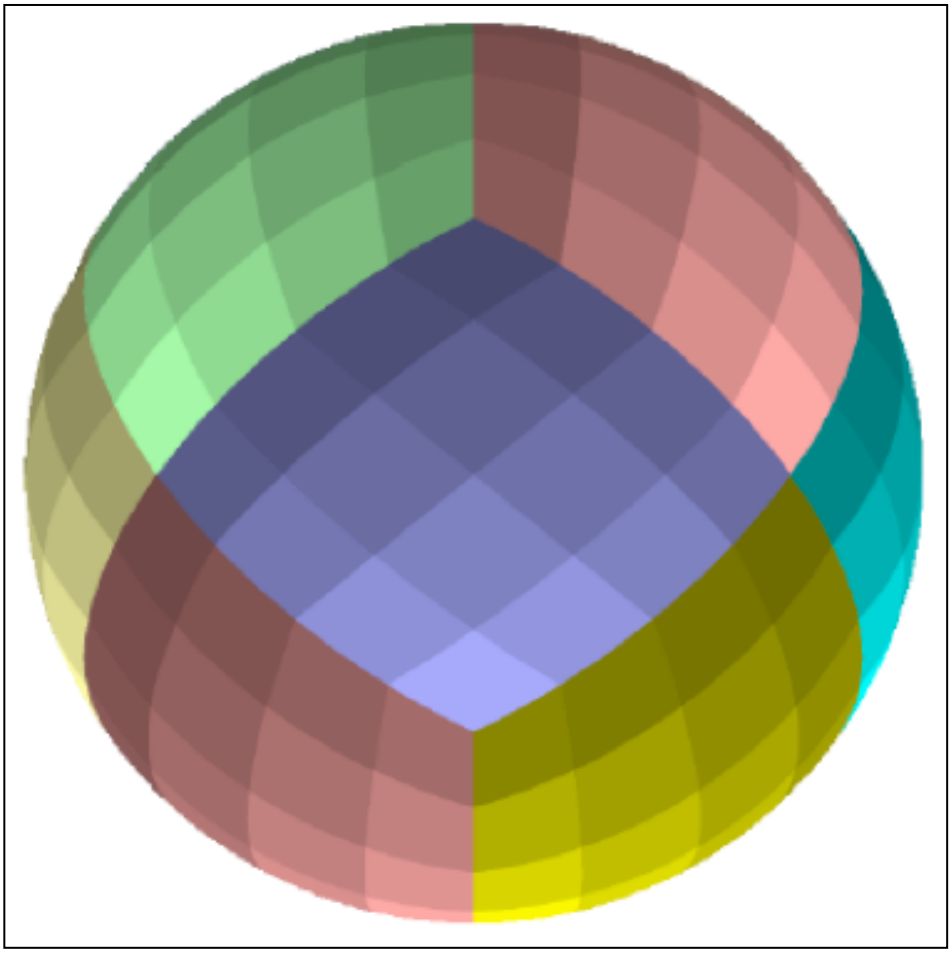

Figure 1.5 3D spherical shell in CitcomS-3.1.1 (after *Tan et al.,* 2009; CitcomS User Manual).

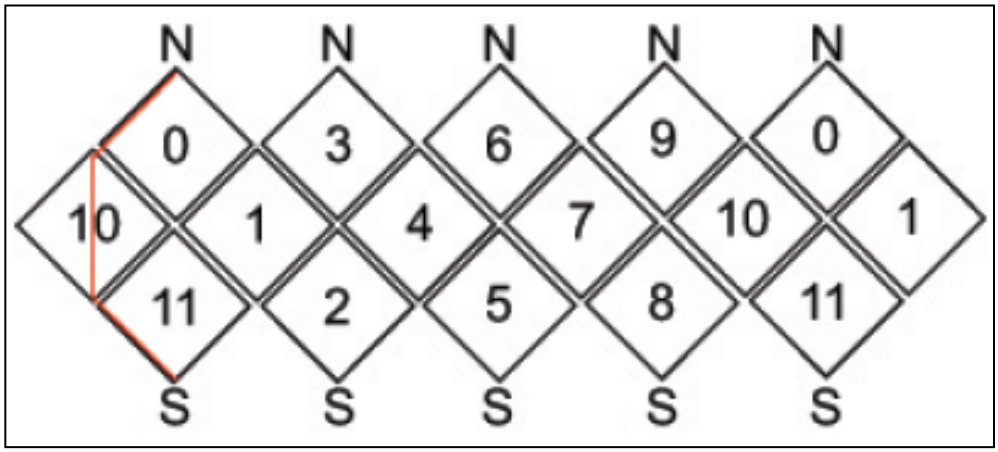

Figure 1.6 12 spherical caps in CitcomS-3.1.1 (after *Tan et al.,* 2009; CitcomS User Manual).

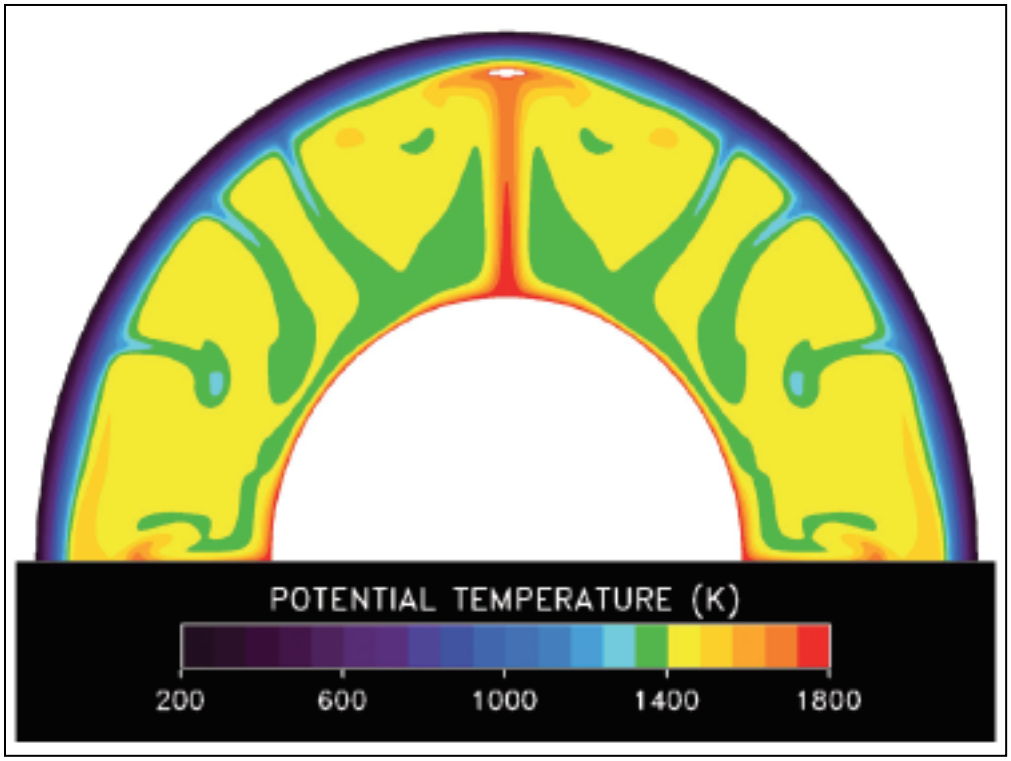

Figure 1.7 Previous 2D asymmetric modeling of plume structure (after *Kiefer*, 2003).

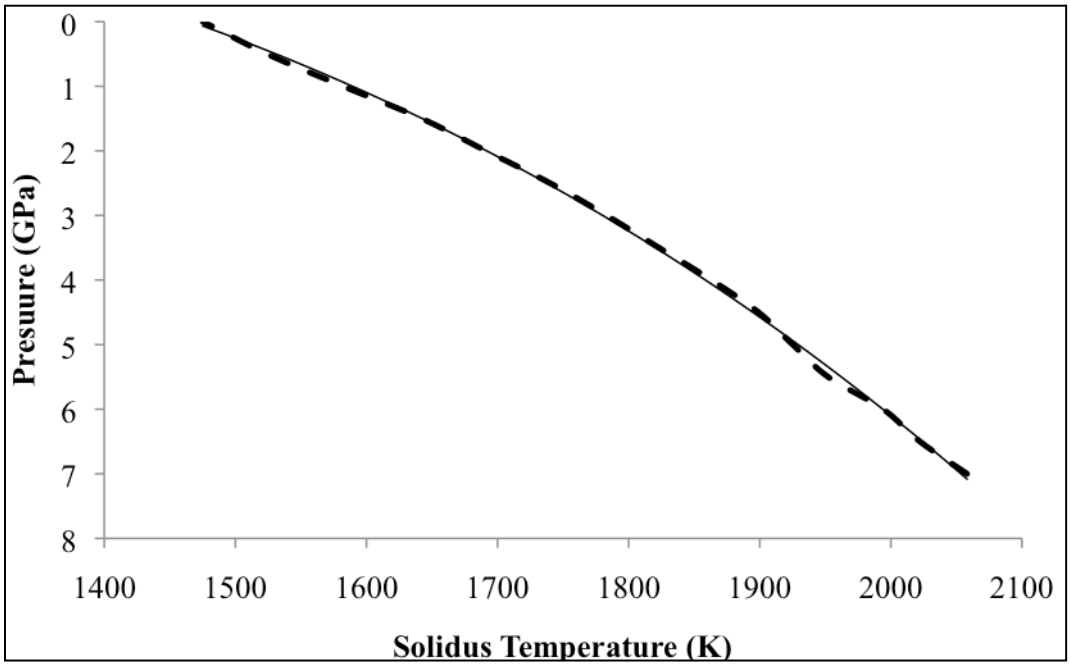

Figure 1.8 Pressure increasing with depth as a function of solidus temperature for Mars composition. The dashed line is the result of *Draper et al.* (2003), followed by *Kiefer* (2003).

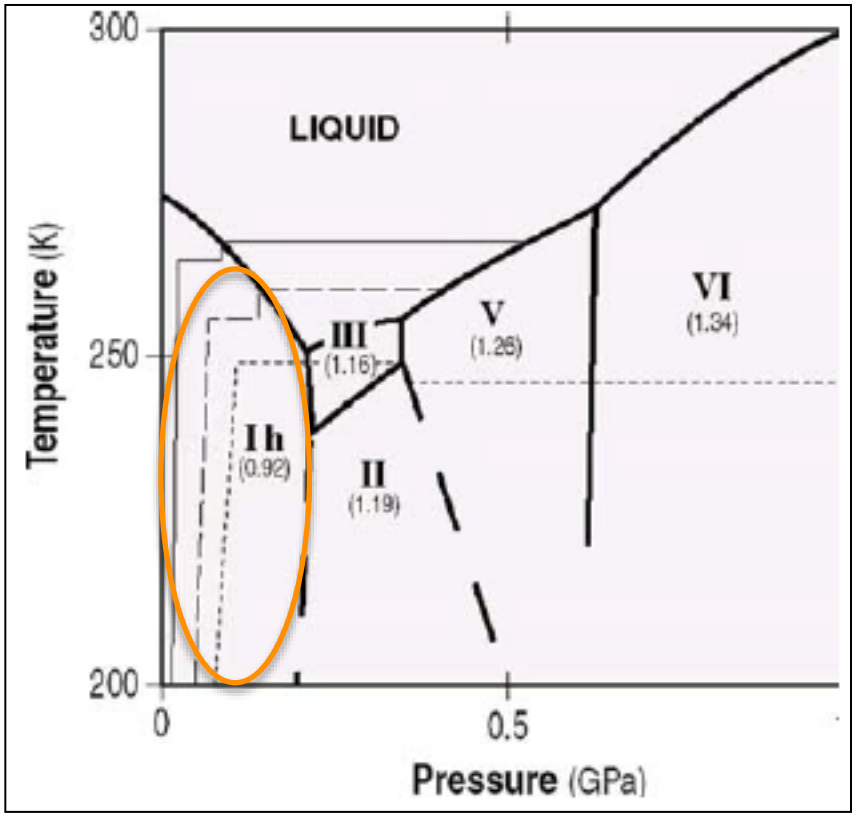

Figure 1.9 Phase diagram of water ice with temperature profiles given by *Sotin et al* (2008). The orange oval is the region of pressure and temperature under consideration for Ceres.

Earth and Planetary Science Letters 388 (2014) 27–37

Contents lists available at ScienceDirect

Earth and Planetary Science Letters

www.elsevier.com/locate/epsl

3D spherical models of Martian mantle convection constrained by melting history

Pavithra Sekhar *, Scott D. King

Department of Geosciences, Virginia Tech, Blacksburg, VA 24061, United States

ARTICLE INFO

Article history:
Received 15 April 2013
Received in revised form 8 November 2013
Accepted 23 November 2013
Available online xxxx
Editor: C. Sotin

Keywords:
mantle convection
melting history
volcanic evolution
Tharsis rise
plume structure
heat sources

ABSTRACT

While most of Tharsis rise was in place by end of the Noachian period, at least one volcano on Tharsis swell (Arsia Mons) has been active within the last 2 Ma. This places an important constraint on mantle convection and on the thermal evolution of Mars. The existence of recent volcanism on Mars implies that adiabatic decompression melting and, hence, upwelling convective flow in the mantle remains important on Mars at present. The thermal history on Mars can be constrained by the history of melt production, specifically generating sufficient melt in the first billion years of the planets history to produce Tharsis rise as well as present day melt to explain recent volcanism. In this work, mantle convection simulations were performed using finite element code CitcomS in a 3D sphere starting from a uniformly hot mantle and integrating forward in time for the age of the solar system. We implement constant and decaying radioactive heat sources; and vary the partitioning of heat sources between the crust and mantle, and consider decreasing core–mantle boundary temperature and latent heat of melting. The constant heat source calculations produce sufficient melt to create Tharsis early in Martian history and continue to produce significant melt to the present. Calculations with decaying radioactive heat sources generate excessive melt in the past, except when all the radiogenic elements are in the crust, and none produce melt after 2 Gyr. Producing a degree-1 or degree-2 structure may not be pivotal to explain the Tharsis rise: we present multi-plume models where not every plume produces melt. The Rayleigh number controls the timing of the first peak of volcanism while late-stage volcanism is controlled more by internal mantle heating. Decreasing the Rayleigh number increases the lithosphere thickness (i.e., depth), and increasing lithosphere thickness increases the mean mantle temperature. Increasing pressure reduces melt production while increasing temperature increases melt production; hence predicting melt production from convection parameters is not straightforward. Generating enough melt in the mantle to create Tharsis early on and also to explain recent volcanism may require other mechanisms such as small-scale convection or lowering the thermal conductivity of the crust.

1. Introduction

The Tharsis region, consisting of the shield volcanoes Olympus Mons, Arsia Mons, Pavonis Mons, Ascraeus Mons and Alba Patera, is one of the most prominent features of Mars. High resolution Mars Orbiting Laser Altimeter (MOLA) topography provides a view of the Tharsis region and its shield volcanoes, showing that this region consists of two rises: the southern rise from 40°S to 20°N which includes Arsia, Pavonis and Ascraeus Mons, and the northern rise which consists of Alba Patera. Unlike the other shield volcanoes, Olympus Mons sits off the western edge of the Tharsis rise (Smith et al., 1999). Previous studies have suggested that one or more plumes could be responsible for the formation of Tharsis (Harder and Christensen, 1996; Kiefer, 2003; Wenzel et al., 2004; Solomon et al., 2005; Zhong, 2009; Sramek and Zhong, 2010).

The relative and absolute ages of surface features can be studied by impact cratering studies (Tanaka, 1986; Tanaka et al., 1992; Hartmann et al., 1999, 2008; Werner, 2009). The southern hemisphere is heavily cratered with older geological features in contrast to the lightly cratered northern hemisphere, possibility due to volcanic resurfacing (Mutch et al., 1976; Carr, 1981; Zuber et al., 2000; Zhong and Zuber, 2001; Frey et al., 2002; Carr and Head, 2010). The northern hemisphere is lower in elevation and has a thinner crust than the southern highlands (Zuber et al., 2000; Neumann et al., 2004; Solomon et al., 2005). However, a number of buried impact basins, known as Quasi-Circular Depressions (QCD), were discovered underneath the surface in the northern hemisphere indicating a basement surface equal in age, if not older than, the southern highlands (Frey et al., 2002).

The southern highlands have abundant valley networks (Phillips et al., 2001) and nearly all of these appear to flow into or

* Corresponding author. Tel.: +1 540 231 8827.
E-mail addresses: pav06@vt.edu (P. Sekhar), sdk@vt.edu (S.D. King).

0012-821X/$ – see front matter
http://dx.doi.org/10.1016/j.epsl.2013.11.047

away from the Tharsis trough, a topographic depression that surrounds Tharsis. These valleys formed after most of Tharsis was emplaced because the Tharsis slope determines the direction of flow. The majority of the valley networks are late Noachian in age, suggesting that Tharsis had formed by Noachian (Phillips et al., 2001), while a few regions have a younger Hesperian age (Smith et al., 1999). The Noachian age suggests that the lithospheric structure underneath Tharsis has remained stable through Mars's evolution (Anderson et al., 2001), with majority of the crust having formed during the early and mid-Noachian (Scott and Tanaka, 1986; Greeley and Guest, 1987; Tanaka and Scott, 1987; McEwen et al., 1999; Anderson et al., 2001; Phillips et al., 2001; Head et al., 2001; Zuber, 2001; Frey et al., 2002; Solomon et al., 2005; Werner, 2008; Carr and Head, 2010).

While most of Tharsis was emplaced during the Noachian period, images from Mars Express shows that a few volcanic regions lack visible craters and these have been interpreted to be areas resurfaced by young lava flows (Plescia, 1990; Hartmann et al., 1999, 2008; Hartmann and Berman, 2000; Berman and Hartmann, 2002; Neukum et al., 2004; Hartmann, 2005; Hauber et al., 2011). It was once believed that volcanism at Elysium province ended prior to 2.2 Gyr, leading to a conceptual model of a one-plume planet (e.g., Harder and Christensen, 1996). However, recent data shows volcanism remained active in the Elysium region into the Amazonian (e.g., Werner, 2009; Carr and Head, 2010). Two mechanisms have been proposed to explain the recent volcanism: decompression melting due to an upwelling mantle plume (Harder and Christensen, 1996; Kiefer, 2003; Redmond and King, 2004; Roberts and Zhong, 2004; Li and Kiefer, 2007; O'Neill et al., 2007; Kiefer and Li, 2009; Grott and Breuer, 2010), or melting due to heat trapped beneath an isolated thick region of crust (Montesi and Zuber, 2003; Schumacher and Breuer, 2007).

Previous work suggested that the pattern of mantle convection on Mars may be dominated by a single, strong upwelling under Tharsis (Harder and Christensen, 1996; Zuber, 2001; Roberts and Zhong, 2004; Zhong, 2009) or multiple plumes (Kiefer, 2003; Li and Kiefer, 2007; Grott and Breuer, 2010). Harder and Christensen (1996) studied Martian mantle convection in a 3D spherical shell. In their calculation, initially several plumes develop and as the model evolves, the weaker plumes die out until finally, only the strongest plume survives. The long duration of the single surviving plume is consistent with the stability of the Tharsis volcanic region. This is quite different from the convection process on Earth where the mobile lithosphere plays an important role with downwelling slabs and multiple upwelling plumes (cf. Schubert et al., 2001).

A number of recent Martian mantle convection investigations have used quasi-steady-state calculations (Kiefer, 2003; Roberts and Zhong, 2006; Li and Kiefer, 2007). Kiefer's work (2003) is based on the Wanke and Dreibus (1994) heating rates and is consistent with present day radioactive element concentrations while Roberts and Zhong (2006) used a much higher internal heating value (Fig. 1). In both cases the value of the internal heating rate was constant with time. Roberts and Zhong (2006) suggested that the single upwelling (i.e., a degree-one structure) could explain the formation of Tharsis; this convective platform requires a strongly temperature/depth-dependent viscosity (Lenardic et al., 2004; Roberts and Zhong, 2004, 2006).

1.1. Melting history

Based on in situ measurements and SNC meteorite isotope data; the planet differentiated around 4.5 Ga, forming a crust, mantle and core (Breuer and Spohn, 2006). Shortly after the formation of the planet, the mantle temperatures were high and melting was prevalent throughout shallow part of the upper mantle, leading to the formation of the crust. As mantle temperatures cooled, most volcanic activity was restricted to two areas: Tharsis and Elysium rises (e.g., Harder and Christensen, 1996). Partitioning of radioactive elements between crust and mantle must have happened when the crust formed, because there appears to be little large-scale modification of the crust after formation. The initial melt would be enriched in radiogenic elements and continued melting will cause depletion of these elements in the mantle (Breuer and Spohn, 2006; Schumacher and Breuer, 2007). If majority of the heat producing elements were not concentrated in the crust, there would be widespread melting of the lower mantle, providing a further constraint on the melt production during the early stages of Mars' formation.

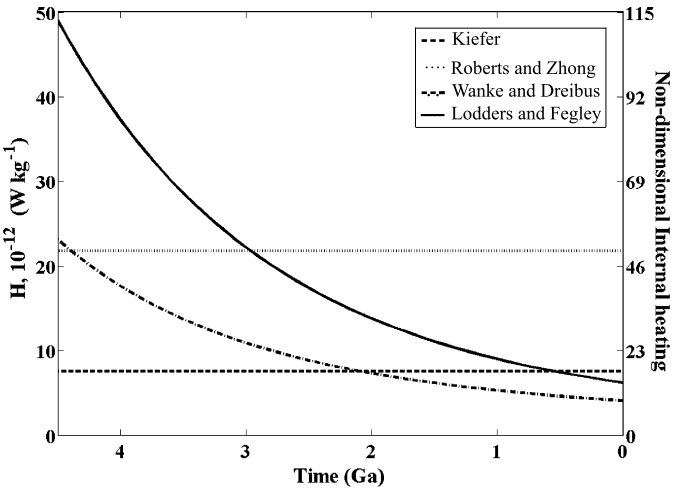

Fig. 1. Rate of internal heating for constant heat sources and decaying heat source as a function of time measured back from present day. Shown are two constant heat sources, Kiefer (2003) and Roberts and Zhong (2006), and two decaying heat sources, Wanke and Dreibus (1994) and Lodders and Fegley (1997).

In this study, numerical models are constrained by the conceptual model for the development of Tharsis by a mantle plume with the timing above. The partitioning of radioactive elements between the crust and the mantle has a significant impact on mantle temperature, which in turn affects melt production (e.g., Kiefer, 2003). The concentration of radioactive elements in the crust and mantle is still unclear; however 50% of the total radiogenic material is probably in the crust (McLennan, 2001). We seek to identify a region of parameter space that allows sufficient melt to produce most of Tharsis region by the end of Noachian, with small amounts of melt continuing to present. We do not consider the problem of how melt is extracted from the mantle, as this is a challenging unresolved problem and beyond the resolution of global models.

2. Numerical method

Mantle convection on Mars is currently in the stagnant-lid convection regime (Solomatov, 1995; Solomatov and Moresi, 1996, 2000; Reese et al., 1998, 1999, Grasset and Parmentier, 1998). We consider a Newtonian rheology with a strong temperature-dependent viscosity and a layered viscosity structure that includes a viscosity increase by a factor of 8 and 25 at a depth of 996 km (Roberts and Zhong, 2006). We consider both a constant heating rate and heating rate that decreases with time due to the decay of long-lived radioactive isotopes. The former is determined by the temperature difference between the mantle and core, while the latter is determined by the partitioning of radioactive material between the mantle and the crust. A crust thickness of 55 km is used for partitioning of the heat producing elements. We do not have a compositionally distinct crust. We implement latent heat

Table 1
Model parameters.

Parameter	Symbol	Value
Default internal heating rate	Q	7.4×10^{-8} W m^{-3}
Planetary radius	R_p	3.398×10^6 m
Density of the mantle	ρ_m	3.40×10^3 kg m^{-3}
Specific heat	C_p	1200 J K^{-1} kg^{-1}
Temperature difference across the mantle	ΔT	1600 K
Thermal diffusivity	κ	10^{-6} m^2 s^{-1}
Gravitational acceleration	g	3.72 m s^{-2}
Thermal expansion coefficient	α	3.0×10^{-5} K^{-1}
Reference viscosity	η_0	10^{21} Pa s
Activation energy	E	157 kJ mol^{-1}
Universal gas constant	R	8.3144 J K^{-1} mol^{-1}
Activation volume	V	3.61×10^{-6} m^3 mol^{-1}
Surface temperature	T_{surf}	220 K
Latent heat of melting	H_l	6.4×10^5 J kg^{-1}

of melting and also a decreasing core–mantle boundary temperature following Hauck and Phillips (2002) for decaying heat source models. The calculations are performed in a 3D spherical shell with a free-slip cold upper boundary and a stress-free core–mantle boundary. The calculations begin with a conductive boundary layer at the surface and an initial non-dimensional mantle temperature of 0.95 with an error function temperature profile for the top thermal boundary layer (250 Myr). A perturbation of 0.01 is added to the radial temperature with a spherical harmonic $l = 50$, $m = 42$ pattern. We fix the surface temperature at 220 K while the core–mantle boundary is at 1820 K at a depth of 1780 km. The calculations begin at 4.3 Ga, corresponding to the end of formation of the crustal dichotomy. While this is clearly oversimplifying the early history of Mars, it avoids the complexity of the melt forming the initial crust and allows us to focus on melt generated from upwelling plumes.

The calculations were performed using the finite element code CitcomS-3.1.1 (Zhong et al., 2000, 2008; Tan et al., 2006) with $65 \times 65 \times 65$ element in each of the 12 spherical caps. CitcomS solves the equations of conservation of mass, momentum and energy for a creeping, incompressible fluid. Using a Boussinesq approximation, these equations are given by:

$$\nabla.\vec{u} = 0 \tag{1}$$

$$-\vec{\nabla}P + Ra\,T\vec{e}_r + \vec{\nabla}\left(\eta\left(\nabla\vec{u} + \nabla\vec{u}^T\right)\right) = 0 \tag{2}$$

$$\frac{\partial T}{\partial t} + \vec{u}.\vec{\nabla}T = \nabla^2 T + H_{int} - H_L \tag{3}$$

where u, P, T, and η are the velocity vector, dynamic pressure, temperature and viscosity respectively. Ra is the Rayleigh number, H_{int} is the non-dimensional internal heating rate (which may be a function of time) and H_L is the non-dimensional latent heat of melting. H_L is the product of melt production rate and dimensional latent heat of melting, H_l (Table 1). Eqs. (1), (2) and (3) are governed by two dimensionless numbers: Rayleigh number, Ra, and internal heat parameter, H_{int}. Rayleigh number is the ratio of the buoyancy of a fluid to the viscous stresses resisting motion and is given by,

$$Ra = \frac{\rho_m g \alpha \Delta T R_p^3}{\kappa \eta_0} \tag{4}$$

where ρ_m, g, α, ΔT, R_p, κ and η_0 are the mantle density, gravitational acceleration, thermal expansion coefficient, super-adiabatic temperature difference across the mantle, planetary radius, thermal diffusivity and mantle viscosity respectively (Table 1). The initial temperature difference across the mantle is 1600 K (Kiefer, 2003) and the other parameters and their values are given in Table 1. Present-day Martian mantle viscosity is probably comparable to Earth's viscosity, approximately 10^{21} Pa s (Lenardic et al., 2004).

In addition to the Rayleigh number, the equations are governed by the non-dimensional internal heating parameter given by,

$$H_{int} = \frac{Q R_p^2}{\rho_m C_p \Delta T \kappa} \tag{5}$$

where Q and C_p are the heat per unit volume and specific heat at constant pressure respectively (Table 1). The default internal heating rate is 7.4×10^{-8} W m^{-3} for early Mars (Roberts and Zhong, 2006) based on chondritic composition or 9.75×10^{-9} W m^{-3} for present-day Mars (Kiefer, 2003) (Fig. 1).

The non-dimensional pressure and temperature-dependent viscosity, η', is given by (e.g. Roberts and Zhong, 2006),

$$\eta = \eta'(r) \exp\left[\frac{E' + V'(1-r)}{(T+T_s)} + \frac{E' + V'(1-r_{core})}{(1+T_s)}\right] \tag{6}$$

where $\eta'(r)$ is the temperature and pressure dependent radial viscosity profile, r and T are the non-dimensional radius and temperature, respectively and r_{core} is the non-dimensional radius of the core. The non-dimensional parameters E', V' and T_s are normalized using,

$$E' = \frac{E}{R\Delta T}, \qquad V' = \frac{\rho_m g R_p V}{R\Delta T}, \qquad T_s = \frac{T_{surf}}{\Delta T} \tag{7}$$

where E, R, V and T_{surf} are the activation energy, universal gas constant, activation volume and surface temperature respectively (Table 1). At the pressures of the Martian interior, mantle deformation is likely dominated by diffusion creep (Grott and Breuer, 2009).

Plumes arise from a hot thermal boundary layer at the base of the convecting mantle and thus the temperature drop between the core and mantle will control plume dynamics. The lack of an internally generated magnetic field may indicate a low heat flow from the core into the mantle hence small thermal boundary layer at the core–mantle boundary (Nimmo and Stevenson, 2000), while the presence of a long-lived plume requires a significant thermal boundary layer at the core–mantle boundary. In our decaying models, core cooling allows the temperature across the core–mantle boundary to decrease by 15% from the initial temperature condition (or 240 K), over a span of 4.5 Gyr (Hauck and Phillips, 2002).

2.1. Radioactive heat sources

While in many mantle convection studies, the heat source term, H_{int} from Eq. (5), is taken to be constant with time, here we use a heat source as a function of time based on the concentration of radioactive material from the Martian meteorite studies (Wanke and Dreibus, 1994) or a combination of CI, CV and H chondrites (Lodders and Fegley, 1997). Table 2 shows the abundance of radioactive material for bulk silicate Mars for these two compositions. The two main heat producing radioactive elements, Uranium and Thorium are the same for both the models while Potassium is higher by a factor of 3 for the Lodders and Fegley model.

The mean heat production rate of the mantle in the past can be related to present day heat production using the half-lives of radioactive isotopes like U, Th and K where natural uranium is composed of 99.28% by weight ^{238}U and 0.71% ^{235}U, natural thorium is 100% ^{232}Th and natural potassium is 0.0119% ^{40}K. The concentration of these isotopes is calculated by integrating backward from present day values (Turcotte and Schubert, 2002). The internal heating values for the constant heat source models from Kiefer (2003) and Roberts and Zhong (2006) along with the decaying heat source models Lodders and Fegley (1997) and Wanke and Dreibus (1994) are shown in Fig. 1.

Table 2
Rate of Heat Release, H and Half-Lives, $\tau_{1/2}$ of the important radioactive isotopes for the two Mars models, Wanke and Dreibus (1994) and Lodders and Fegley (1997).

Isotope	H ($W\,kg^{-1}$)	$\tau_{1/2}$ (yr)	Concentration C ($kg\,kg^{-1}$)	
			Wanke and Dreibus	Lodders and Fegley
^{238}U	9.46×10^{-5}	4.47×10^{9}		
^{235}U	5.69×10^{-4}	7.04×10^{8}		
U	9.81×10^{-5}		16.0×10^{-9}	16.0×10^{-9}
^{232}Th	2.64×10^{-5}	1.40×10^{10}	56.0×10^{-9}	56.0×10^{-9}
^{40}K	2.92×10^{-5}	1.25×10^{9}		
K	3.48×10^{-9}		30.5×10^{-5}	92.0×10^{-5}

2.2. Melt calculations

We follow Kiefer's (2003) method to calculate the melt from the resulting pressure and temperature fields of our calculations. First, the non-dimensional temperature, T_{nd}, is converted to dimensional temperature, T_{dim} using,

$$T_{dim} = T_s + T_{nd}\Delta T + (1-r)T_{ad} \tag{8}$$

where ΔT and T_s are explained in Eqs. (4) and (7), $(1-r)$ is the depth of the mantle, and T_{ad} is the adiabatic gradient in the mantle, assumed to be 0.18 K/km (Kiefer, 2003). The pressure is calculated using the hydrostatic approximation, $P = \rho g(1-r)$.

The solidus temperature was plotted as a function of pressure and best fit line was a third order polynomial. This was done by using the values of the high-pressure solidus of the Martian mantle from Bertka and Holloway (1994). Bertka and Holloway calculated the partial melting using the mantle composition of Wanke and Dreibus (1994). Bertka and Holloway had the lowest dry melting solidus for a Mars-analogue composition.

The melt production rate is then calculated by comparing the dimensional temperature values from Eq. (8) with the melt solidus and the percentage of melt, F, is given by the following equation,

$$F = (T_{dim} - T_{solidus}) * 0.005 \tag{9}$$

Because there are few constraints on the production of melt above the solidus at high pressure, we assume that melt productivity varies linearly with temperature above the solidus. Based on terrestrial peridotite studies by Takahashi et al. (1993) and Martian meteorite studies at high pressures by Agee and Draper (2004), we assume the average melt productivity to be about 0.5% per degree ($0.005\ K^{-1}$) above the solidus (Kiefer, 2003).

3. Results

We present two sets of calculations: one set with an internal heating rate that is constant with time and one set with internal heating rates based on the decay of radioactive elements using the concentrations in Lodders and Fegley (1997). For the constant heat source calculations, we compare our 3D spherical convection calculations with the 2D axisymmetric hemispherical convection calculations from Kiefer (2003). We also test the effects of varying fraction of radiogenic elements between the crust and the mantle, and compare different depth-dependent viscosity models. We focus on the mantle structure early in Martian history, around 4.0 Ga and close to present day, approximately around 0.2 Ga.

In addition to searching for parameters that produce stable low-degree structures, we estimate the melt production, globally and locally, and compare that to the volume of Tharsis swell. The volume of melt required to create Tharsis is calculated by multiplying the surface area of the Tharsis region, one-third of the surface of Mars, with the average thickness of the Tharsis region. The amount of melt, calculated from this, is around $1–3 \times 10^8$ km^3 (e.g., Solomon and Head, 1982; Zuber et al., 2000; Phillips et al., 2001). Tharsis was set in place during the Noachian era, around 3.5–3.8 Ga (Tanaka, 1986; Wenzel et al., 2004) suggesting that the melt production rate is 0.36 km^3/yr with an uncertainty of an order of magnitude. As for mid-ocean ridge calculations in Earth's mantle, we assume that approximately 10% of the melt created in the mantle reaches the surface (Klein and Langmuir, 1987).

3.1. Constant heat source calculations

We begin with 3D spherical calculations with the Rayleigh number and internal heating value (Table 3) chosen to reproduce one of the 2D axisymmetric calculations in Kiefer (2003). Kiefer's 2D calculations used a depth-dependent viscosity model designed to capture the radial changes in viscosity that would result from a temperature-dependent viscosity calculation. These calculations produced a single strong upwelling along the axis of symmetry and several downwelling drips off-axis. The single plume had an elevated temperature anomaly and region of melting was restricted to the head of the plume.

In contrast to Kiefer's 2D axisymmetric calculation, our 3D temperature-dependent spherical shell calculation, PS1, produces a number of plumes with correspondingly smaller temperature anomalies in each plume (Fig. 2a and 2c). This is easy to understand because the heat carried from the core–mantle boundary in the 3D case is distributed across of order 10 smaller plumes and not concentrated in one large upwelling structure as in the axisymmetric case. The large number of plumes produced in our calculation and small amount of global melt is inconsistent with the observation of concentrated volcanism at the Tharsis and Elysium rises. Thus we search parameter space for calculations that produce fewer plumes that would be capable of carrying enough heat to produce melt sufficient to create the Tharsis rise. Following Roberts and Zhong (2006), we consider 3D temperature-dependent calculation, PS2, with a slightly lower Rayleigh number and higher

Table 3
Model parameters for Constant and Decaying heat sources. The early and late time steps correspond to the respective isotherm structures of the constant and decaying heat source models from Figs. 2, 5 and 6.

Case	*Ra*	H_{in} for constant heat source	Partitioning of radioactivity (Crust fraction)	$\eta_{lower}/\eta_{upper}$	Early time (Myr)	Late time (Myr)
PS1	4.08e7	17.25	–	1:1	4190	69
PS2	2.24e7	49.66	–	1:8	4088	114
PS3	1.25e8	49.66	–	1:8	–	–
PS4	2.24e6	49.66	–	1:8	–	–
PS5	2.24e6	33.50	–	1:8	–	–
SK1	2.24e7	–	100	1:8	4076	255
SK2	2.24e7	–	60	1:8	3870	263
SK3	2.24e7	–	0	1:8	4118	338
SK4	2.24e7	–	60	1:25	4064	296

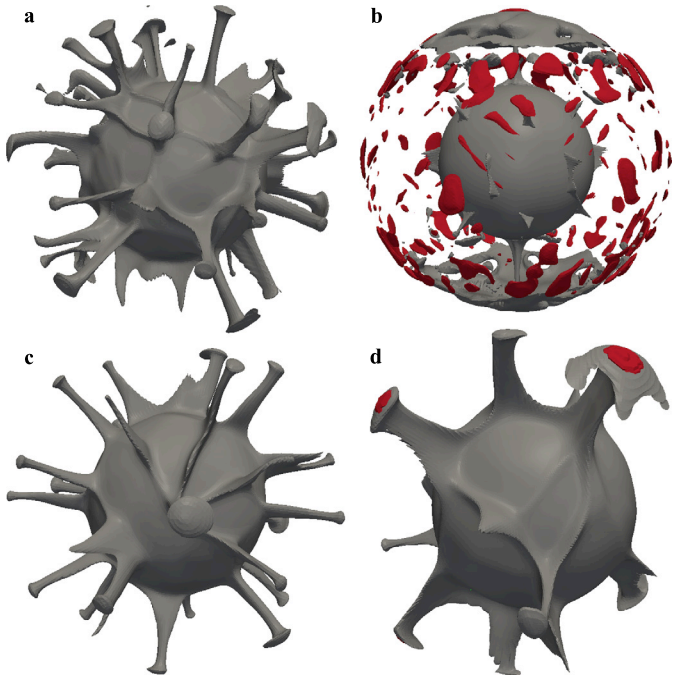

Fig. 2. 3D calculations and melt location for the constant heat sources during early formation, around 4 Ga and also during the late stages, around 0.08 Ga. The isothermal spherical plots for PS1 (a) early and (c) late stages and PS2 (b) early (0.4 Ga) and (d) late stages (0.1 Ga) are shown. All the early formation plots are taken at a non-dimensional temperature of approximately 0.95 that corresponds to a dimensional temperature of 1740 K. While the late-stage plots are set at a temperature of approximately 0.85 that corresponds to 1580 K on a dimensional scale. Melt is shown in red. (For interpretation of the references to color in this figure legend, the reader is referred to the web version of this article.)

internal heating rate than PS1, and we increase the mantle viscosity by a factor of 8 at a depth of 996 km (Table 3). The higher internal mantle heating value leads to an increase in mean mantle temperature and the plumes that rise from the boundary layer cool less as they reach the base of the lithosphere. These broader plumes with localized melt in this 3D calculation (Figs. 2b and 2d) are similar to Kiefer's 2D axisymmetric model. Early on we find a two-plume structure that evolves with time to a structure with more plumes that have lower temperature anomalies.

Fig. 3 shows the melt production rate for the constant heat source models. We focus on the melt production after the crustal dichotomy was formed, to explain Tharsis and Elysium. We compare the melting rate to 3.6 km^3/yr (i.e., 1.08e8 km^3 for 300 Myr with 10% melt reaching the surface). In PS1, there are two peaks in melt production at 4.25 Ga and 4.2 Ga and melt production ceases after 4.1 Ga. The heat is distributed among multiple plumes. In the case of PS2, the melt production is approximately 5300 km^3/yr at around 4.1 Ga and decays quickly within 4.0 Ga. As the model progresses, the amount of melt produced still exceeds the amount required to create Tharsis and continues to 15 km^3/yr during present day. The melt production in this case is excessive and also occurs at a slightly delayed time compared to PS1. PS2 produces fewer plumes and they are broader with stronger temperature anomalies with greater melt production in the plume heads.

Both of these models produce orders of magnitude more melt early on than what is needed to produce the Tharsis rise. Thus we consider several calculations where we vary the Rayleigh number, by changing the scaling viscosity and keeping the other parameters fixed in order to assess the impact on melt production. With PS2 as the base model, we vary the Rayleigh number to a higher and lower limit of 1.25×10^8 (PS3) and 2.24×10^6 (PS4). The peak in the melting curve occurs later in the calculation as the Rayleigh number decreases. In comparing PS3 and PS2, the peak of the melting curve decreases with decreasing Rayleigh number. However, there is an enormous spike in the melt production for PS4. The timing of peaks in melt production corresponds to the time for the onset of instability in a thermal boundary layer and scales as $\eta^{2/3}$ (Olson et al., 1987). The delay in instability for PS3 is 0.05 Gyr, PS2 is 0.21 Gyr and PS4 is 0.92 Gyr. The ratio between the time of peaks (Fig. 3) are PS2/PS3 = 4.2 and PS4/PS3 = 18.4 which compares with onset time ratios of $(10^{21}/1.91 \times 10^{20})^{2/3} \sim 3.14$ and $(10^{22}/1.91 \times 10^{20})^{2/3} \sim 14.6$ from Olson et al.s theory.

At first the change in behavior in melt production as a function of time seems puzzling, but upon further reflection, melt production depends on both temperature and pressure. The mean mantle temperature and the pressure at which melt occurs (i.e., depth to melting controlled by the thickness of the lithosphere) are impacted by the Rayleigh number in ways that have an opposite

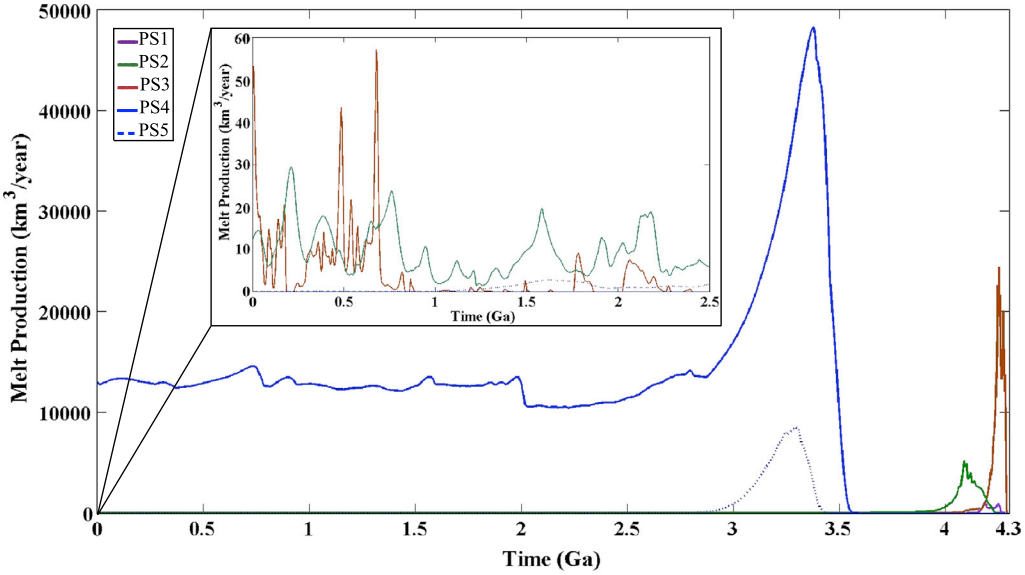

Fig. 3. The melt production rate for constant heat sources with varying Rayleigh numbers and internal heating values. The time scale begins at 4.3 Ga (i.e., after the formation of the crustal dichotomy) and 0 represents present day Mars. The inset figure focuses on present day volcanic activity.

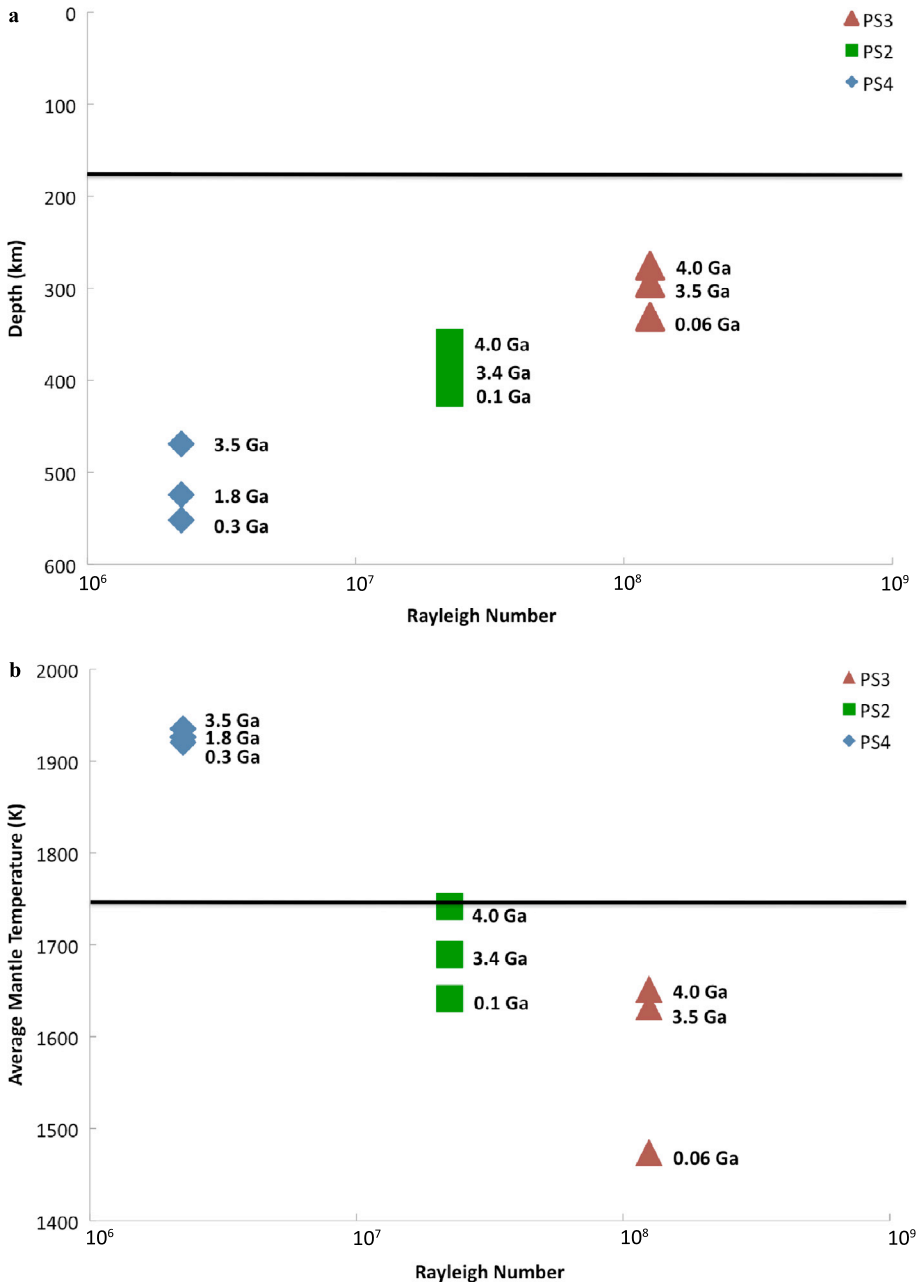

Fig. 4. (a) The thickness of the lithospheric lid for varying Rayleigh numbers. The evolution of the lid with time is shown by the age scale right next to the symbols. The black line is the initial lid thickness. (b) The average mantle temperature for varying Rayleigh numbers. Similar to (a), the evolution of the lid with time is shown by the age scale right next to the symbols. The black line depicts the initial average mantle temperature.

effect on melting. Increasing temperature, while holding pressure constant, increases the amount of melt once above the melting temperature (Eq. (9)). On the other hand, increasing pressure increases the melting temperature and thus for a given temperature decreases the melt.

The impact of the thickness of the lithospheric lid as a function of Rayleigh number for the three calculations, PS3, PS2 and PS4 is shown in Fig. 4a. The thickness of the lid is calculated by calculating the radially-averaged temperature profile for the calculation at each time and measuring the inflection point where the curve transitions from an increasing temperature with depth to a nearly isothermal interior. Because melting in these calculations is restricted to the plume heads, which do not significantly penetrate into the lithospheric lid, this is a first-order control on the pressure of melting. The range of values for each Rayleigh number shows how the lithospheric lid thickness changes with time throughout the calculations. Hence, we observe an increase in lid thickness as Rayleigh number decreases.

In contrast, the average mantle temperature as a function of Rayleigh number is shown in Fig. 4b. While there is little change in the average mantle temperature between PS3 and PS2, the average mantle temperature increases significantly for PS4. This is because the thicker boundary layer is less effective at conducting heat through the surface. The significant increase in mantle temperature for PS4 is consistent with the significant increase in the melt production.

Due to the unrealistic melt production in PS4, we compute a final calculation, PS5 (Fig. 3), where the internal heating value is reduced from 49.66 to 33.50 while maintaining the same Rayleigh number. This reduces the amount of melt produced and maintains the delay in the peak of melt production, illustrating the sensitivity of the melt production to the internal mantle heat (e.g., Kiefer,

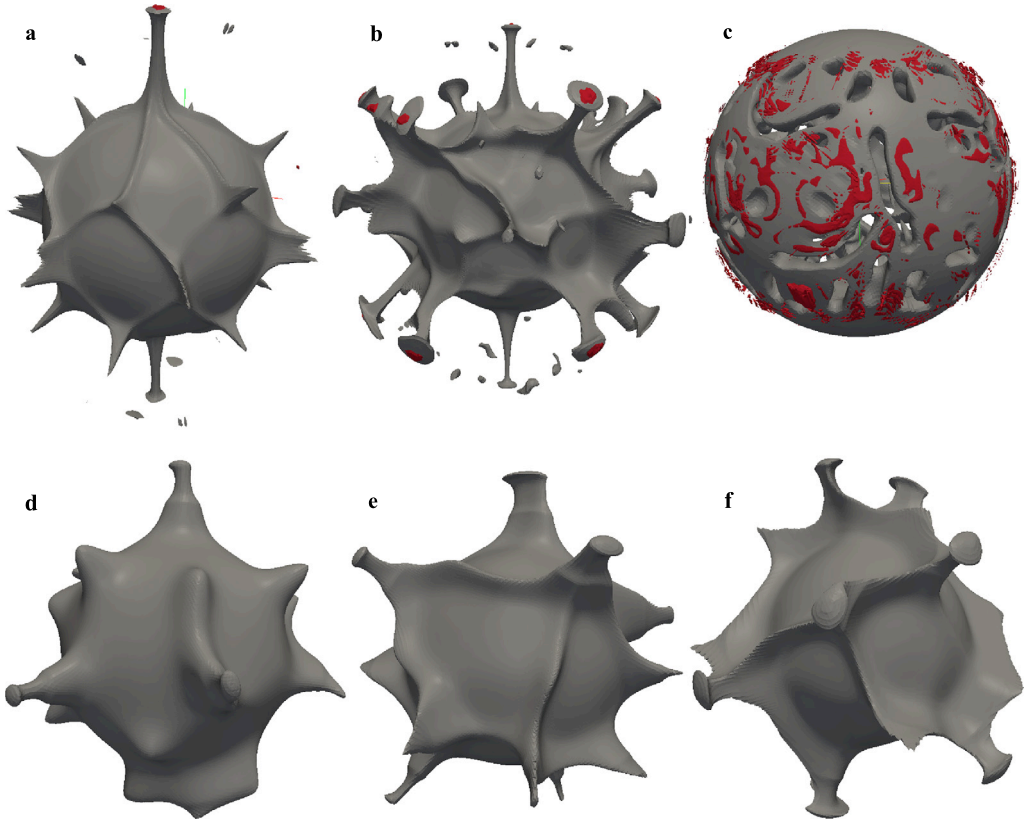

Fig. 5. Convection calculations and melt location for the decaying heat sources with different amounts of partitioning and layered viscosity. Shown are the isothermal structures for (a) SK1, (b) SK2 and (c) SK3 at approximately 4 Ga and (d) SK1, (e) SK2 and (f) SK3 at 0.3 Ga respectively. The isothermal structure is maintained at approximately 0.98 that corresponds to 1788 K for early stages and 0.75 that corresponds to 1420 K for late stages and depict upwelling in all the cases. Melt is shown in red. (For interpretation of the references to color in this figure legend, the reader is referred to the web version of this article.)

2003). Since, the melt production of the constant heat sources is inconsistent with the observations, we will move onto cases with decaying radioactive heat sources and a cooling core boundary condition.

3.2. Varying heat source calculations

Based on the difference between the melt produced in the previous calculations we speculate that the decrease in internal heating through time could change melt production with time. The decaying heat sources are based on the concentrations of uranium, thorium and potassium from Lodders and Fegley (1997). The higher amount of potassium in the Lodders and Fegley (1997) model led us to implement this model.

Even though potassium is a minor contributor to the total radioactive heat production, the Lodders and Fegley (1997) heat production rate is significantly larger than the Wanke and Dreibus (1994) rate due to potassium, early in Martian history (Fig. 1). Varying the partitioning of radioactive elements between the crust and the mantle plays an important role in the temperature structure of the mantle and the formation of a low-degree structure. For the cases where we consider decreasing radioactive heat source abundance with time, we also include a decreasing core–mantle boundary temperature with time, based on the results of Hauck and Phillips (2002).

The results presented here use the two-layered viscosity structure following Roberts and Zhong (2006). The ratio of the upper to lower layer viscosity and the fraction of radioactivity partitioned between the crust and the mantle are given in Table 3. All the models have a strongly varying temperature-dependent viscosity. The first three models, SK1, SK2 and SK3 have a viscosity increase by a factor of 8 and the last model, SK4, has an increase by a factor of 25 at a depth of 996 km, corresponding to the pressure at which phase transition occurs between olivine and spinel. On Earth, a viscosity jump at this pressure is inferred based on long wavelength geoid (Hager and Richards, 1989). The difference between SK1, SK2 and SK3 is the partitioning of radioactive elements between the crust and the mantle. The fraction of radioactive elements in the mantle is 0%, 40% and 100% as we move from SK1 to SK3. SK4 has the same partitioning as SK2.

An isosurface of temperature for models SK1, SK2 and SK3 is shown in Fig. 5. For SK1, with 0% of the radioactive elements in the mantle, a prominent degree-two structure with many smaller plumes forms early on, around 4 Ga. The low rate of internal heating causes the low-degree structure to evolve into a final planform of many smaller plumes by 0.3 Ga. Increasing the fraction of radioactivity in the mantle, SK2 (40%), give rise to a multiple-degree structure by 3.8 Ga. It finally evolves to a multiple-plume planform with a few ridge structures. For SK3 (100%), the mantle temperature is so high that it is hard to observe the internal structure. This model heats up gradually and it cools down to a multiple-degree structure with a more prominent ridge feature across the mantle. Increasing the fraction of radioactive elements in the mantle increases the mean mantle temperature and reduces the temperature gradient across the core–mantle boundary. The isotherm of SK4, the high viscosity model, is shown in Fig. 6. SK4 (40%), produces a multiple plume structure that has two prominent plumes and a number of smaller plumes initially. As the calculation evolves, it settles into a multiple plume and ridge structure.

Fig. 7 shows melt production as a function of time for all the decaying heat models. Again, our calculations focus on the time period after the formation of the initial crust of Mars and the melt production rate is compared to what is needed to produce the

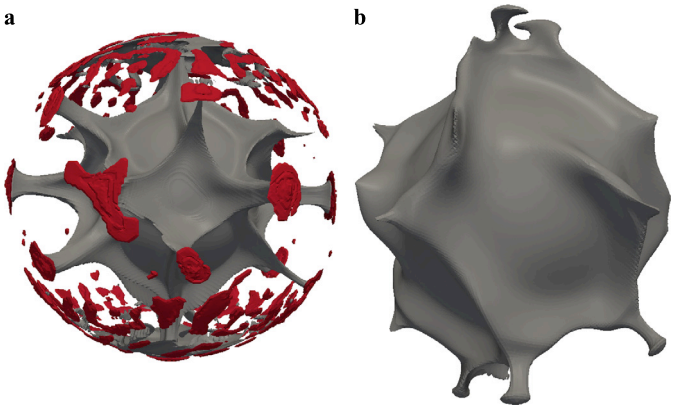

Fig. 6. Convection calculations and melt location for SK4, with much higher viscosity at the lower mantle. Shown are the isothermal structure at (a) 4 Ga, and (b) 0.3 Ga respectively. The isothermal structure is maintained at 0.98 initially and at 0.75 for late stages that corresponds to 1788 K and 1420 K respectively and depicts upwelling's in all the case. Melt is shown in red. (For interpretation of the references to color in this figure legend, the reader is referred to the web version of this article.)

Tharsis region over a time span of 300 Myr. The peak melt production occurs at the earliest stage in all the models, suggesting that a plume forms almost immediately.

SK1 produces 0.25 km^3/yr of melt around 4.2 Ga and a small pulse of melt, approximately 0.15 km^3/yr at 4.1 Ga, before shutting down completely. The melt in calculation SK1 is confined to the two small plume heads (Fig. 6) and is not sufficient to create Tharsis, even if 100% of the melt in the mantle reached the surface or underplated the crust. SK2 produces 10 km^3/yr of melt around 4.1 Ga and random pulses of melt continue till 3.6 Ga before dying out. The majority of the melt in SK2 is confined to the head of multiple plumes but not necessarily all the plume heads (Fig. 6). For SK3, mantle temperatures are higher thereby increasing the melt production and producing melt for a longer period of time. SK3 produces a peak of 110 km^3/yr around 4.1 Ga and decreases steadily until about 2.5 Ga, before ceasing all production. SK3 produces a globally-distributed melt layer early in the model and melt is not restricted to the thermal structures (Fig. 6).

In an effort to further reduce the multiple plume planform, we consider SK4. SK4 follows a similar pattern to its low viscosity counterpart SK2. It produces 10 km^3/yr melt around 4.1 Ga and decaying pulses of melt at 3.7 Ga, 3.6 Ga and 3.4 Ga, these pulses being below the amount needed to create Tharsis. SK4 has a slightly larger melt production curve than SK2 but dies out around 3.0 Ga, similar to SK2. In the case of SK4, the majority of the melt is confined to the dual-plume structure with smaller amounts of melt in the remaining plume heads (Fig. 6). SK2, SK3 and SK4 produce sufficient melt to produce the Tharsis rise early in Mars history. All these calculations cease to produce melt around 2 Ga.

Fig. 8 shows the radial temperature and viscosity profiles for the low viscosity decaying heat models. Fig. 8a shows the decrease in lithospheric lid thickness from SK1 to SK3 (increasing radiogenic elements in mantle), during the late stages. The core cooling at a depth of 1780 km is also visible in the temperature profile. While not shown, SK4 follows the same temperature depth profile as SK2. Fig. 8b shows how the viscosity profile varies between SK1 and SK3. The biggest difference is observed in the lithospheric thickness, again during the late stages, and the viscosity jump is shown at 996 km. SK1 has the least convective solution and cools down to an almost conductive profile while SK3 maintains the most vigorous convective profile and shows the least amount of change in the viscosity profile. SK4 follows a similar profile to SK2 except for a higher viscosity jump at 996 km. The viscosity at 1780 km is higher for the high viscosity than the low viscosity decaying heat source models.

4. Discussion

The constant heating rate models illustrate the strong effect of internal heating rate on melt. The low internal heating rate model, PS1 produces a pulse of melt early but no melt at present day while the high internal heating rate model, PS2 produces a significant amount of melt around 4.2 Ga and continues to produce melt to present day. While the low internal heating rate model produces a global layer of melt early, the high internal heating rate model produces isolated blobs of melt on plume heads during the late stages.

Lowering the Rayleigh number affects the timing of the melt production but this effect is not linear. As we lower the Rayleigh

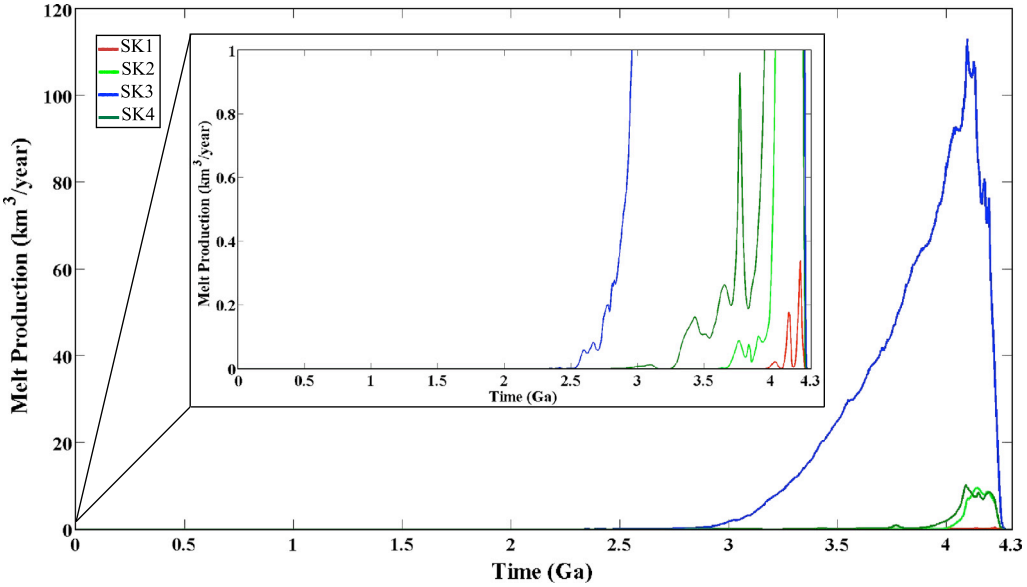

Fig. 7. The melt production rate for the decaying heat sources, both, low and high viscosity models. The time scale is similar to Fig. 4 where 4.3 Ga represents the beginning of our model and 0 represents present day Mars. The inset figure focuses on the melt production on a smaller scale to understand the magnitude of melt in better detail.

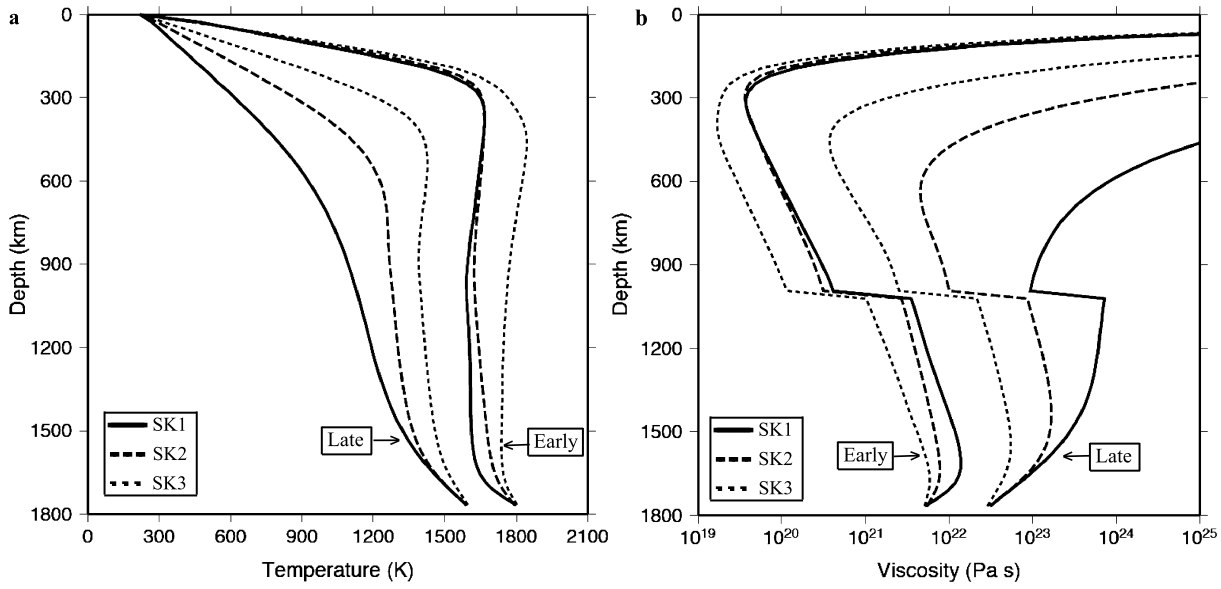

Fig. 8. Radial (a) temperature and (b) viscosity profile for the low viscosity decaying heat source models, SK1, SK2 and SK3, during early and late stages of the planet's evolution.

number, we observe that the initial pulse of melt occurs later in the model evolution. As for the magnitude of the melt production, there is a tradeoff between pressure and temperature. As we lower the Rayleigh number, the lid thickness increases and halts the rise of the plume head at the base of the lithosphere lid at a higher pressure, reducing the melt production. At the same time when the thickness of the stagnant-lid increases, the mean mantle temperature increases creating more melt. Internal heat generation has a secondary affect that also impacts both the internal temperature (e.g., Kiefer, 2003) and thickness of the lid.

This led us to consider the decay of radiogenic heat sources through time and the cooling core boundary condition to explain large amount of melt early to create Tharsis and the sharp decrease in melt production after Tharsis formation. The model with 100% of the radiogenic elements in the crust does not produce enough melt to create a structure like Tharsis. For a model with 40% radioactive elements in the mantle, the lid is pretty thick (Fig. 8) and even if it produces a decent amount of melt, it is uncertain how melt would make it to the surface. With all the radiogenic elements in the mantle, the model produces more melt than would be required to create Tharsis. However, none of the models generate any melt between 2 Gyr and present. Using the Wanke and Dreibus (1994) concentrations of radiogenic elements with 100% of these in the mantle produces a melt curve similar to the Lodders and Fegley (1997) curve with 60% of the radiogenic elements in the crust. Thus, while a model with the Wanke and Dreibus heating rate decreases the initial pulse of magma at about 4 Gyr, it does not produce any melt after 3.3 Gyr.

The planform of convection was also compared with the distribution of volcanism on Mars. None of the constant heat source models produce a prominent low-degree structure early on but the model with higher internal heating definitely produces a comparatively low-degree structure. However, both the models decay to a multiple-plume structure. For the decaying heat sources with a viscosity increase by a factor of 8 in the lower mantle, the structure varies from a low-degree to multiple plumes structure early on and melt production varies from isolated plumes heads to a global layer; as we increase the percentage of radiogenic elements in the mantle. All the low-viscosity decaying models evolve to a multiple plume structure at present day. For the viscosity increase by a factor of 25, we observe a multiple plume structure with a dominant degree-two structure; with isolated melt on plume heads, developing around 4 Ga that evolves to a multiple plume structure with ridge features.

Lowering the super-adiabatic temperature difference across the mantle by 25 degrees reduces the melt production by an order of magnitude and a reduction of 100 degrees shuts off melt production almost completely. While this could provide a bound on the mantle temperature and the corresponding melt production through time, uncertainties in the melting relationship need to be considered. In addition, we use a delta T value of 1600 K (Kiefer, 2003) for our melt production calculations in contrast to a higher value of 1980 K as used in some studies (i.e., Roberts and Zhong, 2006). Even this low value produces an enormous amount of melt during the early stages of the calculation. Similarly, lowering the mantle temperature or including more thermodynamically consistent melt calculations in our models (e.g. Sramek and Zhong, 2012; Ruedas et al., 2013a, 2013b) will reduce the melt production early on to a more reasonable scale but would not solve the lack of present day melt.

We did not find a strong tendency toward degree-1 planforms as in Roberts and Zhong (2006). The main difference between our calculations (Fig. 2b and 2d) and theirs is that we begin from a hot mantle and allowed our calculations to cool through time, while they used an initial condition based on a quasi-steady axisymmetric calculation. When we lower the initial mantle temperature from 0.95 to a value of 0.75, closer to the steady-state value, we observe a degree-two structure with a ridge for the constant heat source model. This cooler starting mantle temperature reduces the amount of excess heat in the mantle. The resulting planform is similar to Roberts and Zhong's (2006) model V2. This leads us to speculate that the initial temperature is the main cause of the difference. With an initially hot mantle, the mantle must cool and in stagnant-lid convection, plumes are the primary means of transferring heat from the deep interior. It is also possible that the depth-dependent coefficient of thermal expansion and diffusivity used by Roberts and Zhong (2006) could cause the variation. In the case of decaying models, for example SK4, lowering the mantle temperature to 0.75 produces a strong low-degree structure and also lowers the production of melt to a value more consistent with the melt needed to produce Tharsis.

5. Conclusion

We modeled 3D spherical convection with both constant and varying heat sources with a hot isothermal interior and with the inclusion of latent heat and ran for 4.3 Gyr. A constant and low value of internal heating, PS1, consistent with our best estimate of present day radioactive isotope abundances produces abundant melt distributed in a global layer due to the presence of many smaller plumes. A constant and high value of internal heating, PS2, consistent with our best estimate of radioactive isotope abundances at 4.2 Ga produce more than enough melt to create Tharsis, but also continues to produce a similar amount of melt throughout the calculation, localized to plume heads, even to the present day.

We implement a cooling core boundary condition with the decaying radiogenic heat sources. We partition the heat producing elements between the crust and the mantle and our models with higher concentrations of heat producing elements in the mantle produce abundant melt. Early on, melt is concentrated on plume heads to a global layer as we increase radioactive elements in the mantle. In all the decaying cases, melt production ceases midway through the evolution and we are unable to generate present day melt. Yet the concentrations of heat producing elements in these models are higher than predicted based on SNC meteorite studies. We are able to produce a near degree-2 structure with the high internal constant heat sources and with the decaying heat source where all the radioactive elements are partitioned into the crust.

There are many uncertain parameters in the problem, including the initial temperature of the mantle, the partitioning of heat producing elements between the mantle and crust, the melting curve of the Martian mantle, and the temperature of the core–mantle boundary through time. Because the melt production curves change significantly with small changes in these parameters, we do not believe it is profitable to 'tune' the models to achieve specific curves. Yet, based on this work we have some general observations. First, the timing delay between the formation of the dichotomy and the formation of Tharsis can be controlled by the Rayleigh number and a smaller value than what was estimated based on typical mantle parameters seems necessary to delay the onset of melting from the start of the calculation. Magma ocean solidification and overturn (Elkins-Tanton et al., 2003, 2005) due to a stable stratified mantle could delay the formation of instabilities at the core–mantle boundary and hence the arrival of a mantle plume at the surface and allow time for a cold, stiff boundary layer to form. This is beyond the scope of our investigation. Alternatively, reducing the thermal conductivity of the crust or relying on small-scale convection may be necessary to explain late-stage volcanism. Using Wanke and Dreibus (1994) concentrations lowers the melt production early but does not resolve the absence of melt late. Finally, not every plume head in our calculations generate melt. The large-scale volcanic features may not coincide with the pattern of mantle convection. While our results are intriguing, there is much more to be done to fully understand the relationship between Martian volcanism and internal dynamics of the mantle, including a better understanding of the thermal structure of plumes in a multi-plume planform and using a more thermodynamically consistent melt calculation.

Acknowledgements

We acknowledge support from NASA, Mars Data Analysis Program, grant NNX08AD07G. We thank James Roberts and three anonymous reviewers for their constructive reviews. The sponsor had no role in the design study, collection or analysis of the work.

References

Agee, C.A., Draper, D.S., 2004. Experimental constraints on the origin of Martian meteorites and the composition of the Martian mantle. Earth Planet. Sci. Lett. 224, 415–429.
Anderson, R.C., Dohn, J.M., Golombek, M.P., Haldemann, A.F.C., Franklin, B.J., Tanaka, K.L., Lias, J., Peer, B., 2001. Primary centers and secondary concentrations of tectonic activity through time in the western hemisphere of Mars. J. Geophys. Res. 106 (E9), 20563–20585.
Berman, D.C., Hartmann, W.K., 2002. Recent fluvial, volcanic, and tectonic activity on the Cerberus Plains of Mars. Icarus 159, 1–17.
Bertka, C.M., Holloway, J.R., 1994. Anhydrous partial melting of an iron-rich mantle I: Subsolidus phase assemblages and partial melting phase relationships at 10 to 30 kbar. Contrib. Mineral. Petrol. 115, 313–322.
Breuer, D., Spohn, T., 2006. Viscosity of the Martian mantle and its initial temperature: Constraints from crust formation history and the evolution of the magnetic field. Planet. Space Sci. 54, 153–169.
Carr, M.H., 1981. The Surface of Mars. Yale Univ. Press, New Haven, CT.
Carr, M.H., Head III, J.W., 2010. Geologic history of Mars. Earth Planet. Sci. Lett. 294, 185–203.
Elkins-Tanton, L.T., Parmentier, E.M., Hess, P.C., 2003. Magma ocean fractional crystallization and cumulate overturn in terrestrial planets: Implications for Mars. Meteorit. Planet. Sci. 38 (12), 1753–1771.
Elkins-Tanton, L.T., Hess, P.C., Parmentier, E.M., 2005. Possible formation of ancient crust on Mars through magma ocean processes. J. Geophys. Res. 110.
Frey, H.V., Roark, J.H., Shockey, K.M., Frey, E.L., Sakimoto, S.E.H., 2002. Ancient lowlands on Mars. Geophys. Res. Lett. 29 (10), 1384.
Grasset, O., Parmentier, E.M., 1998. Thermal convection in a volumetrically heated, infinite Prandtl number fluid with strongly temperature-dependent viscosity: Implications for planetary evolution. J. Geophys. Res. 103, 18171–18181.
Greeley, R. Guest, J.E., 1987. Geological map of the eastern equatorial region of Mars. U.S. Geol. Surv., Misc. Invest. Series, Map 1-1802-B.
Grott, M., Breuer, D., 2009. Implications of large elastic thickness for the composition and current thermal state of Mars. Icarus 201, 540–548.
Grott, M., Breuer, D., 2010. On the spatial variability of the Martian elastic lithosphere thickness: Evidence for mantle plumes?. J. Geophys. Res. 115.
Hager, B.H., Richards, M.A., 1989. Long-wavelength variations in Earth's geoid: Physical models and dynamical implications. Philos. Trans. R. Soc. Lond. A 328, 309–327.
Harder, H., Christensen, U.R., 1996. A one plume model of Martian mantle convection. Nature 380.
Hartmann, W.K., 2005. Martian cratering 8: Isochron refinement and the chronology of Mars. Icarus 174, 294–320.
Hartmann, W.K., Berman, D.C., 2000. Elysium Planitia lava flows: crater count chronology and geological implications. J. Geophys. Res. 105, 15011–15026.
Hartmann, W.K., Malin, M., McEwen, A., Carr, M., Soderblom, L., Thomas, P., Danielson, E., James, Philip, Veverka, J., 1999. Evidence for recent volcanism on Mars from crater counts. Nature 397, 586–589.
Hartmann, W.K., Neukum, G., Werner, S., 2008. Confirmation and utilization of the "production function" size frequency distributions of Martian impact craters. Geophys. Res. Lett. 35.
Hauber, E., Broz, P., Jagert, F., Jodlowski, P., Platz, T., 2011. Very recent and widespread basaltic volcanism on Mars. Geophys. Res. Lett. 38.
Hauck II, S.A., Phillips, R.J., 2002. Thermal and crustal evolution of Mars. J. Geophys. Res. 107. E7.
Head, J.W., Greeley, R., Golombel, M.P., Hartmann, W.K., Hauber, E., Jaumann, R., Masson, P., Neukum, G., Nyquist, L.E., Carr, M.H., 2001. Geological processes and evolution. Space Sci. Rev. 96, 263–292.
Kiefer, W.S., 2003. Melting in the martian mantle: Shergottite formation and implications for present-day mantle convection on Mars. Meteorit. Planet. Sci. 39 (12), 1815–1832.
Kiefer, W.S., Li, Q., 2009. Mantle convection controls the observed lateral variations in lithospheric thickness on present day Mars. Geophys. Res. Lett. 36.
Klein, E.M., Langmuir, C.H., 1987. Global correlations of ocean ridge basalt chemistry with axial depth and crustal thickness. J. Geophys. Res. 92, 8089–8115.
Lenardic, A., Nimmo, F., Moresi, L., 2004. Growth of the hemispheric dichotomy and the cessation of plate tectonics on Mars. J. Geophys. Res. 109.
Li, Q., Kiefer, W.S., 2007. Mantle convection and magma production on present-day Mars: Effects of temperature-dependent rheology. Geophys. Res. Lett. 34.
Lodders, K., Fegley, B., 1997. An oxygen isotope model for the composition of Mars. Icarus 126, 373–394.
McEwen, A.S., Malin, M.C., Carr, M.H., Hartmann, W.K., 1999. Voluminous volcanism on early Mars revealed in Valles Marineris. Nature 397, 584–586.
McLennan, S.M., 2001. Crustal heat production and the thermal evolution of Mars. Geophys. Res. Lett. 28 (21), 4019–4022.
Montesi, L.G.J., Zuber, M.T., 2003. Clues to the lithospheric structure of Mars from wrinkle ridge sets and localization instability. J. Geophys. Res. 108 (E6), 1–22.
Mutch, T.A., Arvidson, R.A., Binder, A.B., Guinness, E.A., Morris, E.C., 1976. The Geology of Mars. Princeton Univ. Press, Princeton, NJ.

Neukum, G., Jaumann, R., Hoffmann, H., Hauber, E., Head, J.W., Basilevsky, A.T., Ivanov, B.A., Gasselt, S.V., Murray, J.B., McCord, T., The HRSC Co-Investigator Team, 2004. Recent and episodic volcanic and glacial activity on Mars revealed by the High Resolution Stereo Camera. Nature 432, 971–979.

Neumann, G.A., Zuber, M.T., Wieczorek, M.A., McGovern, P.J., Lemoine, F.G., Smith, D.E., 2004. Crustal structure of Mars from gravity and topography. J. Geophys. Res. 109.

Nimmo, F., Stevenson, J.D., 2000. Influence of early plate tectonics on the thermal evolution and magnetic field of Mars. J. Geophys. Res. 105 (E5), 11969–11979.

Olson, P., Schubert, G., Anderson, C., 1987. Plume formation in the D″-layer and the roughness of the core–mantle boundary. Nature 327, 409–413.

O'Neill, C., Lenardic, A., Jellinek, A.M., Kiefer, W.S., 2007. Melt propagation and volcanism in mantle convection simulations, with applications for martian volcanic and atmospheric evolution. J. Geophys. Res. 112 (E7).

Phillips, R.J., Zuber, M.T., Solomon, S.C., Golombek, M.P., Williams, M.E., Banerdt, W.B., Smith, D.E., Williams, M.E., Hynek, B.M., Aharonson, O., Hauck II, S.A., 2001. Ancient geodynamics and global-scale hydrology on Mars. Science 291 (5513), 2587–2591.

Plescia, J.B., 1990. Recent flood lavas in the Elysium region for Mars. Icarus 88, 465–490.

Redmond, H.L., King, S.D., 2004. A numerical study of a mantle plume beneath the Tharsis Rise: Reconciling dynamic uplift and lithospheric support models. J. Geophys. Res. 109, E09008. http://dx.doi.org/10.1029/2003JE002228.

Reese, C.C., Solomatov, V.S., Moresi, L.N., 1998. Heat transport efficiency for stagnant lid convection with dislocation viscosity: Application to Venus and Mars. J. Geophys. Res. 103 (E6), 13643–13658.

Reese, C.C., Solomatov, V.S., Moresi L, N., 1999. Non-Newtonian stagnant lid convection and magmatic resurfacing on Venus. Icarus 139, 67–80.

Roberts, J.H., Zhong, S., 2004. Plume-induced topography and geoid anomalies and their implications for the Tharsis rise. J. Geophys. Res. 109, E03009. http://dx.doi.org/10.1029/2003JE002226.

Roberts, J.H., Zhong, S., 2006. Degree-1 convection in the Martian mantle and the origin of the hemispheric dichotomy. J. Geophys. Res. 111.

Ruedas, T., Tackley, P.J., Solomon, S.C., 2013a. Thermal and compositional evolution of the martian mantle: Effects of water. Phys. Earth Planet. Inter. 220, 50–72. http://dx.doi.org/10.1016/j.pepi.2013.04.006.

Ruedas, T., Tackley, P.J., Solomon, S.C., 2013b. Thermal and compositional evolution of the martian mantle: Effects of phase transitions and melting. Phys. Earth Planet. Inter. 216, 32–58. http://dx.doi.org/10.1016/j.pepi.2012.12.002.

Schubert, G., Turcotte, D.L., Olson, P., 2001. Mantle Convection in the Earth and Planets. Cambridge Univ. Press, New York. 940 pp.

Schumacher, S., Breuer, D., 2007. An alternative mechanism for recent volcanism on Mars. Geophys. Res. Lett. 34.

Scott, D.H. Tanaka, K.L., 1986. Geologic map of the western equatorial region of Mars. U.S. Geol. Surv. Misc. Invest. Series, Map I-1802-A.

Smith, D.E., Zuber, M.T., Solomon, S.C., Phillips, R.J., Head, J.W., Garvin, J.B., Banerdt, W.B., Muhleman, D.O., Pettengill, G.H., Neumann, G.A., Lemoine, F.G., Abshire, J.B., Aharonson, O., Brown, C.D., Hauck, S.A., Ivanov, A.B., McGovern, P.J., Zwally, H.J., Duxbury, T.C., 1999. The global topography of Mars and implications for surface evolution. Science 284 (5419), 1495–1503.

Solomatov, V.S., 1995. Scaling of temperature- and pressure-dependent viscosity convection. Phys. Fluids 7, 266–274.

Solomatov, V.S., Moresi, L.N., 1996. Stagnant lid convection on Venus. J. Geophys. Res. 101 (E2), 4737–4753.

Solomatov, V.S., Moresi, L.N., 2000. Scaling of time-dependent stagnant lid convection: Application to small-scale convection on Earth and other terrestrial planets. J. Geophys. Res. 105, 21795–21817.

Solomon, S.C., Head, J.W., 1982. Evolution of the Tharsis province of Mars: the importance of heterogeneous lithospheric thickness and volcanic construction. J. Geophys. Res. 82, 9755–9774.

Solomon, S.C., Aharonson, O., Aurnou, J.M., Banerdt, W.B., Carr, M.H., Dombard, A.J., Frey, H.V., Golombek, M.P., Hauck II, S.A., Head III, J.W., Jakosky, B.M., Johnson, C.L., McGovern, P.J., Neumann, G.A., Phillips, R.J., Smith, D.E., Zuber, M.T., 2005. New perspectives on Ancient Mars. Science 307 (5713), 1214–1220.

Sramek, O., Zhong, S., 2010. Long-wavelength stagnant lid convection with hemispheric variation in lithospheric thickness: Link between Martian crustal dichotomy and Tharsis?. J. Geophys. Res. 115.

Sramek, O., Zhong, S., 2012. Martian crustal dichotomy and Tharsis formation by partial melting coupled to early plume migration. J. Geophys. Res. 117.

Takahashi, E., Shimazaki, T., Tsuzaki, Y., Yoshida, H., 1993. Melting study of a peridotite KLB-1 to 6.5 GPa, and the origin of basaltic magmas. Philos. Trans. R. Soc. Lond. A 342 (1663), 105–120.

Tan, E., Choi, E., Thoutireddy, P., Gurnis, M., Aivazis, M., 2006. GeoFramework: Coupling multiple models of mantle convection within a computational framework. Geochem. Geophys. Geosyst. 7 (6).

Tanaka, K.L., 1986. The stratigraphy of Mars. In: Proc. Lunar Planet. Sci. Conf. 17. J. Geophys. Res. Suppl. 91 (B13), E139–E158.

Tanaka, K.L. Scott, D.H., 1987. Geological map of the polar regions of Mars. U.S. Geol. Sum., Misc. Invest. Series, Map 1-1802-C.

Tanaka, K.L., Scott, D.H., Greeley, R., 1992. Global stratigraphy. In: Kieffer, H.H., et al. (Eds.), Mars. Univ. of Ariz. Press, Tucson, pp. 345–382. Chap. 11.

Turcotte, D.L., Schubert, G., 2002. Geodynamics, 2nd ed. Cambridge Univ. Press, Cambridge. 456 pp.

Wanke, H., Dreibus, G., 1994. Chemistry and accretion history of Mars. Philos. Trans., Phys. Sci. Eng. 349 (1690), 285–293.

Wenzel, M.J., Manga, M., Jellinek, M., 2004. Tharsis as a consequence of Mars' dichotomy and layered mantle. Geophys. Res. Lett. 31.

Werner, S.C., 2008. The early martian evolution—Constraints from basin formation ages. Icarus 195 (1), 45–60.

Werner, S.C., 2009. The global martian volcanic evolutionary history. Icarus 201, 44–68.

Zhong, S., 2009. Migration of Tharsis volcanism on Mars caused by differential rotation of the lithosphere. Nat. Geosci. 2 (1), 19–23.

Zhong, S., Zuber, M.T., 2001. Degree-1 mantle convection and the crustal dichotomy on Mars. Earth Planet. Sci. Lett. 189 (1–2), 75–84.

Zhong, S., Zuber, M.T., Moresi, L., Gurnis, M., 2000. Role of temperature-dependent viscosity and surface plates in spherical shell models of mantle convection. J. Geophys. Res. 105 (B5), 11063–11082.

Zhong, S., McNamara, A., Tan, E., Moresi, L., Gurnis, M., 2008. A benchmark study on mantle convection in a 3-D spherical shell using CitcomS. Geochem. Geophys. Geosyst. 9.

Zuber, M.T., 2001. The crust and mantle of Mars. Nature 412, 220–227.

Zuber, M.T., Solomon, S.C., Phillips, R.J., Smith, D.E., Tyler, G.L., Aharonson, O., Balmino, G., Banerdt, W.B., Head, J.W., Johnson, C.L., Lemoine, F.G., McGovern, P.J., Neumann, G.A., Rowlands, D.D., Zhong, S., 2000. Internal structure and early thermal evolution of Mars from Mars global Surveyor topography and gravity. Science 287 (1788).

Chapter 3

Analysis of Martian Geoid and Topography based on Temperature Dependent Layered Viscosity Mantle Convection Models

Abstract

The internal structure of a planet has profound implications on its tectonic history and thermal evolution. The Mars Global Surveyor (MGS) and Mars Orbiter Laser Altimeter (MOLA) topography and gravity data sets are powerful tools that hold information on the internal structure of Mars. These data sets have been used to estimate the thickness of the Martian crust; however, gravity inversions are non-unique and, it is quite probable that in the current generation of crustal thickness models, mantle density structure is being mapped into crustal thickness at the longest wavelengths. We analyze a large number of 3D spherical convection models in an effort to characterize the mantle contribution to the geoid and topography under a variety of model assumptions. We find, consistent with previous work (*Kiefer et al*., 1996), that for spherical harmonics less than degree 10, there is a significant contribution to the geoid of Mars from mantle density structure. We compare the power spectra from our models with Kaula's rule (*Kaula,* 1967) and find that the geoid and topography spectra from our calculations decreases faster than Kaula's rule. This is consistent with the assumption that the geoid at short wavelengths is dominated by crustal structure and not mantle structure. However the geoid spectra from our convection models at long wavelengths varies from being nearly flat to following Kaula's trend.

3.1 Introduction

Our understanding of the dynamics of the Martian mantle is limited by a paucity of observations. The classic view of the Marian interior is that the mantle was, and possibly still is, dominated by one or more long-lived, stationary mantle plumes (e.g., *Carr*, 1973). The absence of an internally generated magnetic field on Mars implies that heat flow from the core into the mantle is low (*Nimmo and Stevenson*, 2000). This low value of the core heat flow has been used in thermal evolution calculations that conclude that Mars has cooled to a point that is not convecting (*Hauck and Phillips*, 2002). Although, *Redmond and King* (2004) show that this low heat flow does not rule out a thermal boundary layer at the base of the mantle and a plume. The view of a present-day conductive mantle is inconsistent with fully 3D spherical convection calculations that include decaying radiogenic heat sources, decreasing core-mantle boundary temperature with time, and latent heat of melting *(Ruedas et al.*, 2013a; *Ruedas et al.,* 2013b; *Sekhar and King,* 2014).

Prior to Mars Global Surveyor (MGS), a number of studies used gravity and topography to study the Martian lithosphere and concluded that long-wavelength topography on Mars is primarily supported by membrane stresses in the lithosphere and not mantle structure (*Turcotte et al.,* 1981; *Sleep and Phillips*, 1985; *Anderson and Grimm*, 1998). Gravity, topography and tectonic observations have been used to infer surface compensation and loading for the Tharsis region (e.g., *Sleep and Phillips*, 1985) and Valles Marineris (e.g., *Anderson and Grimm*, 1998). *Zhon*g (2002) used a viscoelastic loading model to show that only a small fraction of the Tharsis geoid anomaly (<10%) could be due to mantle structure and that the majority of the Tharsis geoid anomaly is the result crust and surface loading. *Redmond and King* (2004) found a slightly larger contribution to the Tharsis geoid anomaly from a mantle plume (<20%). The primary difference between the results of *Redmond and King* (2004) and *Zhong* (2002) is the assumed elastic thickness. *Zhong* (2002) assumes a 150 km elastic thickness, based on the gravity and topography studies, whereas *Redmond and King* (2004) assume a smaller value. *Zhong* (2002) further shows that the thin elastic shell formulation (e.g., *Turcotte et al.,* 1981) and the viscous flow models (e.g., *Richards and*

Hager, 1984; *Harder*, 2000) are both special cases of the viscoelastic loading formulation. Under certain conditions, combining viscous flow models and the thin elastic shell formulation can simulate the viscoelastic response. While *Redmond and King* (2004) do not use a viscoelastic formulation, they do combine the viscous flow calculations and the thin elastic shell formulation.

While the previous work described above has shown that the mantle contribution to the global gravity field and topography may be smaller than the crustal contribution, at long wavelengths 10-20% of the total gravity and topography is significantly greater than the level of uncertainty in these observations. In contrast, *Kiefer et al.* (1996) inverted the long-wavelength (harmonic degrees < 10) gravity and topography of Mars for crustal structure and lateral variations in mantle density, which they assume to be generated by thermal structure. They show that mantle structure dominates the topography at longest wavelengths and is a significant contributor to the long-wavelength gravitational potential.

The global topography data from Mars Orbiter Laser Altimeter (MOLA) (*Smith et al.,* 2001) and gravity data from Doppler tracking residuals (*Smith et al.,* 1999) from the MGS spacecraft provide information on the internal structure of Mars. *Zuber et al.* (2000), the first study using MGS gravity and topography, calculated a global Bouguer gravity field and interpret this in terms of a crustal thickness model with an average crustal density of 2900 kg/m^3 and average thickness of 50 km. In this model, the crust was up to 90 km thick under the southern hemisphere and significantly thinner under the northern hemisphere. *Neumann et al.* (2004) expand on the previous crustal thickness models of *Zuber et al.* (2000) by including a lower density for the Tharsis region based on regional admittance modeling and a low density for the polar ice caps. Both *Zuber et al.* (2000) and *Neumann et al.* (2004) used the crustal thickness formulation developed by *Wieczorek and Phillips* (1998). In the *Wieczorek and Phillips* (1998) formulation, Bouguer gravity is calculated from the observed topography and removed from the global gravity field, then topography on the crust-mantle interface is constructed to match the residual (i.e. observed minus Bouguer) gravity field. Therefore, by construction the crustal thickness model assumes that there is no contribution to the gravity field from the

mantle. This is only possible if there are no thermal anomalies in the mantle (e.g., *Hager,* 1984).

On Earth, gravity modeling uses constraints from other geophysical imaging techniques, such as seismic reflection/refraction. Without additional observations or theory to constrain the crustal structure, mantle density anomalies have been mapped into the current generation of crustal thickness models for Mars. In order to assess the robustness of these Martian crustal thickness models (e.g., *Neumann et al.,* 2004) we calculate the magnitude and structure of probable mantle density structure using mantle convection modeling. We use the gravitational potential, or geoid, following the example of terrestrial modeling (*Hager,* 1984; *Richards and Hager*, 1984). The contribution to the surface gravitational potential from a mass anomaly at a depth r falls off as 1/r and is more sensitive to deep structure than the free-air gravity, which falls off as $1/r^2$ (c.f., *Hager and Clayton,* 1989). We evaluate the mantle contributions of the gravitational potential and dynamic topography using the spherical harmonic representations of the gravitational potential and dynamic topography fields from our calculations and we specifically focus on power spectra of the geoid and topography.

3.2 Mantle Convection Model

We compare a number of 3D spherical convection calculations in a Mars geometry spherical shell that are computed using the finite element code CitcomS (*Zhong et al.,* 2000; 2008; *Tan et al.,* 2006). CitcomS solves the equations of conservation of mass, momentum and energy for a creeping, incompressible fluid. Using a Boussinesq approximation, these equations are given by:

$$\nabla . \vec{u} = 0 \tag{1}$$

$$-\vec{\nabla} P + RaT\vec{e}_r + \vec{\nabla} \cdot \left(\eta \left(\nabla \vec{u} + \nabla \vec{u}^T\right)\right) = 0 \tag{2}$$

$$\frac{\partial T}{\partial t} + \vec{u} . \vec{\nabla} T = \nabla^2 T + H \tag{3}$$

where *u, P, T,* and η are the velocity vector, dynamic pressure, temperature and viscosity respectively. *Ra* is the Rayleigh number and *H* is the non-dimensional internal heating rate.

We consider a Newtonian rheology with a strong temperature-dependent viscosity (e.g., *Karato and Wu*, 1993) and a layered viscosity structure that includes a viscosity increase by a factor of 8 and 25 at a depth of 996 km (*Roberts and Zhong*, 2006). The calculations are performed with a free-slip cold upper boundary and a stress-free core mantle boundary. Following the work of *Sekhar and King* (2014), we consider both constant and decaying heat sources. We have implemented a cooling core boundary condition that is consistent with the thermal evolution models presented by *Hauck and Philips* (2002) for the decaying heat source models and we have included latent heat of melting on the temperature. The details of these methods are given in *Sekhar and King* (2014). We vary the Rayleigh number from 10^6–10^8. We begin from a uniform mantle temperature with a 50-My old thermal boundary layer and a 1% temperature perturbation with a spherical harmonic l=50, m=42 pattern. The calculations run for more than 4 Gyr of model evolution on a 768 by 768 by 64-element grid require 3-4 days of computational time on our 96-processor cluster.

3.2.1 Data Sets

We have generated two reference maps, a geoid/areoid map (Figure 3.1) using the gravitational potential model JGM95 (*Neumann et al.,* 2004; *Konopliv et al.,* 2006; *Wieczorek*, 2007) which was derived from MGS data and a topographic map (Figure 3.2) (*Wieczorek*, 2007). In this work, we use the spherical harmonic degree 95 model, jgm95j01.sha, which was obtained from the website: http://ppi.pds.nasa.gov/data/MGS-M-RSS-5-SDP-V1.0/DATA/RS_SHA/. The topography model used in this work is MarsTopo2500.shape accessed from the planetary topography website: http://www.ipgp.fr/~wieczor/SH/SH.html. The topography model of Mars is based on MOLA data with a maximum spherical harmonic degree of 2500. We restrict our focus to spherical harmonic degrees less than 100.

The topography of Mars is divided into a northern lowland region and southern highland region. Near the boundary of this region is Tharsis rise, a volcanic construction that includes the shield volcanoes Olympus Mons, Arsia Mons, Pavonis Mons, Ascraeus Mons and Alba Patera (*Smith et al.,* 2001), and encompasses nearly a quarter of the surface area of the planet. The geoid has two prominent highs, the larger high correlates with Tharsis rise and the smaller high is almost 180 degrees from Tharsis.

The gravitational potential is given by (*Kiefer et al.,* 1996),

$$U(\theta,\phi,r) = \frac{GM}{r}\left[l + \sum_{l=2}^{50}\sum_{m=0}^{l}\left[\frac{R}{r}\right]^{l} P_{lm}(cos\theta)(C_{lm}cosm\phi + S_{lm}sinm\phi)\right] \quad (4)$$

where $P_{lm}(cos\theta)$ are the normalized associated Legendre polynomials of degree l and order m, θ is the colatitude, ϕ is the longitude and r is the radius at which the field is evaluated. C_{lm} and S_{lm} are the harmonic co-efficients, $GM = 4.282\text{x}10^4$ km^3 s^{-2} and R = 3398 km (*Smith et al.,* 1993, *Kiefer et al.,* 1996). The geoid, N, from this gravitational field is calculated by,

$$N = \frac{U(\theta,\phi,r)}{g} \quad (5)$$

where g is the gravitational acceleration of the planet (Table 3.1).

3.2.2 Power Spectrum

Because the calculations we are using are time-dependent, thermal anomalies within the interior of the planet are not stationary. We assume that energy from the short-wavelength instabilities in the flow field, while moving around the sphere, remains in the short-wavelength components of the flow once we approach a quasi-steady state. Similarly, we assume that energy in the long-wavelength component of the flow remains at the long wavelengths. Thus looking at the power spectrum of the gravitational or topographic fields should be invariant even though the flow may still be time varying.

The spectral power of a field per degree l (e.g., *Dahlen and Tromp*, 1998, B.8; *Becker and Boschi*, 2002), can be defined by

$$\sigma_l^2 = \frac{1}{2l+1}\sum_{m=0}^{l}\left(C_{lm}^2 + S_{lm}^2\right) \tag{6}$$

where l, m, C_{lm} and S_{lm} are the same as Equation 4. *Melosh* (2011) notes that the power spectra of Earth, Venus, and Mars all follow Kaula's rule and only the Moon deviates from this trend. The relation between wavelength and spherical harmonic degree, following *Melosh* (2011) work, is given as:

$$\lambda = \frac{2\pi a}{\sqrt{l(l+1))}} \tag{7}$$

where a is the planetary radius. The wavelength that corresponds to *l*=1 is $1.5\text{x}10^4$ km, for *l* = 2 is $8.5\text{x}10^3$ km and for *l*=20, wavelength is $1.0\text{x}10^3$ km.

*Kaula (*1963a) inferred the following relationship for normalized coefficients of Earth's gravitational potential as a function of degree,

$$\sigma_l \approx \sqrt{(2l+1).\frac{10^{-10}}{l^4}} \tag{8}$$

This is sometimes referred to as "Kaula's rule" or "Kaula's law" and is known to hold for the topographic and gravity fields of Earth, Venus and Mars (*Melosh*, 2011).

Following *Kiefer et al.* (1996), we plot the power spectrum of the gravitational potential as a function spherical harmonic degree (Figure 3.3). While *Kiefer et al*.'s work was based on gravity model GMM1 (*Smith et al.,* 1993) that used Mariner 9 and Viking 1 and 2 data with significantly greater uncertainty than JGM95 (*Wieczorek*, 2007), the power spectrum in Figure 3.3 is nearly identical to *Kiefer et al*. (1996) (see their Figure 1) for degrees up to and including 50. Following *Kiefer et al.* (1996) we calculate the admittance, F_l, given by

$$U_{lm} = F_l H_{lm} + I_{lm} \tag{9}$$

where U_{lm} are the gravitational potential coefficients for degree *l* and order *m*, H_{lm} are the coefficients of the spherical harmonic expansion of topography for degree *l* and order *m*, and I_{lm} are the coefficients of the component of the gravitational potential that is uncorrelated with the topography. The admittance can be calculated by a standard least-squares approach as outlined by *Bills et al.* (1987). Using the JGM95 gravity coefficients and the MarsTopo2500.shape topography model we plot the admittance in Figure 3.4. The admittance curve agrees quite well with the curve from *Kiefer et al*. (1996). Figures 3.3 and 3.4 demonstrate that the wavelengths of interest for global modeling from modern models for gravitational potential (JGM95) and topography (Shape2050.sha) are little changed from the pre-MGS models GMM1 (*Smith et al.,* 1993) and *Bills and Nerum's* (1995) topography model.

Figure 3.5 shows the power spectra of the jgm95j01 geoid and MarsTopo2500 topography model along with the Kaula's trend (Equation 8) for spherical harmonic degrees up to degree and order 100. The slope of the topography power spectrum is nearly identical to Kaula's trend, with the only significant deviations at degree 1 and 2. The power in the geoid is zero at degree 1 because of the adoption of a center of mass coordinate system for gravity models (c.f., *Wahr*, 1996). At degrees 2-4 the geoid coefficients deviate significantly from Kaula's trend, while degrees 5-38 lie on the Kaula trend. Beyond degree 38, there is a steep fall off in the geoid that may be due to damping of the higher harmonics in the gravity inversion. Both the geoid and topography have correlated kinks in the power spectra between degrees 20 and 38. The deviation of the geoid spectra from the Kaula trend at degrees 2-4 along with admittance results for degrees 2-3 which require compensation depth in the mid-mantle (*Kiefer et al.,* 1996) and the weaker correlation between the geoid and topography at those degrees (*Kiefer et al.,* 1996) all point to a significant mantle contribution at these wavelengths.

3.3 Results

We consider 12 calculations (Table 3.2) with a range of physical parameters in order to isolate the effect of these parameters on the resulting geoid and topography from our calculations. We analyze all the power spectrum plots for a maximum degree and

order of 40 through the evolution of the models. We also observe the geoid and topography correlation with one another for all our models. Because we have no reason to prefer one set of conditions to another, and because there is no issue of computational error that would differ from calculation to calculation, we vary parameters. We have two sets of models: those with a constant heat source and those with a heat source that decreases with time. For the constant heat source calculations, we vary the Rayleigh number ($10^6 – 10^8$), viscosity layer in the lower mantle (isoviscous, 8 times higher and 25 times higher than the viscosity of the upper mantle) and internal heat. In constant heat source, the internal heat parameter maintains the same internal heat through the evolution of the planet. We have high internal values of 49.66, following *Roberts and Zhong* (2006) and low internal heat values of 17.25 based on the *Wanke and Dreibus* (1994) heating rates and is consistent with present day radioactive element concentrations. In the case of decreasing heat sources with time, we vary the partitioning of radiogenic elements between the mantle and crust (*Kiefer,* 2003) and we consider the lower mantle viscosity to be 8 times and 25 times the upper mantle (*Roberts and Zhong*, 2006). We implement the *Lodders and Fegley* (1997) concentration of radioactive isotopes in the mantle. For further details see *Sekhar and King* (2014). SK1, SK2 and SK3 have a lower mantle with a viscosity increase 8 times that of the upper mantle, while SK4 has a lower mantle viscosity of 25 times the upper mantle viscosity, consistent with previous models from *Roberts and Zhong* (2006) which produce low-degree mantle structure consistent with one or few plumes. While all the radioactive elements are in the crust (100%) for SK1, SK2 and SK4 have 60% of the radioactive elements in the crust and SK3 has 100% of the radioactive elements in the mantle. In the models with radiogenic heat sources, the partitioning of radioactive elements between the crust and mantle controls the decaying heat.

3.3.1 Rayleigh Number

In Figure 3.6 we consider the effect of Rayleigh number on the power spectra with a temperature-dependent rheology and constant non-dimensional internal heat source of 49.66 based on *Roberts and Zhong* (2006) calculations, which would be applicable for early in the solar system evolution. The calculations have a 8-fold increase

in viscosity at a depth of 996 km, which produces low-degree structure (*Roberts and Zhong*, 2006). While the calculations evolve with time, the power spectra are taken from the final state, after 4 Gyr of model evolution, when the calculations are in a statistically steady state. We observe that the power spectrum of the highest Rayleigh number case (plus symbols, model PS3) follows the trend of Kaula's law except for degree 1. As noted above, because gravity models are constructed in a center of mass reference frame the degree 1 gravitational potential coefficients are identically zero. In our convection models, the geoid is calculated in a center of mass reference frame. We note that with decreasing Rayleigh number, the slope of the power spectra change. For harmonics greater than about degree 20, the slope becomes more strongly negative, while for the harmonics less than about degree 15, the slope becomes more flat. Because these are time-evolving models, we plot the power spectra for the Rayleigh number 10^8 case at various times during the calculation on Figure 3.7. The most significant variation in the spectra occurs at the lowest spherical harmonic degrees, consistent with the interpretation that these degrees have a significant contribution from the mantle.

As we observe the power spectrum through the evolution of the model, the highest Rayleigh number of 10^8 (PS3) has a very strong degree-1 contribution and the power decreases with increasing wavelength until degree 11. A Rayleigh number of $2x10^7$ (PS2) has a much stronger contribution at degrees 1, 2 and 4 with degree 1 being the strongest. The smallest Rayleigh number of $2x10^6$ (PS4) has a prominent degree 1, 2 and 4 pattern as well. Even though there is power in these degrees, the power spectrum is weaker in PS4 compared to PS2. A big difference can be observed for larger degrees (i.e., $l \geq 10$). While there is some contribution to the higher degrees in PS2 and PS4, it is completely absent in PS3 (Figure 3.8).

The general expectation is that geoid and topography should decrease with increasing Rayleigh number (e.g., *Blankenbach et al.,* 1989). In the maps of geoid and topography this appears to be violated. The geoid for the Rayleigh number 10^8 case (PS3) has the largest peak-to-peak values of -300 m to 300 m. This is a result of a very large degree -1 component. Once degree-1 is removed from the geoid contribution, the peak-to-peak geoid structure is much smaller of -25 m to 65 m. This is shown in Figure

3.9. The peak-to-peak topography is -900 m to 2600 m. There is a strong correlation between geoid and topography. A smaller Rayleigh number, $2x10^7$ (PS2), has a less prominent low-degree structure and a larger peak to peak variation of -100 m to 180 m in the geoid. There are two highs in the geoid that correlate spatially with two highs in the topography. There is a prominent geoid low that does not exactly correlate with the topography. The largest peak-to-peak geoid of -320 m and 280 m is the Rayleigh number $2x10^6$ case (PS4), which has a multiple plume structure. The geoid correlates with the topography (Figure 3.9).

We also examine two models with varying Rayleigh numbers, which have no viscosity increase between the upper and lower mantle (Figure 3.10). For a Rayleigh number of $2x10^6$ (PS2ab), it has a higher geoid flatness compared to the model with Rayleigh number $2x10^7$ (PS2a) between $l = 4$ and $l = 12$. The slope drops more steeply for $2x10^6$ (PS2ab) compared to $2x10^7$ (PS2a) for shorter wavelength, $l>18$ (Figure 3.10). Compared to PS2a, PS2ab has a higher degree-2 contribution and the smaller harmonics do not correlate with the Kaula's trend suggesting the same as above that they are probably due to mantle contributions.

While observing the power spectrum through time, it is seen that PS2ab has an equivalent prominent degree-1 structure compared to PS2a but a much stronger degree 2, as can be seen in Figure 3.11. In general there is a stronger geoid contribution in the power law for PS2ab. In the case of PS2a, there is a steady decay in power with increasing harmonics.

3.3.2 Internal Heat

We have three different non-dimensional internal heating rates in our calculations, 17.25 based on the composition of *Wanke and Dreibus* (1994), 49.66 based on *Roberts and Zhong* (2006) and an intermediate internal heat value of 33.5. All the models have a Rayleigh number of $2x10^6$ and a lower mantle viscosity that is 8 times higher than the upper mantle (*Roberts and Zhong*, 2006). None of the internal heating calculations follow the Kaula's trend (Figure 3.12). There are variations between internal heat models, 49.66 (PS4), 33.5 (PS5) and 17.25 (PS6) in the smaller degrees $l \leq 5$ but in all cases, the

lowest internal heating rate has the largest power and the highest internal heating rate has the lowest power. They all have a similar trend with a flat geoid power spectra for l<12. The difference between the power spectra narrows at l = 12 and l = 13, the contribution from the three calculations is exactly the same. Beyond l = 13, the contribution by lowest internal heating rate (PS6) falls more steeply than the others, while the intermediate case (PS5) and highest case (PS4) fall off less steeply. Therefore, for higher degrees, the contribution to geoid by a higher internal heat continues while the lowest internal heat calculation cools down drastically.

Considering the time evolution of the models, as seen in Figure 3.13, the most striking feature of the time evolution in all models is that the present day spectra have the greatest power in the lowest harmonics. For the highest internal heating value (PS4), degree 1 is more prominent than degree 2 and degree 4. However, degree 2 and degree 4 are more prominent than degree 1 for the intermediate case (PS5). In the case of the smallest internal heating value (PS6), there is contribution to l = 2, 4 and even to a higher degree such as l = 8. PS6 does not show contribution for higher degree structures (l ≥18). All these models have a lower mantle viscosity 8 times the viscosity of the upper mantle (Figure 3.13). For present day, PS4 has a prominent degree 1 structure and also decays steadily. PS5 has a prominent degree 2 and 4 structure and decays steadily as well, but at a much faster rate and. PS6 has a stronger contribution in degree 1, 2, 4 and even 8, before decaying steadily.

Looking at the geoid and topography maps (Figure 3.14), we see that the geoid and topography do not correlate very strongly for (PS4), but the models with the lower internal heat, PS5 and PS6, have a strong correlation between the geoid and topography. All the models have a geoid peak to peak of approximately -300 m to 300 m while the topography peak to peak varies from -40 m to 40 m.

3.3.3 Viscosity Layering

We vary the viscosity at the lower mantle by including a viscosity jump of 8 and 25 times higher than the upper mantle at 996 km (*Roberts and Zhong*, 2006) but maintain the same Rayleigh number of 2×10^7 and same internal heat of 49.66, based on *Roberts*

and Zhong (2006) calculation. We can divide the spectra into three regions, the lowest degrees, 1-4, an intermediate region, 4-12 and a short wavelength region, greater than spherical harmonic degree 12 (Figure 3.15). All the three viscosity structures have a very similar slope that is somewhat steeper than the Kaula trend, in the short wavelength region. In the intermediate region, the uniform viscosity with depth model (PS2a) is flat and smaller than the 8-fold and 25-fold increase in viscosity models (PS2 and PS2b respectively), which have a shallower slope than the short wavelength region. At the longest wavelengths, once again the uniform viscosity with depth model (PS2a) has the smallest values while for the 8-fold and 25-fold increase (PS2 and PS2b), the trends are not as clear as in the intermediate and short wavelength regions.

On the power spectrum through the time evolution as seen in the plots on Figure 3.16, there is a prominent degree-1 structure for the higher viscosity layering models (PS2 and PS2b) compared to the uniform viscosity with depth model (PS2a) consistent with the Roberts and Zhong (2006) observation that viscous layering increases the probability of degree-1 structure. The uniform viscosity with depth calculation (PS2a) has most of the power concentrated in the first four harmonics and this pattern is consistent through out the time period of the calculation. The 8-fold and 25-fold cases (PS2 and PS2b) have more power at degree 1 than the uniform case, but also have significant but decreasing power in the first 15 harmonics. Once again, this pattern is maintained through out the entire time period of the calculation. This is consistent with our assumption that power in the flow field is not moving from long to short wavelengths, or vice versa, with time.

Looking at the geoid and topography maps at the end of the calculation (Figure 3.17), for the uniform viscosity with depth model (PS2a), the topography has many short-wavelengths highs and lows with peak to peak amplitudes of -140 to 200 m, however, the geoid contains a prominent long-wavelength geoid high in the southern hemisphere that is comprised of many smaller highs. The peak-to-peak geoid is -60 to 80 meters. In the case of the 8-fold viscosity increase (PS2), the short-wavelength peaks of the geoid and topography correlate with one another. The topographic lows in the southern hemisphere do not correspond to lows in the geoid. The geoid peak to peak is from -110 m to 190 m

and the topography peak to peak is -170 m to 430 m. There is a degree-1 pattern in the geoid with the southern hemisphere significantly higher than the northern hemisphere. This hemispheric pattern is completely absent in the topography. For the 25-fold increase in viscosity (PS2b), the geoid has a strong degree-1 component with a prominent high in the western hemisphere and a prominent low in the eastern hemisphere that have peak-to-peak values of -230 m to 250 m. On the other hand, the topography contains multiple short-wavelength highs and lows with peak-to-peak amplitudes of -200 to 450 m and the topography does not bear any resemblance to the geoid degree-1 structure. The low in the geoid correspond to multiple highs in the topography.

3.3.4 Decaying Heat Source

In the case of decaying heat source models, we implement the radiogenic concentrations of *Lodders and Fegley* (1997) and partition the heat sources between the mantle and the crust. All the models have a Rayleigh number of $2x10^7$ and SK1, SK2 and SK3 have a lower mantle viscosity 8 times higher than the upper mantle while SK4 and an increase of 25 times higher than the upper mantle. At the end of the calculations, the rate of internal heating in these models is closer to our low-end member case 17.25 (PS6). In general, we see that for the lower internal heating cases we have more power in the intermediate wavelengths and less power in the short wavelengths. This is again true in these models. In these calculations we partition the radioactive material between the crust and the mantle. The case with 100% of the radiogenic elements in the crust (SK1) has the highest contribution in degrees 1 through 8 and very little power above degree 15 (Figure 3.18). This pattern of power in the low degrees develops in the first billion years of model evolution and remains relatively constant from then on. In the case of SK2, which has 60% of the radiogenic elements in the crust, there is a very strong degree-1 component that stands out compared to the other degrees with significant power in the first 5 degrees at the end of the calculation. Once again, there is significantly more power in the first 15 degrees and the higher degrees drop off rapidly. SK3, which has 100% of the radiogenic material in the mantle, shows a much weaker degree-1 structure compared to SK2 with a general trend of power increasing from the early part of the calculation up to the end. With 60% of radiogenic elements in the crust, as in SK2 but a 25-fold increase

in viscosity, for SK4 the degree -2 component is more prominent than degree-1 and differs from its lower viscosity counterpart, SK2, in this manner. Degrees 1, 3, 5 and 6 are still significant in SK4 (Figure 3.18) and there is once again a trend of increasing power as the time progresses.

Looking at the maps of geoid and topography at the end of the calculation, all four calculations have a common intermediate wavelength pattern similar to the low internal heating calculation PS6 (Figure 3.19). The geoid peak to peak varies from -800 m to 1200 m (SK1), -500 m to 600 m (SK2), -200 m to 250 m (SK3) and -500 m to 700 m for SK4. The topography peak to peak varies from -650 m to 1150 m (SK1), -450 m to 750 m (SK2), -250 m to 550 m (SK3) and -600 m to 800 m for SK4. In all four cases the geoid and topography are correlated; however in SK2 and SK3, there is evidence of a degree-1 geoid high in the southern hemisphere that is not reflected in the topography. SK4 also shows a degree-2 structure in the geoid and topography that is observed in the poles.

3.4 Discussion

There is significant interest in degree-1 structure for Mars, because of the dominance of the Tharsis region. A Rayleigh number of 10^8 has a very strong degree-1 contribution, which dominates the geoid. Another model that shows a strong degree-1 structure is the constant heat source model with a very high viscosity in the lower mantle. For the decaying heat source models, the higher viscosity model, SK4 also shows a degree – 1 contribution. We can see that degree-1 is often a huge contribution to the geoid structure.

We can generally divide the power spectra into three regions, the longest wavelengths (l=1,5), intermediate wavelengths (l=5,20) and short wavelengths (l>20). For all of our calculations, with the exception of the Rayleigh number 10^8, 8-fold viscosity increase, high internal heating case (PS3), the power spectra fall off more rapidly than the Kaula trend at the shortest wavelengths. With increasing Rayleigh number, the general trend is that the individual values in the power spectra are smaller, with the exception of degree 1. The impact of viscosity on the power spectra is most

apparent at the intermediate and long wavelengths. For the uniform viscosity models the intermediate part of the spectrum is flat and with increasing lower mantle viscosity the slope increases. The pattern at the lowest harmonics is not as clean, but the higher viscosity lower mantle spectra have large values than the uniform viscosity case. Internal heating impacts the magnitude of the spectra but has little impact on the shape. Our results are generally consistent with Kiefer et al. (1996) who found that there was a significant component of mantle structure in the longest wavelengths (l=1-10).

The dynamic topography from stagnant lid convection should be small and in our calculations the peak to peak dynamic topography is always less than plus or minus 1 km, and in most cases on the order of plus or minus 100 m. This compares with peak topography of 22 km and a maximum low of -8 km on Mars. Thus, most of the topography on Mars is not supported by present-day convection, consistent with the results of *Lowry and Zhong* (2003) and *Redmond and King* (2004) and others. The geoid has contributions from internal density sources and surface topography (*Richard and Hager*, 1984) and these two contributions are large and have opposite signs. Therefore, because the dynamic topography is small, the contribution to the geoid from internal density (i.e., mantle thermal anomalies) should be significant. This is presently not accounted for by crustal thickness models (e.g., *Zuber et al.,* 2000; *Neumann et al.*, 2004).

While the present day pattern of mantle convection on Mars depends on initial conditions, distribution of radiogenic elements, and processes through time that may never be known, we have some hope that the power in the convecting system might be less dependent on these effects. To that end, we focus on the power spectrum of geoid and topography from our calculations. In some calculations we find a trend of overall increasing power with time; however all our calculations develop relatively stable power spectra, with power concentrated in the low harmonics, even though our initial perturbation was l=50.

One of the more interesting aspects of power spectra of planetary topography and geoid is "Kaula's rule" which states that power decreases as $1/l^2$. This holds true for the Earth, Venus and Mars but not the Moon (*Melosh*, 2011) and there is at present no

theoretical explanation for this observation. Most of the power spectra from our calculations do not follow Kaula's rule, hence we deduce that there is some important aspect in planetary topography/geoid that is not accounted for in our convection models. Because most of Mars topography is not convectively supported, we suggest that Kaula's rule is a statement of the spectrum of planetary topography, although we have no explanation for why topography on these different planets should vary like $1/l^2$.

There are several trends that we infer from our model power spectra that push them toward Kaula's rule these include higher Rayleigh number and a large increase in viscosity with depth. Because we only have a single high Rayleigh number calculation, additional results are needed to verify this hypothesis.

3.5 Conclusion

We observe that the power spectrums are very intriguing and provide us with information on the evolution of the spherical harmonic degree structure with time. As mentioned earlier, we are using time-dependent calculations where thermal anomalies within the interior of the planet are not stationary. However, the energy from the short-wavelength instabilities in the flow field, remains in the short-wavelength components of the flow the energy in the long-wavelength component of the flow remains at the long wavelengths. Thus looking at the power spectrum of the geoid and topography fields remain consistent with each step.

Our calculations also show that the characteristics of convection models that match Kaula's trend are models with a high Rayleigh number of 10^8 and models with a viscosity jump at the lower mantle viscosity. These calculations are isolated cases and we need more high Rayleigh number calculations to clearly understand the correlation between Kaula's trend and these models.

Finally, Even though Kaula's rule follows the topography trend, it breaks down for the geoid at the longest wavelengths. This suggests that the longest wavelengths of the geoid may have a significant mantle contribution, consistent with *Kiefer et al*. (1996).

References

Anderson, S., and R. E. Grimm (1998). Rift processes at the Valles Marineris, Mars: Constraints from gravity on necking and rate-dependent strength evolution, *Journal of Geophysical Research*. Vol 103, 11,113 11,124.

Blankenbach, B. et al (1989). A benchmark comparison for mantle convection codes. *Geophys. J. Int*. Vol 98, 23-38.

Becker, T. W. and L. Boschi (2001). A comparison of tomographic and geodynamic mantle models, *Geochem. Geophys. Geosyst*., Vol 3, 10.129/2001GC000168.

Bills, B.G., and R.S. Nerem (1995) A harmonic analysis of Martian topography, *Journal of Geophysical Research*. Vol 100, 26,317-26,326.

Bills, B. G., W. S. Kiefer, and R. L. Jones (1987). Venus: A harmonic analysis *Journal of Geophysical Research*. Vol 92, 10,335-10,350.

Carr, M. H. (1973). Volcanism on Mars, *Journal of Geophysical Research*. Vol 78, 4049-4062.

Dahlen, F. A., and J. Tromp (1998). Theoretical Global Seismology, *Princeton Univ. Press, Princeton, N. J*.

Hager, B. H (1984). Subducted slabs and the geoid; constraints on mantle rheology and flow. *Journal of Geophysical Research*. Vol 89, 6003-60015.

Hager, B. H., and R. W, Clayton (1989). Constraints on the structure of mantle convection using seismic observations, flow models, and the geoid. In: Peltier, W R (ed.) *Mantle Convection*. 658-753.

Harder, H (2000). Mantle convection and the dynamic geoid of Mars, *Geophys. Res. Lett*., Vol 27, 301-304.

Hauck, S. A. II, and R. J. Phillips (2002). Thermal and crustal evolution of Mars, *Journal of Geophysical Research*. Vol 107, E5052.

Lodders, K., and B. Fegley, B (1997). An oxygen isotope model for the composition of Mars, *Icarus* Vol. 126, 373-394.

Karato, S., and P. Wu (1993). Rheology of the upper mantle: A synthesis, *Science*, Vol. 260, 771-778.

Kaula, W. M., Theory of statistical analysis of data distributed over a sphere, *Rev. Geophys*., Vol 5, 83–107, 1967

Kaula,W. M. (1963a.). The investigation of the gravitational fields of the moon and planets with artificial satellites *Space Sci. Technol*., Vol 5, 210-230,

Kiefer, W. S. (2003). Melting in the Martian mantle: Shergottite formation and implications for present-day mantle convection on Mars, *Meteoritics* , Vol 38, 1815 1832.

Kiefer, W.S., B.G. Bills and R.S. Nerem (1996). An inversion of gravity and topography for mantle and crustal structure on Mars, *Journal of Geophysical Research*. Vol 101, 9239-9252.

Konopliv, A. S. et al (2006). A global solution for the Mars static and seasonal gravity, Mars orientation, Phobos and Deimos masses, and Mars ephemeris, *Icarus*, Vol. 182, 23–50.

Lowry, A. R., and S. Zhong (2003). Surface versus internal loading of the Tharsis rise, Mars, *Journal of Geophysical Research*. E9, 5099,

Melosh, H.J (2011). Planetary Surface Processes. Cambridge University Press.

Neumann, G.A. et al (2004). Crustal structure of Mars from gravity and topography. *Journal of Geophysical Research*. Vol. 109. doi:10.1029/2004JE002262.

Nimmo, F. and D.J. Stevenson (2000). Influence of early plate tectonics on the thermal evolution and magnetic field of Mars, *Journal of Geophysical Research*. Vol 105, 11,969-11,979.

Redmond, H. L. and S.D. King (2004). A numerical study of a mantle plume beneath the Tharsis Rise: Reconciling dynamic uplift and lithospheric support models, J *Journal of Geophysical Research*. Vol, 109, E09008.

Richards, M. A., and B. H. Hager (1984). Geoid anomalies in a dynamic earth, *Journal of Geophysical Research*. Vol 89 5987-6002.

Roberts, J.H. and S. Zhong (2006). Degree-1 convection in the Martian mantle and the origin of the hemispheric dichotomy, *Journal of Geophysical Research*. Vol 111.

Ruedas, T., Tackley. P. J. and S.C. Solomon (2013a). Thermal and compositional evolution of the Martian mantle: Effects of water, *Phys. Earth Planet. Inter*. 220, 50-72, doi:10.1016/j.pepi.2013.04.006.

Ruedas, T., Tackley. P. J. and S.C. Solomon (2013b). Thermal and compositional evolution of the Martian mantle: Effects of phase transitions and melting*, Phys. Earth Planet. Inter*. 216, 32-58, doi:10.1016/j.pepi.2012.12.002

Sekhar. P and S.D. King (2014). 3D spherical models of Martian mantle convection constrained by melting history. *Earth and Planetary Science Letters* Vol. 388, 27–37.

Smith, D.E., et al (1993). An improved gravity model for Mars: Goddard Mars Model 1, J. Geophys. Res., Vol. 98, 20,871-20,889.

Smith, D.E., et al (1999). The gravity field of Mars; results from Mars Global Surveyor,

Science, Vol 286, 94- 97.

Smith, D. E. et al (2001). Mars Orbiter Laser Altimeter: Experiment summary after the first year of global mapping of Mars, *Journal of Geophysical Research*. Vol 106, 23,689-23,722.

Sleep, N. H., and R. J. Phillips (1985). Gravity and lithospheric stress on the terrestrial planets with reference to the Tharsis region of Mars, *Journal of Geophysical Research*. Vol 90, 4469-4489.

Tan, E., Choi et al (2006) .Geo Framework: Coupling multiple models of mantle convection within a computational framework , *Geochemistry Geophysics Geosystems* 7 (6).

Turcotte, D. L. et al (1981). Role of membrane stresses in support of planetary topography, *Journal of Geophysical Research*. Vol 86, 3951-3959.

Wahr, J (1996). Gravity and Geodesy.

Wanke, H., and G. Dreibus (1994). Chemistry and Accretion History of Mars, Philosophical Transactions: Physical Sciences and Engineering 349 (1690) 285-293.

Wieczorek, M. A. (2007). Gravity and Topography of the Terrestrial Planets, in *Treatise on Geophysics*, T. Spohn and G. Schubert (eds.), Vol. 10, 165-206, Elsevier.

Wieczorek, M. A. and R. J. Phillips (1998). Potential anomalies on a sphere: Applications to the thickness of the lunar crust. *Journal of Geophysical Research*, Vol. 103, No. E1, 1715-1724.

Zhong, S (2002). Effects of lithosphere on the long-wavelength gravity anomalies and their implications for the formation of the Tharsis rise on Mars, *Journal of Geophysical Research*. Vol 107(E7), 5054.

Zhong, S. et al (2000). Role of temperature-dependent viscosity and surface plates in spherical shell models of mantle convection, *Journal of Geophysical Research*. Vol 105 (B5), 11063–11082.

Zhong, S. et al (2008). A benchmark study on mantle convection in a 3-D spherical shell using CitcomS, *Geochem .Geophys. Geosyst*., 9.

Zuber, M. T. et al. (2000) Internal structure and earth thermal evolution of Mars from Mars Global Surveyor topography and gravity, Science, 287, 1788-1793.

Figures

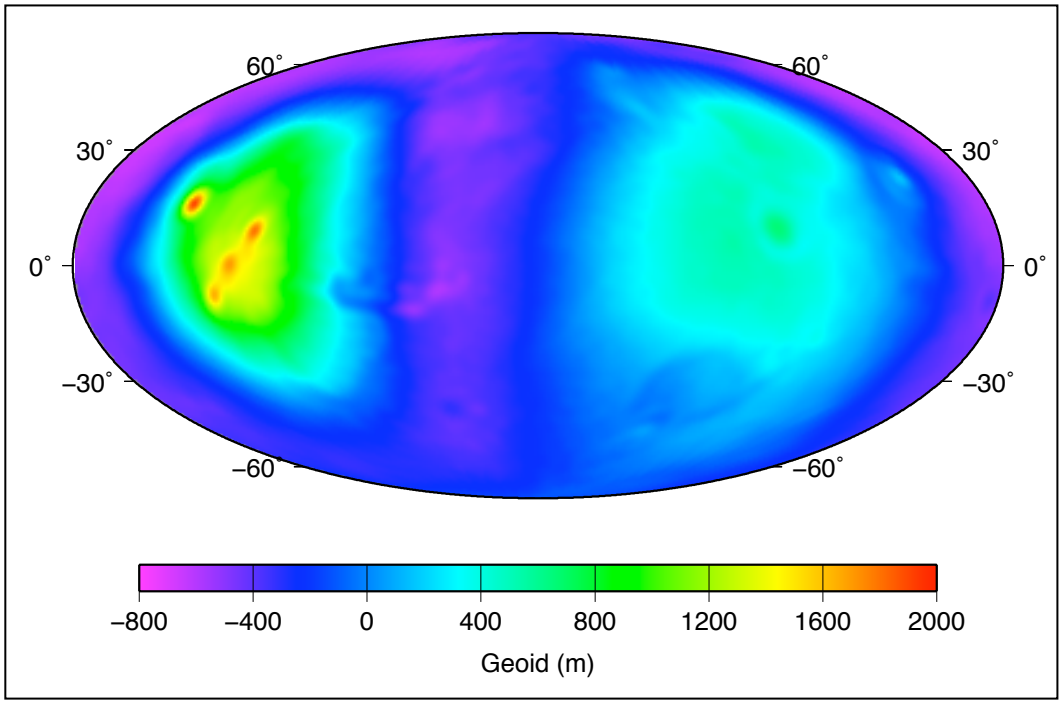

Figure 3.1 Martian Geoid using the gravitational potential model JGM95.

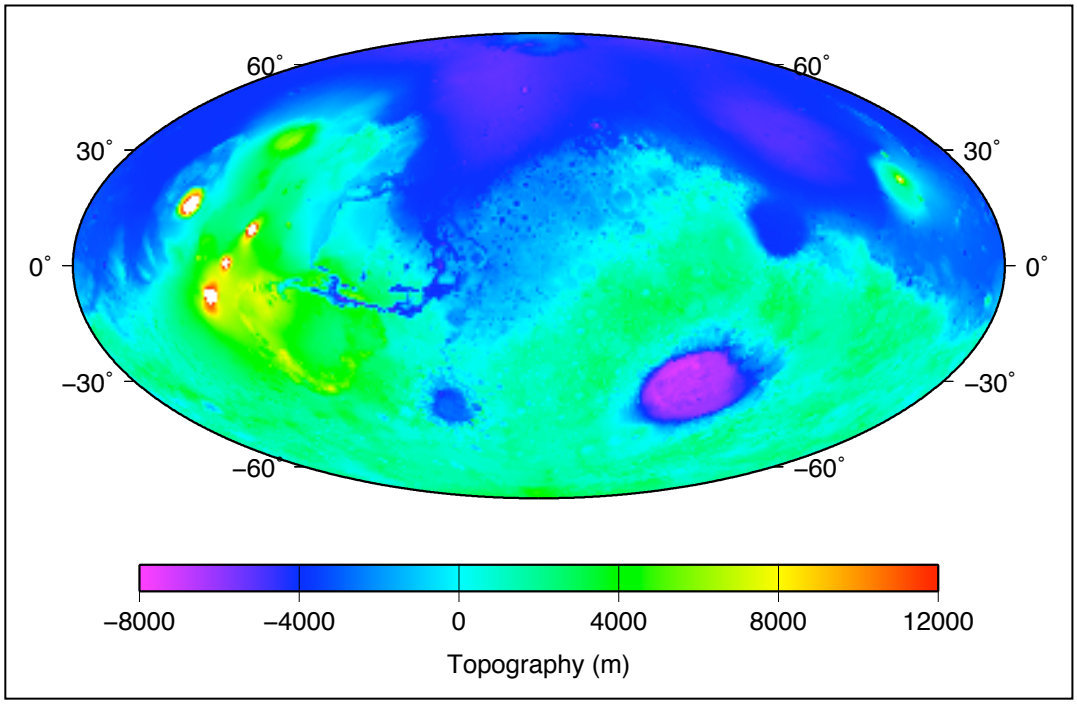

Figure 3.2 Mars topography from the topographic data MarsTopo2500.shape.

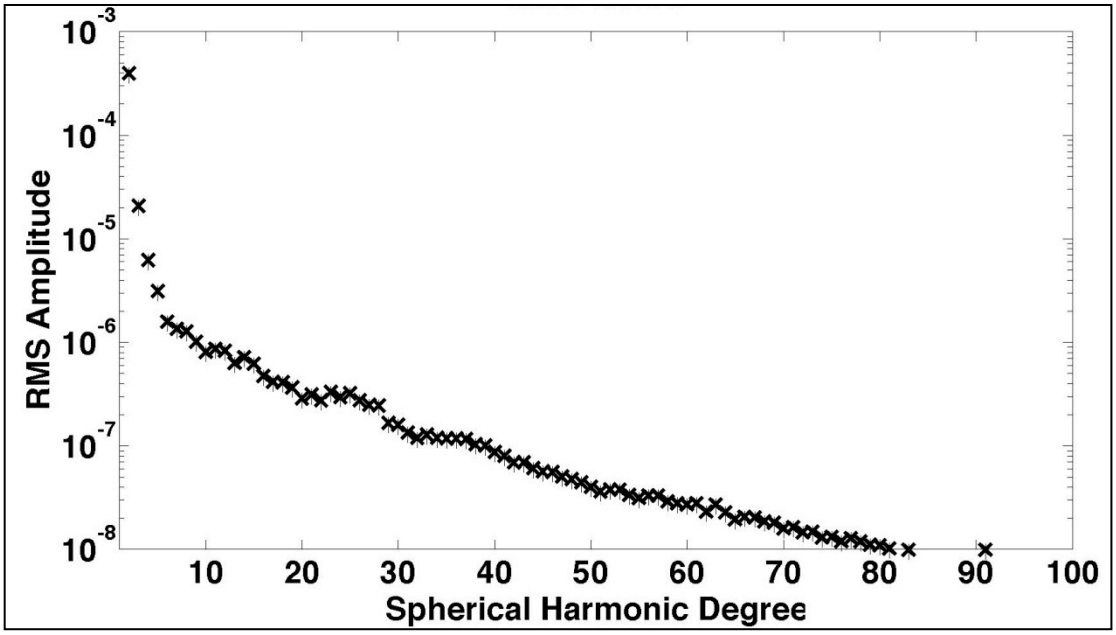

Figure 3.3 Root mean square amplitude of the gravitational potential of Mars from MGS data (jgm95j01.sha) as a function of spherical harmonic degree.

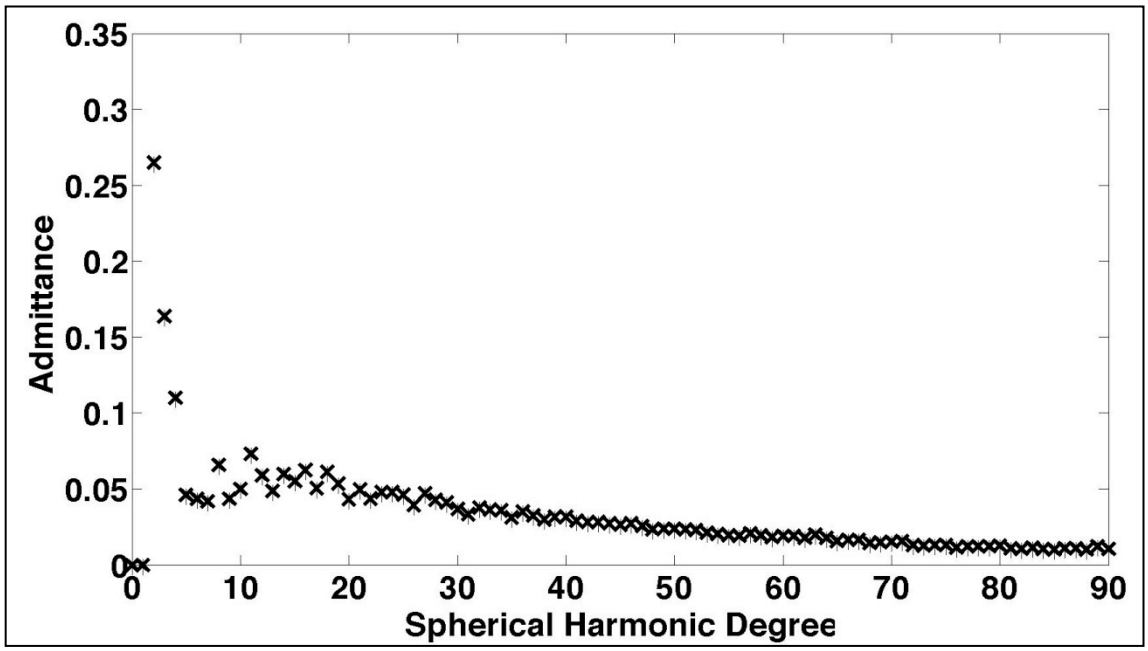

Figure 3.4 Observed admittances as a function of spherical harmonic degree.

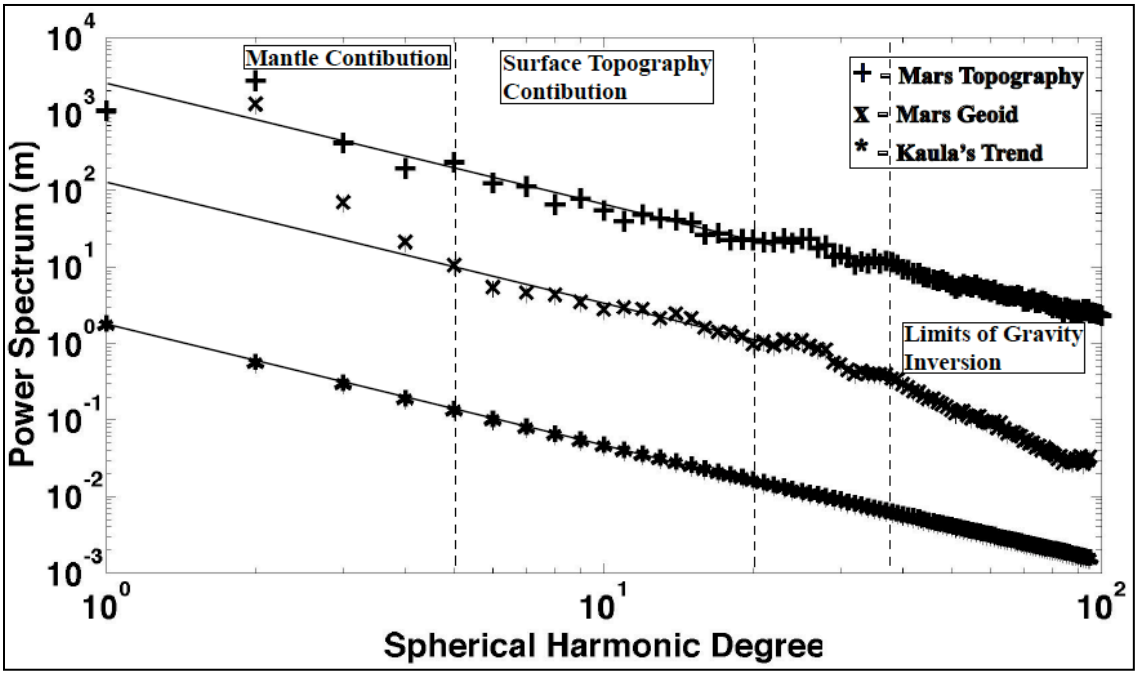

Figure 3.5 Power spectra for Mars Topography data (MarsTopo2600.shape from *Wieczorek*'s Planetary Topography data), Mars Geoid data (jgm95j01.sha from *Wieczorek*, 2007) and Kaula's rule (Equation 3).

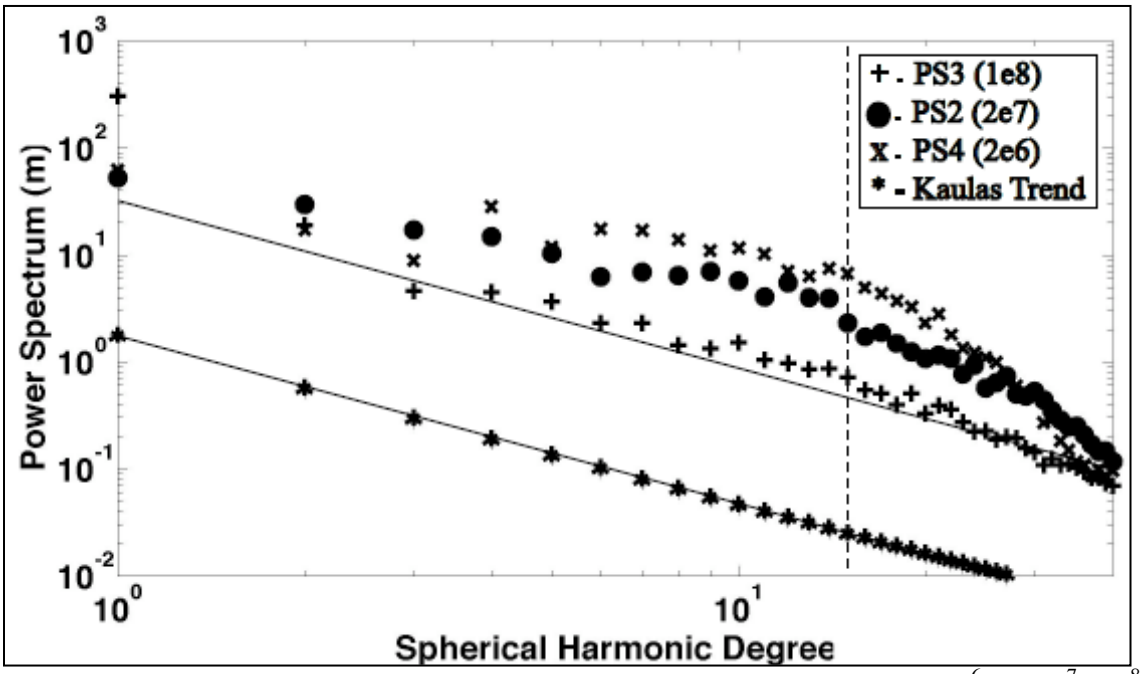

Figure 3.6 Final step power spectra for varying Rayleigh numbers, $2x10^6$, $2x10^7$, 10^8 compared with Kaula's power rule. All models have an internal heat of 49.66 and temperature-dependent viscosity, 8 times increase in viscosity at 996 km depth.

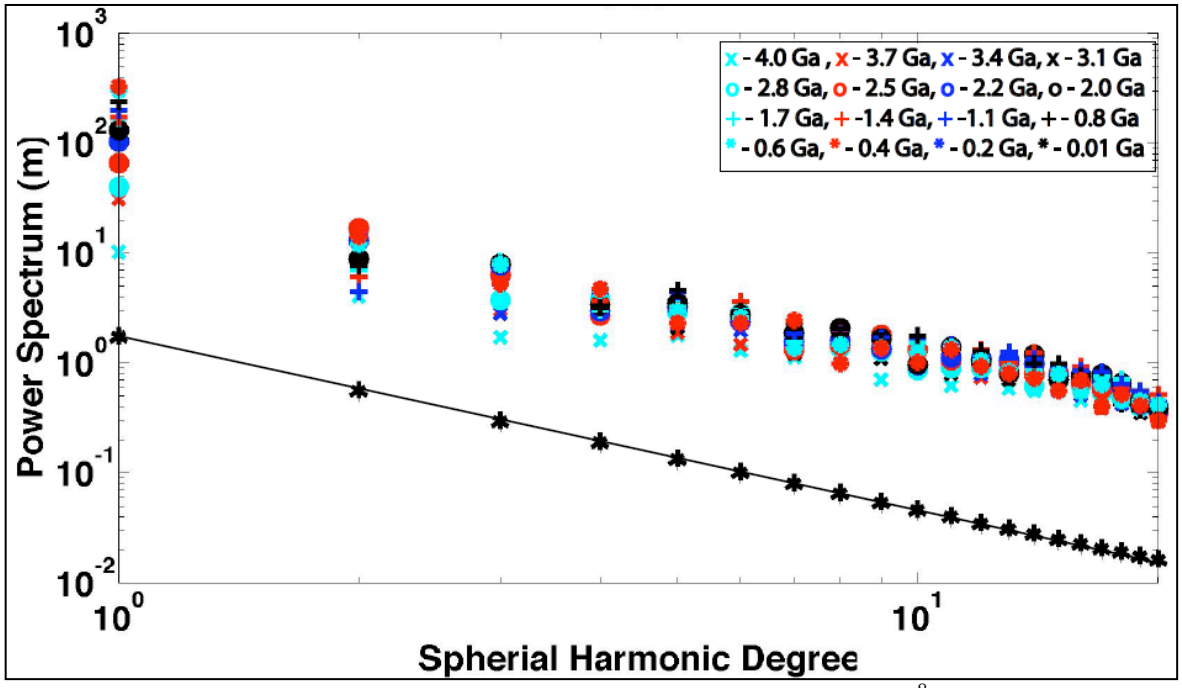

Figure 3.7 All the time steps for the high Rayleigh calculation, PS3 (10^8) with a viscosity of the lower mantle being 8 times higher than the upper mantle and internal heat of 49.66.

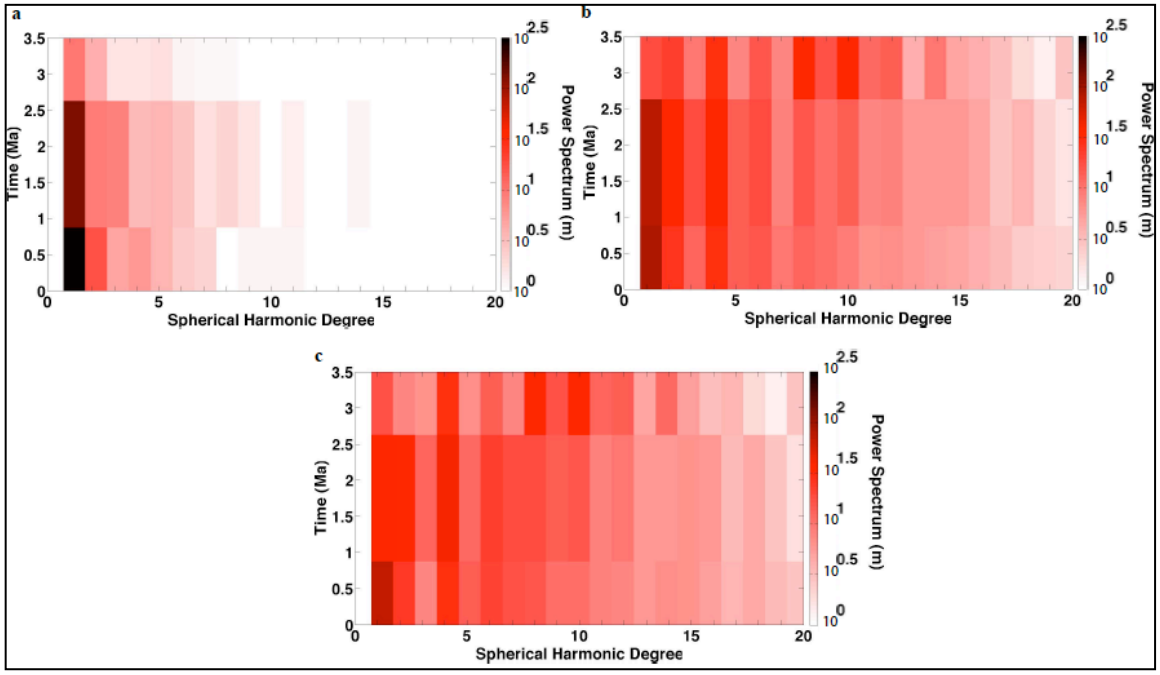

Figure 3.8 Power Spectrum through the evolution of the models a) PS3, b) PS2 and c) PS4.

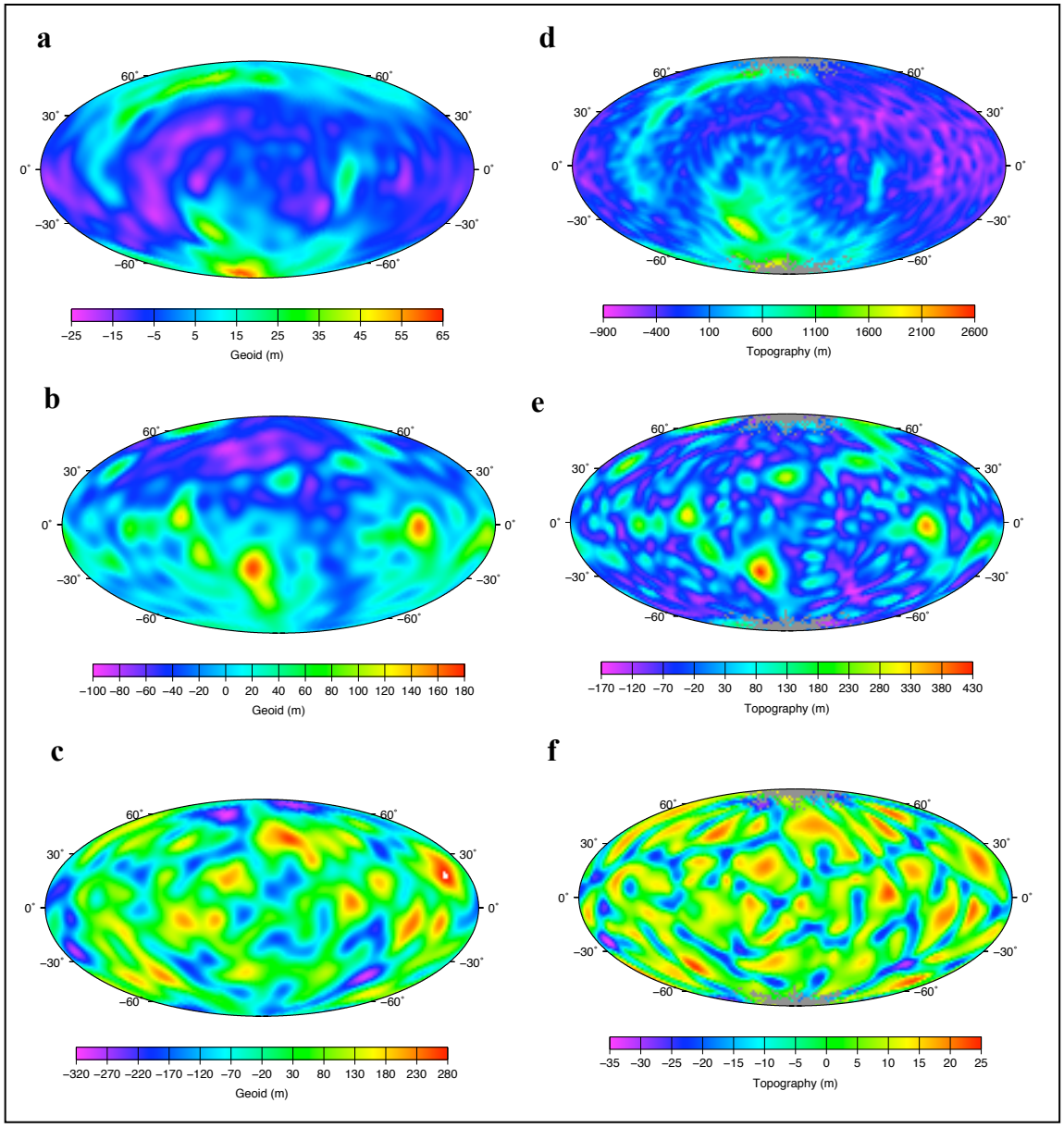

Figure 3.9 Geoid and topography for steady state of models PS3 (a) and (d), PS2 (b) and (e) and PS4 (c) and (f). The geoid of PS3 has degree-1 component removed in this figure.

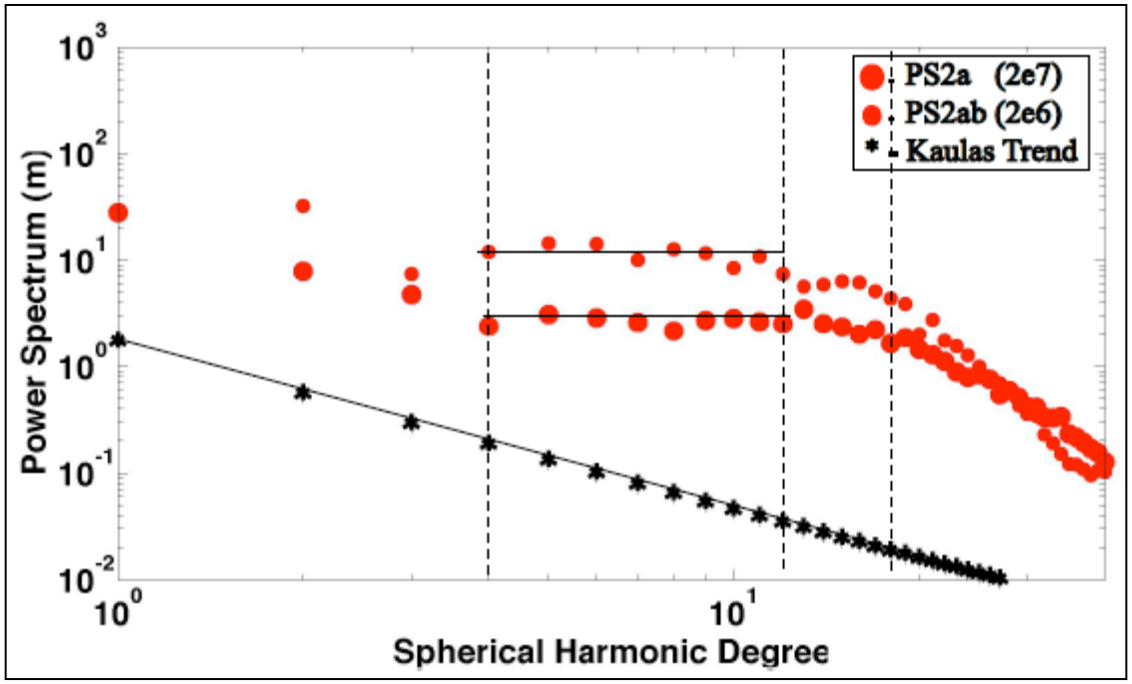

Figure 3.10 Present day power spectrum for varying Rayleigh number, PS2 and PS2b ($2x10^7$ and $2x10^6$ respectively) with an isoviscous structure and internal heat of 49.66. PS2 and PS2b in comparison to Kaula's power rule.

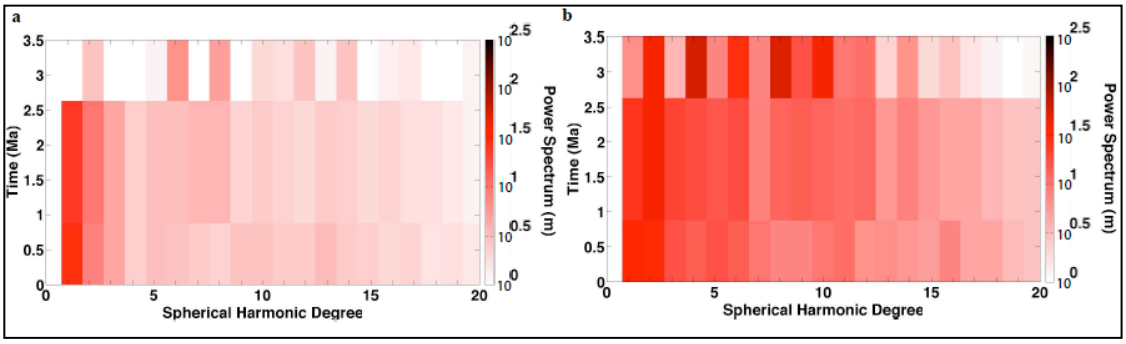

Figure 3.11 Power Spectrum through the evolution of the models a) PS2a and b) PS2ab.

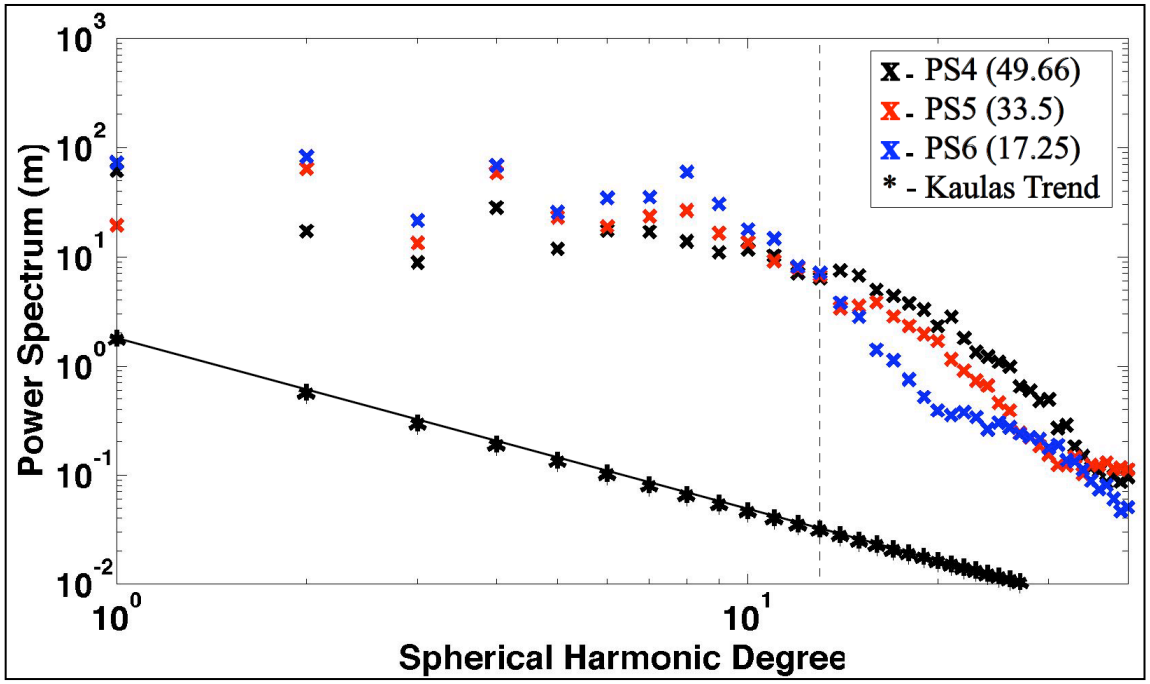

Figure 3.12 Present day power spectrum for varying internal heat models, PS4 (49.66), PS5 (33.5) and PS6 (17.25) with a Rayleigh number of $2x10^6$ and lower mantle being 8 times the viscosity of the upper mantle, in comparison to Kaula's power rule. The high internal heat is following *Roberts and Zhong* (2006) work and 17.25 is based on *Wanke and Dreibus* (1994) composition.

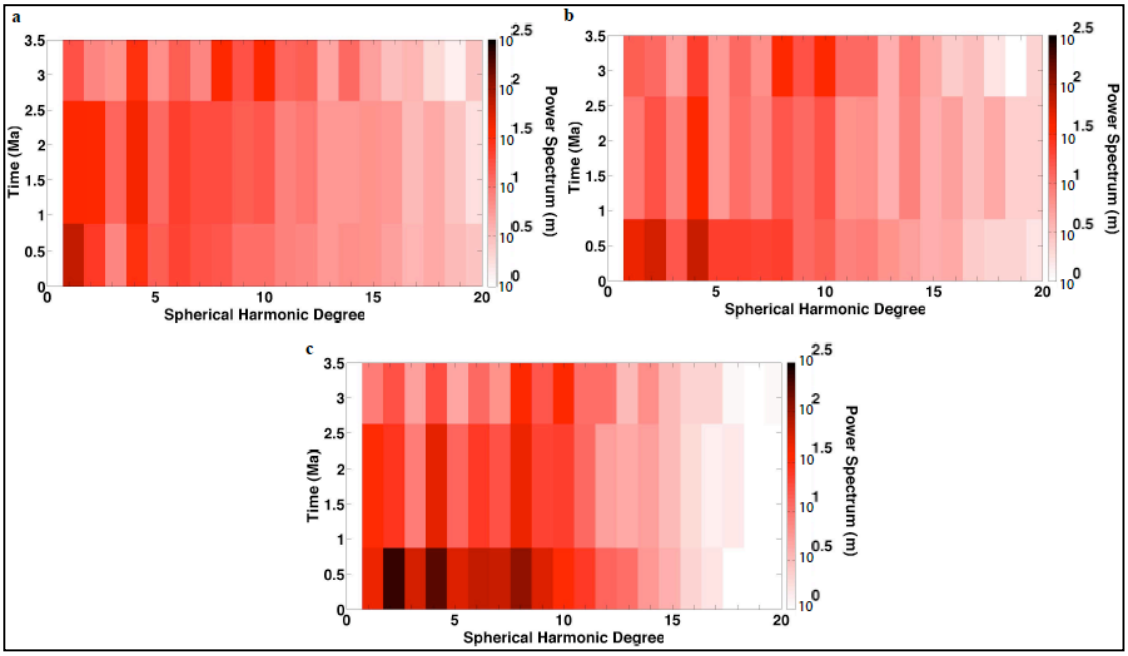

Figure 3.13 Power Spectrum through the evolution of the models a) PS4, b) PS5 and c) PS6.

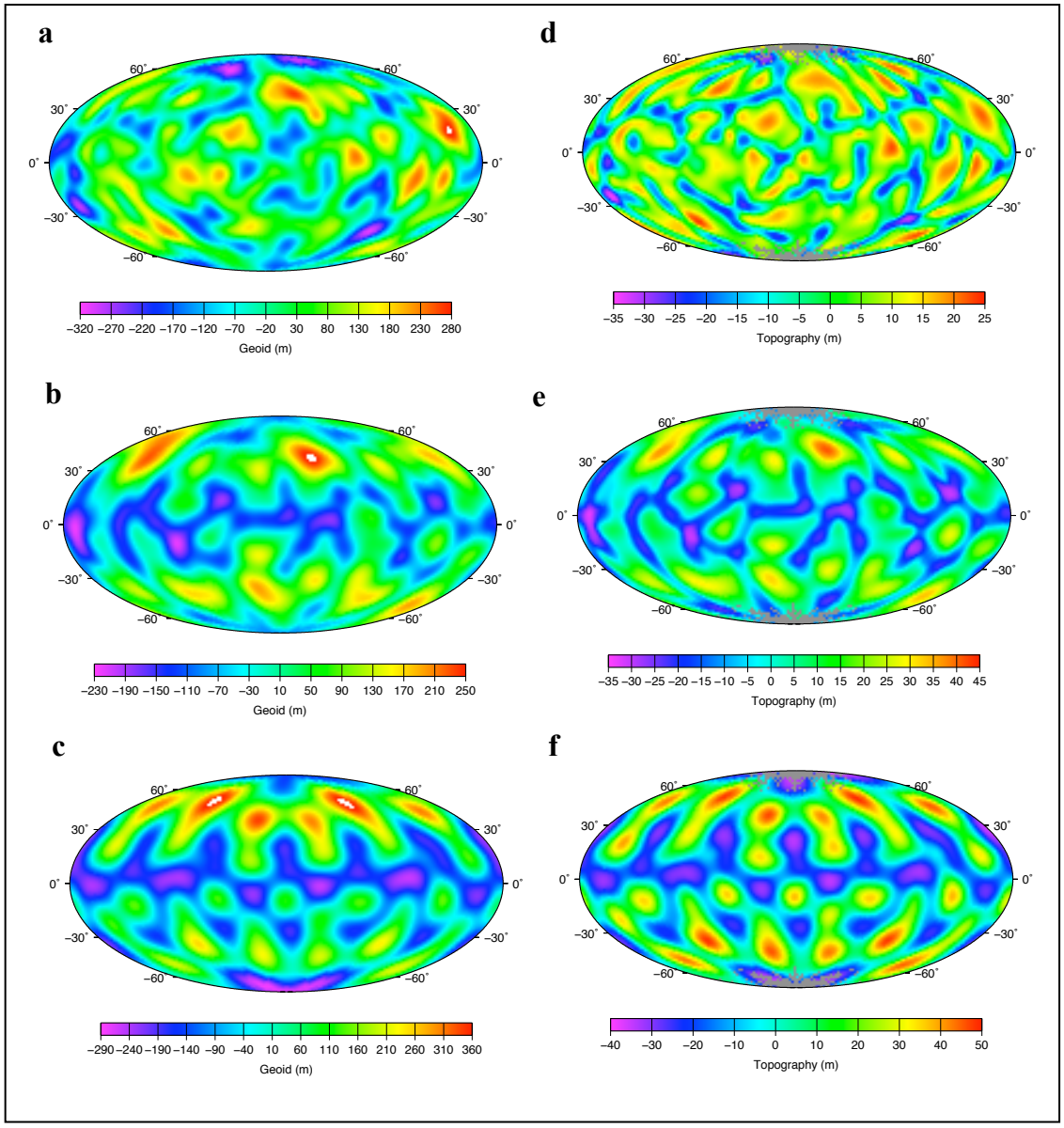

Figure 3.14 Geoid and topography for steady state of models PS4 (a) and (d), PS5 (b) and (e) and PS6 (c) and (f).

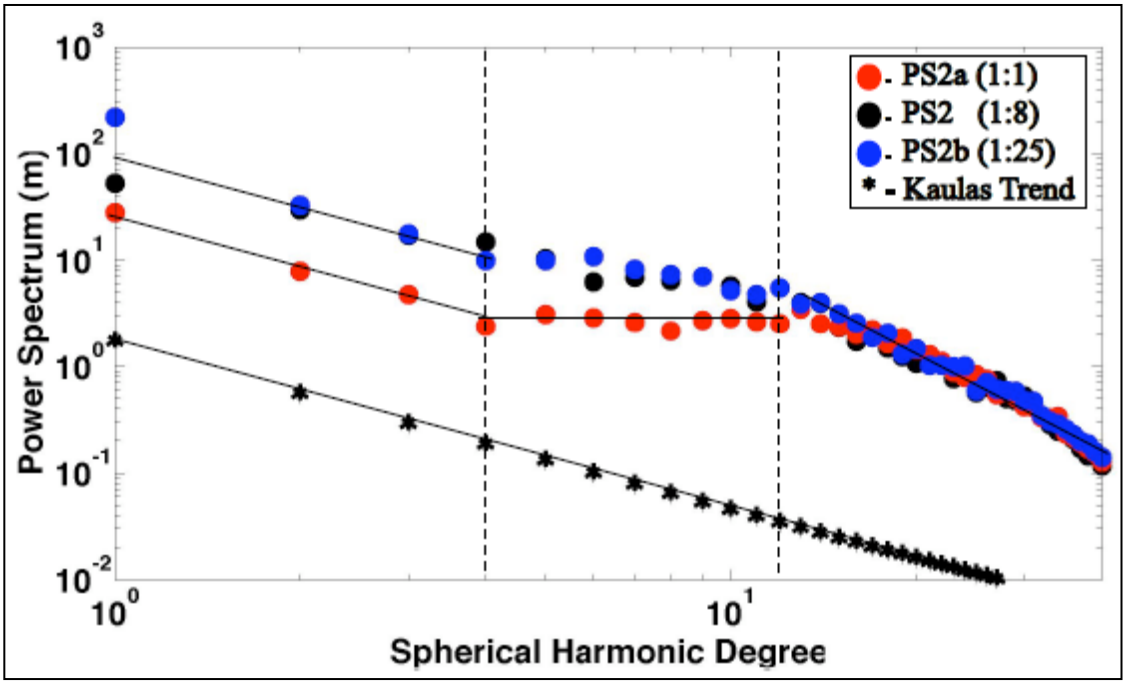

Figure 3.15 Final step power spectrum for varying viscosity layer models, isoviscous (1:1), higher viscosity in the lower mantle (1:8 and 1:25), in comparison to Kaula's power rule for a Rayleigh number of $2x10^7$ and internal heat of 49.66.

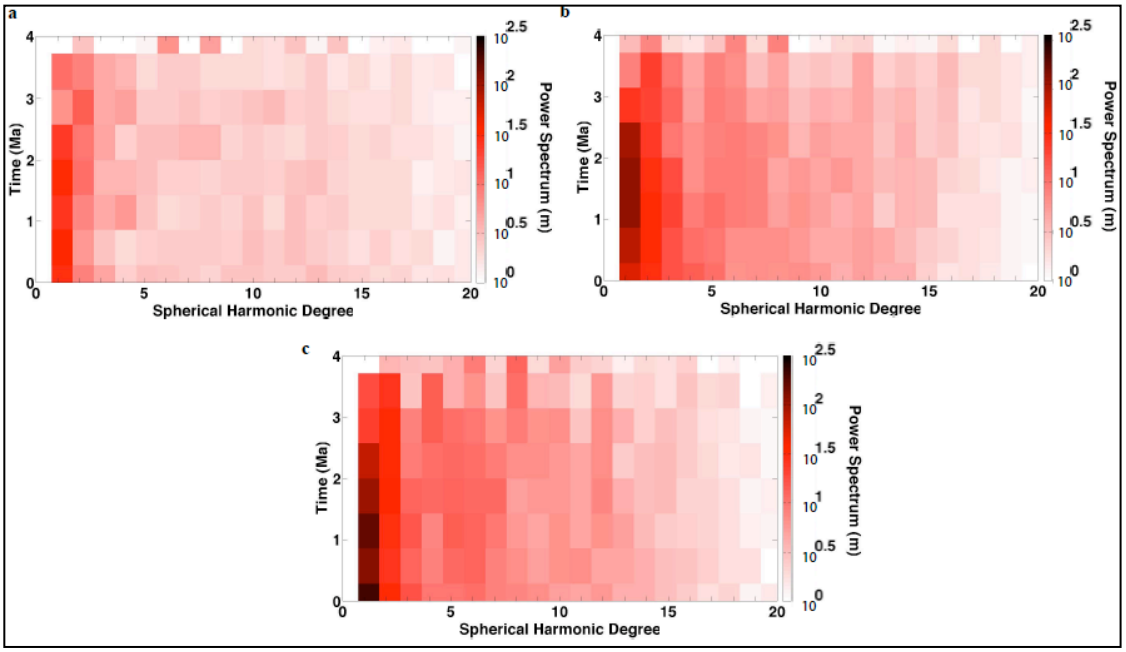

Figure 3.16 Power Spectrum through the evolution of the models a) PS2a, b) PS2 and c) PS2b.

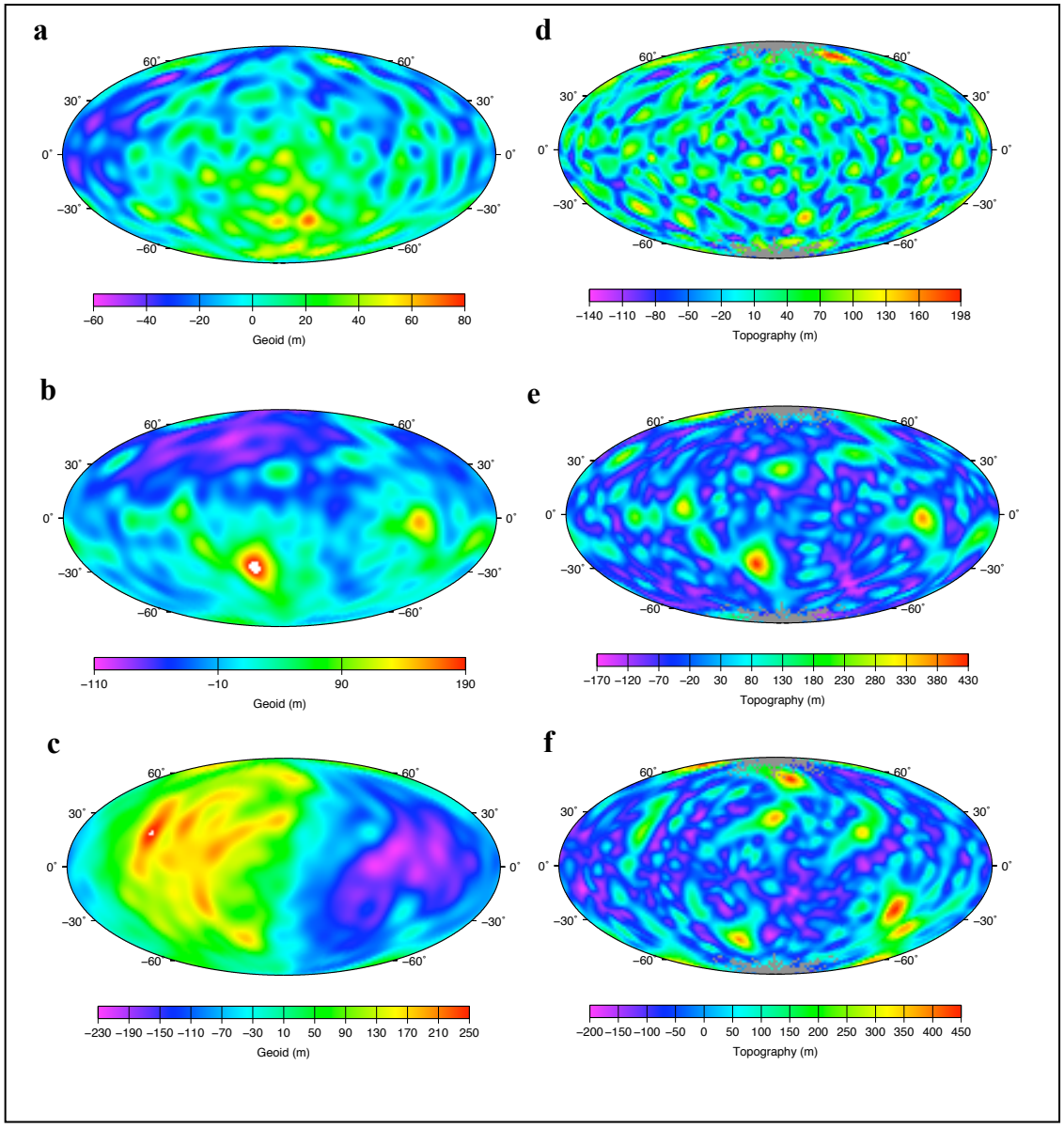

Figure 3.17 Geoid and topography for steady state of models PS2a (a) and (d), PS2 (b) and (e) and PS2b (c) and (f).

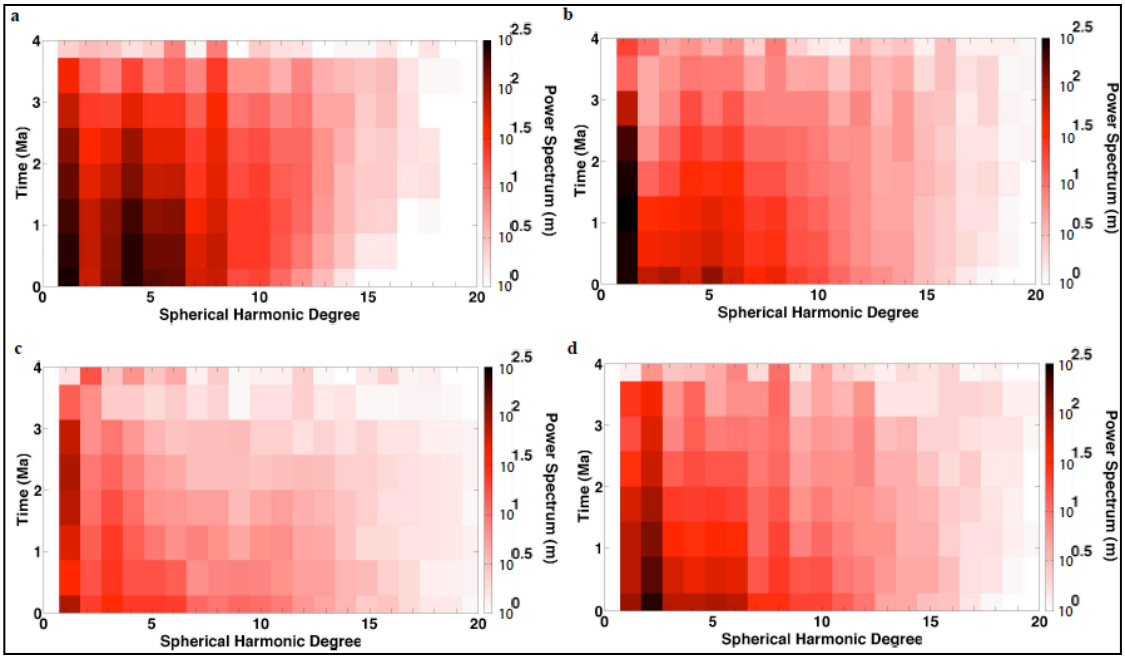

Figure 3.18 Power Spectrum through the evolution of the models a) SK1, b) SK2, c) SK3 and d) SK4.

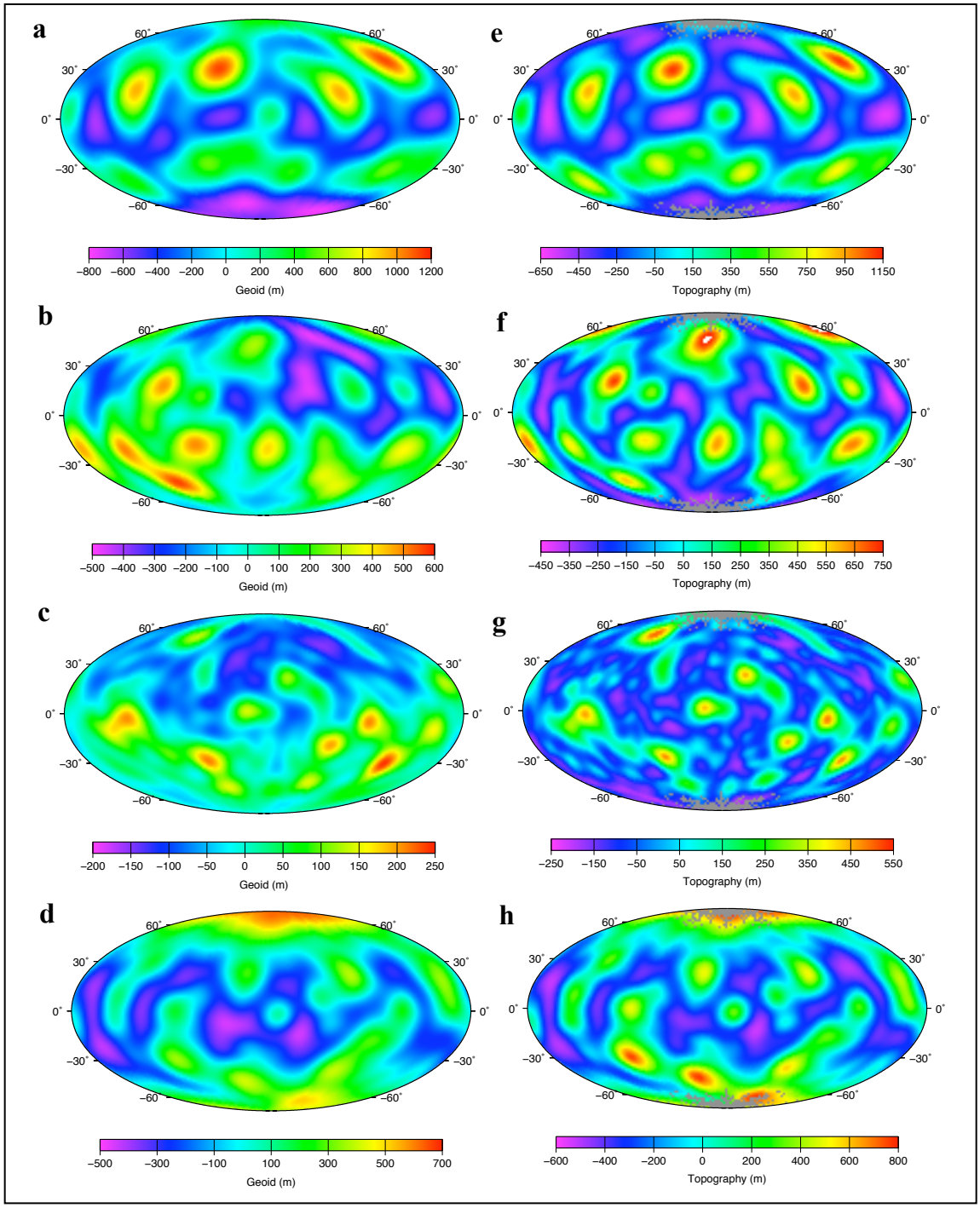

Figure 3.19 Geoid and topography for steady state of models SK1 (a) and (e), SK2 (b) and (f), SK3 (c) and (g) and SK4 (d) and (h).

Tables

Parameter	Symbol	Value
Default internal heating rate	Q	7.4×10^{-8} W m^{-3}
Planetary radius	R_p	3.398×10^{6} m
Density of the mantle	ρ_m	3.40×10^{3} kg m^{-3}
Specific heat	C_p	1200 J K^{-1} kg^{-1}
Temperature difference across the mantle	ΔT	1600 K
Thermal Diffusivity	κ	1.0×10^{-6} m^2 s^{-1}
Gravitational Acceleration	g	3.72 m s^{-2}
Thermal expansion co-efficient	α	3.0×10^{-5} K^{-1}
Reference viscosity	η_o	1.0×10^{21} Pa s
Activation Energy	E	157 kJ mol^{-1}
Universal Gas Constant	R	8.3144 J K^{-1} mol^{-1}
Activation Volume	V	3.61×10^{-6} m^3 mol^{-1}
Surface Temperature	T_{surf}	220 K
Latent heat of melting	H_l	6.4×10^{5} J kg^{-1}

Table 3.1 Model Parameters

Case	Ra	H_{in} for Constant Heat source	Partitioning of radioactivity (Crust fraction)	η	$\eta_{lower}/\eta_{upper}$
PS2a	2.24e7	49.66	-	1e21	1:1
PS2	2.24e7	49.66	-	1e21	1:8
PS2b	2.24e7	49.66		1e21	1:25
PS2ab	2.24e6	49.66	-	1e22	1:1
PS3	1.25e8	49.66	-	1e20	1:8
PS4	2.24e6	49.66	-	1e22	1:8
PS5	2.24e6	33.50	-	1e22	1:8
PS6	2.24e6	17.25	-	1e22	1:8
DECAYING HEAT SOURCES					
SK1	2.24e7	-	100	1e21	1:8
SK2	2.24e7	-	60	1e21	1:8
SK3	2.24e7	-	0	1e21	1:8
SK4	2.24e7	-	60	1e21	1:25

Table 3.2 Model parameters for Constant and Decaying heat sources.

Chapter 4

Non-Newtonian Convection Modeling and the Possibility of Internal Activity on Ceres

Abstract

Ceres, the largest body in the asteroid belt, is believed to have undergone an evolutionary process similar to planets. The comparatively small size of Ceres suggests that it should have cooled early in its formation and should be geologically inactive. However, recent spectral studies of Ceres show the presence of brucite, magnesium carbonates, and serpentine on the surface suggesting that the interior of Ceres may have been active in the recent past. We present calculations of convection within an icy, differentiated body with a silicate core and an ice-silicate mantle to study the evolution of Ceres. We start from a warm but solid interior using a non-Newtonian rheology for the ice-silicate mantle dominated by the viscosity of ice (strain-rate dependent). We vary the percentage of ice and silicate in the mantle, which in turn changes the size of the core. Our results indicate a wide-range of parameters where convection within Ceres persists to present day. We estimate surface deformation, topography, geoid, and heat flow from our models, which can be compared with observational data when the Dawn mission arrives at Ceres in 2015.

4.1 Introduction

Ceres is the largest body in the asteroid belt (*Thomas et al.,* 2005*; Carry et al.,* 2008) but is smaller than Earth's Moon and has been categorized as a planet (*McCord and Sotin,* 2005), asteroid (*McCord and Sotin,* 2005), protoplanet and more recently as a dwarf planet (*Castillo-Rogez and McCord*, 2010*; McCord et al.,* 2011). While it is commonly assumed that Ceres formed in the outer part of the main asteroid belt (*Turrini et al.,* 2009*; McCord et al.,* 2011) and moved inward as Jupiter migrated towards the Sun (*Walsh et al.,* 2010; *O'Brien et al.,* 2010), retaining it's volatile components (*Mousis and Alibert,* 2005); it has also been suggested that it may have migrated from the Kuiper belt (*McKinnon,* 2008) or trans-Neptunian region (eg, *Gomes et al.,* 2005). It is believed that Ceres has retained some of its primordial elements, and is one of the earliest planetoids (*McCord and Sotin,* 2005). Therefore, studying Ceres provides pivotal information to the evolution of planetary bodies and more specifically the role of volatiles during the early stages of the solar system (*Carry et al.,* 2008). This was the main motivation by NASA for the Dawn mission to orbit Vesta and Ceres (*Carry et al.,* 2008).

Ceres contains one-third of the total mass between Mars and Jupiter (e.g., *Krasinsky et al.* 2002; *Pitjeva* 2003) and estimates of the mass of Ceres range from 8.732×10^{20} kg (*Hilton*, 1999) to 9.43×10^{20} kg (*Viateau and Rapaport,* 1998; *Michalak,* 2000; *Standish,* 2001; *Kovacevic and Kuzmanoski,* 2007; *Carry et al.,* 2008; *Zolotov,* 2009). Hilton's value is significantly smaller than the more recent studies cited above and the 9.43×10^{20} kg value has been generally used in modeling studies (e.g. *McCord and Sotin,* 2005).

As discussed by *McCord and Sotin* (2005), there have been three different methods of measuring the size and shape of Ceres: (1) occultation of a star by Ceres as seen from the Earth (*Millis et al.,* 1987) giving equatorial and polar radii of 479.6 km and 453.4 km, (2) Hubble Space Telescope camera direct imaging (*Parker et al.,* 2006) giving semimajor and semiminor axes of 484.8 km and 466.4 km and (3) adaptive optics (AO) imaging with ground-based telescopes (*Drummond et al.,* 1998) giving radii of 508 km and 472.5 km. *McCord and Sotin* (2005) average these and estimate an average equatorial radius of 485 km, an average polar radius of 455 km and an effective

spherically symmetric radius of 475 km. This is higher than 467 km (*Carry et al.,* 2008) and closer to 479 km (*Millis et al.,* 1987; *McCord and Sotin,* 2005; *Thomas et al.,* 2005).

Using mass and size information estimates of Ceres' density vary between 2077 kg/m^3 (*Thomas et al.,* 2005; *Castillo-Rogez and McCord*, 2010) and 2206 kg/m^3 (*Carry et al.,* 2008; *Zolotov*, 2009). Because Ceres' shape is nearly spherical, self-gravitation should be sufficient for the body to experience internal compression which will eliminate pore spaces. Thus, the low density strongly suggests the presence of a significant fraction of the body is water ice. This range of densities is similar to that of CI-type chondrites (*Britt and Consolmagno*, 2000; *McCord and Sotin*, 2005; *Carry et al.,* 2008; *Castillo-Rogez and McCord*, 2010).

Ground based observations (*Dumas et al.,* 2003) and Hubble Space Telescope imaging (*Thomas et al.*, 2005; *Li et al.,* 2006; *Parker et al*., 2006; *Castillo-Rogez and McCord*, 2010) indicate that Ceres is a symmetrically shaped spheroid (*McCord et al., 2011*) or rotationally symmetric (*Carry et al.,* 2008) oblate spheroid. The oblate spheroid shape suggests that Ceres is a differentiated body with a core and a less dense mantle (*Parker et al*., 2006), suggesting a large presence of ice and volatile elements in the interior (*Carry et al.*, 2008). *Castillo-Rogez and McCord* (2010) used a dry ordinary chondritic composition with a density of 3510 kg/m^3 in their model, which constrains the fraction of silicate to be 74% of the mass and the water fraction to be 26% of the mass (*Grimm and McSween*, 1989; *Wilson et al.,* 1999; *McCord and Sotin,* 2005; *Thomas et al.,* 2005; *Li et al.,* 2006; *Castillo-Rogez and McCord*, 2010; *McCord et al.,* 2011). The density of Ceres is also similar to the densities of Ganymede and Calisto, both of which have a significant mass fraction of water ice.

Based on geophysical observations and dynamic modeling, recent studies have indicated that Ceres has undergone evolutionary processes similar to the icy outer satellites of Jupiter, showing signs of water alteration on the surface (*Carry et al.,* 2008; *Castillo-Rogez and McCord*, 2010; *McCord et al.,* 2011). Ceres is wetter, less evolved, and less dense than Vesta and more like Callisto and Ganymede (*McCord and Sotin*, 2005), retaining most of its original water (*Castillo-Rogez and McCord*, 2010; *McCord et al.,* 2011) and this higher fraction of water sets it apart from the other rocky asteroids (*Li*

et al., 2006). Additionally, the exciting recent observations of water vapor by *Kuppers et al.* (2014) describe possible current day releases of water through sublimation or cryovolcanism.

Numerical modeling addressed the likelihood that Ceres is a differentiated body (*McCord and Sotin*, 2005). *McCord and Sotin* (2005) start from a homogeneous mixture with a 74% mass fraction of silicate and 26% mass fraction of ice. The timing of accretion impacts the evolution of Ceres. *McCord and Sotin* (2005) began accretion 2.4 Myr after the formation of CAIs (*Ghosh and McSween*, 1998; *Srinivasan et al.,* 1999) to avoid complete evaporation of water ice, and assume accretion finished before 5 Myr. In this case, the heat from the decay of Al^{26} melts the ice, leading to an undifferentiated body. While *McCord and Sotin* (2005) assumed that heat transfer in the interior is due to conduction, *Castillo-Rogez and McCord* (2010) considered convection with the same time of formation, and found higher internal temperatures that resulted in hydration of silicates, ice melting, and differentiation. If accretion occurs over a longer period of time, such that the decay of short-lived radioisotopes such as Al^{26} are less dominant, long-lived radiogenic heat sources still raise the temperature causing ice and silicate to separate but silicate and iron do not differentiate. The low temperatures and high conductivity of the surface layer prevents the outer layer of silicate and ice mixture from melting but still results in a differentiated structure with an ice mantle and rock-iron core (*McCord and Sotin*, 2005; *Castillo-Rogez and McCord*, 2010; *McCord et al.,* 2011). The presence of ammonia decreases the melting temperature of ice by 100 K (*Sotin et al.,* 1997; *McCord and Sotin,* 2005) and differentiates the model into a silicate core, liquid ocean, convective ice and conductive ice layer (*McCord and Sotin*, 2005). *Zolotov* (2009) suggested an undifferentiated Ceres composed of hydrated silicates that could have accreted after the decay of Al^{26} and therefore would have undergone very little thermal evolution process and volatiles would be absent.

Surface features suggest that Ceres underwent re-surfacing due to cryovolcanism or venting of water vapor (*Li et al.,* 2006; *McCord et al.,* 2011) and carbonates and brucite have been identified on the surface globally (*Carry et al.,* 2008; *Rivkin et al.,* 2006; *Milliken and Rivkin*, 2009). The presence of these minerals suggests that aqueous

alteration of olive-rich rocks has occurred and hydrothermal systems have been active near the surface (*Rivkin and Volquardsen*, 2008; *Milliken and Rivkin*, 2009). Phyllosilicates and carbonates are also suspected to be present on the surface, based on comparison of near infrared mapping of Ceres and laboratory sample studies (*Carry et al.,* 2008). Spectral analysis shows a strong absorption of hydrated minerals (*Jones et al.,* 1990; *Sato et al.,* 1997; *Carry et al.,* 2008). Based on the presence of hydrothermally altered clays (*Li et al.,* 2006; *Rivkin et al.,* 2006) and salts on the surface, it appears similar to the composition of carboneous chondrite (Cc) type meteorites (*Johnson and Fanale*, 1973), more precisely CI and CM meteorites (*Lebofsky*, 1978; *McCord and Sotin*, 2005, *Rivkin et al.,* 2006, *Castillo-Rogez and McCord*, 2010). However, the spectral features of carbonate and brucite observed on Ceres are abundantly greater than on carboneous chondrite meteorites suggesting that the thermal evolution of Ceres differs from carboneous chondrite meteorites (*Milliken and Rivkin*, 2009). Other than Earth and Mars, Ceres is the only other object in the solar system on which carbonates have been identified (*Castillo-Rogez and McCord*, 2010).

4.2 Mantle Convection Model

Based on the average density of Ceres and the abundance of elements in the solar system, we assume that Ceres is composed of silicate-ice mixture. Therefore, we apply a viscosity for the interior of Ceres based on an ice-silicate rheology ratio. We calculate the viscosity of ice using the grain boundary sliding mechanism, following *Solomatov* (1995) and *Barr et al* (2004). The viscosity due to grain boundary sliding is dependent on temperature and strain-rate parameters and is given by,

$$\eta = \left(\frac{d^p}{A}\right)^{1/n} \dot{\varepsilon}_{II}^{(1-n)/n} exp\left(\frac{Q^*}{nRT_m}\right) \quad (1)$$

where d is the grain size of ice, p is the grain-size exponent, A is the pre-exponential parameter in the Ice-1 rheology law (*Goldsby and Kohlstedt,* 2001), Q^* is the activation energy, n is the stress exponent, R is the gas constant and T_m is the melt temperature (Table 4.1). $\dot{\varepsilon}_{II}$ is the second invariant of the strain rate. The strain-rate is scaled by

$$\dot{\varepsilon}_o = \frac{\kappa}{D^2} \tag{2}$$

where κ is the thermal diffusivity and D is the depth of the mantle respectively (Table 4.2).

The viscosity of ice depends strongly on temperature and controls the heat transfer by convection (*McCord and Sotin*, 2005). This value has been determined by observations of terrestrial glaciers and lab experiments (*Durham and Stern*, 2001). For grain boundary sliding, the viscosity of ice at a temperature of 273 K varies on the grain size and it corresponds to an activation energy of 49 kJ/mol.

The equations for creeping convection in an icy body are governed by Rayleigh number, a dimensionless number that is the ratio of the buoyancy of ice to the viscous stresses resisting motion. We modified the Rayleigh number calculation to accommodate an ice shell rheology (*Solomatov*, 1995; *Barr et al.,* 2004) as follows,

$$Ra = \frac{\rho g \alpha \triangle T D^{(n+2)/n}}{(\kappa d^p A^{-1})^{1/n} exp(\frac{Q^*}{nRT_m})} \tag{3}$$

where ρ, g, α, ΔT, D and κ are the mantle density, acceleration due to gravity, thermal expansion coefficient, super-adiabatic temperature difference across the mantle, depth of the mantle and thermal diffusivity respectively (Table 4.2).

4.2.1 Numerical Methods

To study the evolution of Ceres, we perform a series of calculations in a 3D spherical shell using the finite element code CitcomS-3.1.1 (*Zhong et al.,* 2000; 2008; *Tan et al.,* 2006) with 65 x 65 x 65 element in each of the 12 spherical caps. CitcomS solves the equations of conservation of mass, momentum and energy for a creeping, incompressible fluid. We consider the evolution of Ceres after differentiation into a silicate core and ice-silicate mantle and we do not include heating due to radioactive elements, which would likely be concentrated in the core. We assume varying ratios of ice-silicate mixture in the mantle consistent with the average density of Ceres. We use a non-Newtonian isoviscous rheology that is strongly dependent on temperature and stress,

where deformation occurs based on the grain-boundary sliding mechanism for Ice-1 (Equation 1). In regions of high strain rate, the viscosity decreases and this in turn increases the vigor of convection, producing a positive non-linear feedback. We begin with a warm body, just below the melting point of Ice-1 with a cold upper boundary (stagnant lid) and a non-dimensional mantle temperature of 0.95 in the interior. A perturbation of 0.01 is added to the radial temperature with a short-wavelength, spherical harmonic l=50, m=42 pattern. The surface temperature is important not only as the boundary condition for the energy equation but also because our rheology law is based on absolute temperature. Estimates of the surface temperature of Ceres vary from 235 K (*Li et al.,* 2006) to 180 K (*Fanale and Salvail*, 1989; *McCord et al.,* 2011) and 167K (*Castillo-Rogez and McCord*, 2010) at the equator and 130K (*Fanale and Salvail*, 1989; *McCord et al.,* 2011) at the poles. Based on the difference between the maximum and minimum temperature, we set the surface temperature is set to 201 K and the temperature difference across the mantle is set to 50 K. The surface temperature value compares to 200 K used by *McCord and Sotin* (2005). The temperature difference between the surface and the core mantle boundary is not large and thus the vertical gradient of viscosity in the mantle is small (*Castillo-Rogez and McCord*, 2010).

4.2.2 Viscosity of Ice-Silicate Rheology

We begin by considering the viscosity of the ice-rock mixture using the viscosity of a fluid with solid suspensions embedded in it. The viscosity of the fluid-solid mixture, η, is given by (*LeJeune and Richet*, 1995),

$$\eta = \eta_0(1 - \phi/\phi_m)^{-n} \tag{4}$$

where η_o is the viscosity of the homogeneous melt, Φ is the crystal fraction, Φ_m is the critical fraction and n is an adjustable parameter. In our case, η_o is the viscosity of ice-1, Φ is the amount of silicate material calculated in volume percent, Φ_m is assumed to be 0.6 for a random loose packing density and n is equal to the original value of 2.5. We do not consider individual silicate crystals and instead assume that we can use the crystal/liquid formulation as applicable to the ice/silicate mixture.

When the silicate fraction is 0%, the viscosity of the mixture is the viscosity of ice-1. Increasing the silicate fraction in the mantle to approximately 50% by volume increases the viscosity of the mixture by a factor of 50 over the viscosity of pure ice. Beyond a rock fraction of 50% by volume, the viscosity increases exponentially and trends toward the viscosity of silicate material. Above 59.9%, the rheology is that of the silicate material.

For a differentiated mantle structure, we assume that the core is always comprised of silicate and the mantle has varying ratios of ice and silicate as shown in Figure 4.1. Three different core sizes are explored that then determine the volume percent of silicate in the mantle. For the 90 km core, the volume of the core is so small compared with the mantle that the ratio of silicate to ice is nearly the same as the no core case. Because the volume of the core is so small, the ratio of ice to silicate in the mantle (e.g., 42% by volume silicate and 58% by volume ice) is almost equivalent to a completely undifferentiated body with no core. For a core radius of 215 km, there is a 67% ice by volume and 33% silicate by volume. When the core has a radius of 353 km, all of the silicate is in the core and the mantle is comprised only of ice.

Figure 4.2 shows the viscosity as a function of ice-silicate ratio in the mantle. We calculate the viscosity for a basic convective model with a grain size of $5x10^{-4}$ m and the straight black line shows that with increasing amounts of silicate in the mantle the viscosity of the mixture increases, following *Lejeune and Richet* (1995). The dashed line is the upper limit for a loose packing of ice-silicate particles. For Ceres, even with the maximum amount of silicate in the mantle, the viscosity of the mixture increases only by an order of magnitude. Hence, we neglect the contribution of silicate in the viscosity estimates in our modeling. However, when we calculate the viscosity for a conductive model of grain size $3x10^{-3}$ m, the viscosity of ice has a high value of $1.8x10^{18}$ Pa s. In this case, when we consider the maximum amount of silicate in the mantle, the viscosity is $4.0x10^{19}$ Pa s, which approaches the viscosity of silicate planets.

4.3 Results

The least well-constrained material parameter in the viscosity formulation is the grain size, d. Following the approach in *Barr et al.* (2004) we change the rheology by varying the grain size and in turn calculate the Rayleigh number for respective mantle shell thickness to analyze the resulting convective patterns. For calculations with grain sizes of $5x10^{-4}$ m to $3x10^{-3}$ m, the viscosity of ice varies for each individual shell thickness. We use this range of grain sizes to identify the transition from conductive to convective solutions. When the calculations produce convective solutions we analyze the geoid, topography and heat flows to see if we can identify patterns characteristic of the depth of the mantle.

4.3.1 Critical Ice Shell Thickness and Critical Rayleigh Number

As previously discussed, varying the grain size between $5x10^{-4}$ to $3x10^{-3}$ m produce viscosities, which yield effective CitcomS Rayleigh numbers of $1.2x10^{5}$ and $3.0x10^{4}$. While the Rayleigh number in CitcomS is based on radius of the planet, we rescale and report Rayleigh numbers here using the thickness of the mantle as the characteristic length scale, which is the standard definition of the Rayleigh number. This facilitates comparison with previous studies of the onset of convection (*Chandrasekhar*, 1961; *Schubert et al.,* 2001). In Figure 4.3 we vary the grain size of ice and ice shell thickness based on the following equation,

$$d = \left(\frac{\rho g \alpha D^{\left(\frac{n+2}{n}\right)} \triangle T}{(\kappa A^{-1})^{\frac{1}{n}} \, exp\left(\frac{Q^*}{nRT_m}\right) Ra} \right)^{\frac{n}{p}} \tag{5}$$

We perform a series of calculations for mantle thickness of 112, 250 and 375 km to identify the transition from the conductive to convective solution (plusses and crosses) (Figure 4.3). We compare these results with the critical grain size as a function of critical Rayleigh number, based on *Barr et al.* (2004):

$$d_{crit} = \left(\frac{\rho g \alpha D^{\left(\frac{n+2}{n}\right)} \triangle T}{(\kappa A^{-1})^{\frac{1}{n}} \, exp\left(\frac{Q^*}{nRT_m}\right) Ra_{cr}} \right)^{\frac{n}{p}} \quad (6)$$

which is shown as a dark dotted line in Figure 4.3. This dotted line is based on the analytical solution of critical Rayleigh number calculations by *Solomatov* (1995). We have extrapolated a critical Rayleigh number based on previous calculations performed by *Solomatov* (1995) for grain boundary sliding. This curve puts the conductive solutions even higher than our model calculations for 250 km and 375 km shell thickness. For constant viscosity fluids, the critical Rayleigh number depends on shell thickness in a spherical shell (*Chandrasekhar*, 1961; *Schubert et al*., 2001). The light curve in Figure 4.3 is the best-fit critical Rayleigh value from our modeling calculations.

In our calculations, the thinner ice shell reaches a conductive state at smaller grain size (8×10^{-4} m) compared to a convective solution for the thicker ice shell at the same grain size. At higher Rayleigh numbers, calculations convect more vigorously and reach a steady state more quickly. As grain size increases, viscosity increases, which in turn decreases the Rayleigh number and the vigor of convection. We observe the difference in vigor of convection for varying ice shell thickness for the same grain sizes. For the thinnest ice shell thickness, lowering the Rayleigh number from 4.5×10^3 to 4.0×10^3 crosses the threshold where the solution becomes conductive. Similarly the critical Rayleigh number for the shell thickness of 250 km and 375 km the threshold is between 1.8×10^4 to 7.9×10^3 and 4.4×10^4 to 1.8×10^4 respectively (Table 4.3). Therefore the onset of convection, in the case of GBS, depends on both the critical grain size and the critical mantle shell thickness.

4.3.2 Radial Temperature and Velocity Profile

Radial temperature profiles for different grain sizes and shell thicknesses of 112, 250, and 375 km are shown in Figure 4.4. All of the models in this study reach a steady state. The temperature difference across the mantle is maintained at 50 K. The 375 km thick shell (Figure 4.4c) has a uniform-temperature, that extends from the surface to

almost 350 km depth, while the 112 km shell calculation (Figure 4.4a) has a thin, high-viscosity lithospheric lid that extends to approximately 25 km depth. While the thickest shell model appears to have no thermal boundary at the surface, this is in agreement with low Rayleigh calculation studies by *Ratcliffe et al.* (1996a). *Ratcliffe et al.* (1996a) show that there is clear thinning of the surface boundary layer for increasing Rayleigh number in a temperature-dependent viscosity calculation.

For the thickest shell model, at very low surface temperatures, there is a thick high-viscosity upper lid and the fluid behaves almost as a stagnant lid convection model. However, for warmer surface temperatures, the top thermal boundary layer to be affected by convective stresses and it behaves more like a mobile plate convection model, similar to Enceladus (*Barr*, 2008; *Castillo-Rogez and McCord*, 2010).

Radially averaged velocity profiles for the same calculations are shown in Figure 4.5. All the models have larger velocities near the core-mantle boundary while near the surface the velocities are smaller. The 112 km thick shell models (Figure 4.5a) have the largest velocities at the core mantle boundary, while the 375 km thick shell models have somewhat smaller values at the core mantle boundary. At the bottom 25 km of the mantle, i.e, closer to the core mantle boundary; there is a velocity kink, where the slope of the velocity curve increases as mantle shell thickness decreases. The average velocity decreases at depth decreases. As the calculations evolve, the average velocities near the surface decrease, as the shell thickness increases. The average surface velocity for the thinnest shell model is magnitudes higher than the thickest shell model. The high average velocities for a shell thickness of 112 km suggests that these calculations behave more like a mobile lid than stagnant lid convection. The low surface velocities for the thickest shell approach the stagnant lid regime, more like a transitional zone from mobile to stagnant, however these calculations are not stagnant lid because the average velocities are non-zero.

In the case of 112 km shell thickness, the difference in velocity between the surface and the core mantle boundary is comparatively small. These profiles are more similar to isoviscous convection than stagnant lid convection. As the shell thickness increases, the velocity of the surface relative to the interior decreases, reaching low

values of approximately 50 for the 375 km shell thickness models. For a grain size of $5x10^{-4}$ m, the velocity profile remains the same between the initial and final state for the 112 km shell thickness. For the same grain size, in the case of the 250 km thickness model, the difference between the velocity profile for the initial and final state varies significantly. The final state has slower velocities than the initial state. Holding the grain size constant, the maximum difference is observed between the initial and final velocity profile for the 375 km shell thickness model.

4.3.3 3D Structures

Figure 4.6 shows 3D isotherms from the steady-state convection with a 5×10^{-4} m grain size and varying mantle depths. The convective planforms differ significantly as the mantle thickness changes. We show both early and late stages of the models to illustrate that the solution evolve away from the spherical harmonic l=50 m=42 pattern quickly and that the initial condition is not controlling the results. Early time step corresponds to approximately 4.4 Ga and late time step corresponds to 1.0 Ga. The 112-km thick shell has a ridge-like pattern with many plumes along the ridge following the initial perturbation and maintains the multiple plumes (Figure 4.6a and Figure 4.6d). The 250-km thick mantle evolves from a similar multiple plumes structures (Figure 4.6b), in the absence of a ridge early on to a 5-plume structure (Figure 4.6e). The 375-km thick shell model evolves from a single plume with ridge structure early on (Figure 4.6c) to a degree-2 structure connected by a ridge (Figure 4.6f). The 375-km thick shell reaches steady-state stage early in the evolution of the model and the thermal structure remains unchanged after that. The transition from roll-like to plume like patterns as a function of shell thickness has been previously shown for thin silicate bodies (King, 2008; King, 2010). In our calculations, the transition from ridge structure to plume occurs when the shell thickness is between 130 km and 145 km. When we have an ice shell thickness of 130 km, there are isolated plumes but also many ridge structures. However, for a shell thickness of 145 km, plumes alone dominate the isothermal structure.

As we increase the grain size (Figure 4.7), the Rayleigh number decreases and convection becomes less vigorous. In the 112-km thick shell case, the grain size closest to

the critical curve, $6x10^{-4}$ m has similar ridge-like features early on (Figure 4.7a) that evolve to a similar plume like structure with lesser ridges (Figure 4.7d). For the 250-km shell structure, a large grain size of $1x10^{-3}$ m produces a multiple plumes structure with connecting ridges early on (Figure 4.7b). This evolves to a no ridge, multiple plume structure (Figure 4.7e). The grain size of $5x10^{-4}$ m and $1x10^{-3}$ m evolve to a similar low degree structure during its final stages. In the thickest shell model, for a larger grain size of $1x10^{-3}$ m we only observe a continuous ridge across the planet early in its evolution (Figure 4.7c). It evolves to a low degree structure, one prominent plume with a surrounding ridge structure (Figure 4.7f).

4.3.4 Geoid and Topography

Figure 4.8 and 4.9 shows the geoid and topography for early and late time steps for a single grain size of $5x10^{-4}$ m for 112, 250, and 375 km thick shells. For the thinnest shell (112 km), a grain size of $5x10^{-4}$ m produces a roll-like ridge structure with plumes in the temperature structure (Figure 4.6a and Figure 4.6d) and the roll-like pattern is observed in the geoid and topography (Figure 4.8a and Figure 4.8d). Early on, the geoid and topography highs correspond with the multiple plume structure along the ridge. The range of the topography is -5.5 m to 5.5 m and the geoid has a range of -2.5 m to 2 m. The geoid and topography are strongly correlated at early times (Figure 4.8a and Figure 4.8d) but less strongly correlated at steady state (Figure 4.9a and Figure 4.9d). At steady state, the geoid has three prominent highs of 4 m, which do not clearly correlate with the multiple plumes observed in the temperature structure. A -5 m trough is observed in the geoid at steady state, while the topography has several linear highs of 5.5 m that appear to be linear collections of plumes forming a long ridge. As we increase the grain size to $6x10^{-4}$ m, during the early stages (Figure 4.10a and Figure 4.10d), the ridge like structure remains the same with plumes along the ridge but there is also an increase in the number of isolated plumes. The geoid and topography remain correlated with one another. Being closer to the critical Rayleigh number, the contribution of mantle convection to the surface topography is smaller and has values of 4 m and lows of -5.0 m. For the same grain size and present day calculations (Figure 4.11a and Figure 4.11d), there is a strong correlation between geoid and topography highs. There are no ridge structures anymore

but a lot of isolated plumes that have a geoid and topography high of 4.4 m. The geoid lows of -4.5 m correspond with topography lows of -4.5 m. For a larger grain size of $8x10^{-4}$ m, the solution is conductive.

For a shell thickness of 250 km and a grain size of $5x10^{-4}$ m, during the early stages, there are two geoid highs of 2 m 180 degree away from each other with a couple of low –4 m trough structures (Figure 4.8b and Figure 4.8e). The topography highs of 4.5 m and low of -5.5 m co-relates with the geoid high and lows respectively. The geoid high in the southern hemisphere is more prominent than the corresponding topography high. The multiple plume structure correlates to the geoid and topography highs. For the late stages of the models (Figure 4.9b and Figure 4.9e), the geoid and topography have corresponding highs of 5.5 m and 7.5 m and lows of -3.5 m and -2.5 m that correspond to the 5-plume structure. Increasing the grain size to $1x10^{-3}$ m (Figure 4.10b and Figure 4.10e), leads to two prominent geoid highs with multiple highs in the geoid and topography across the equator and the geoid and topography are strongly correlated. Being closer to the critical convection curve, the topographic lows have smaller values of -2.5 m and 4.0 m. At steady-state (Figure 4.11b and Figure 4.11e), there are a number of isolated plumes with geoid high of 4.5 m and topography high of 4.4 m and a strong correlation between geoid and topography. Increasing the grain size to $3x10^{-3}$ m leads to a conductive solution.

In the case of the thickest shell of 375 km with a grain size of $5x10^{-4}$ m for an early time step (Figure 4.8c and Figure 4.8f), there is a general geoid and topographic high of 2 m and 4m respectively and a number of negative lows of -3.0 m and -4.5m respectively. The topography correlates with the geoid structure but the lows are much smaller in values. The plume head in the isothermal structure does correspond with the geoid and topography. During the late stage of the model (Figure 4.9c and Figure 4.9f), there are two prominent geoid highs of 3.0 m 180 degrees apart with two negative lows of -2.5 m between the two highs. The topography has two highs of 3 m that correspond with the geoid highs but there is a ridge that connects the two highs, corresponding to the 2-plume ridge-like isothermal structure. The topographic lows of -1.0 m are on the opposite sides of the ridge. Increasing the grain size to $1x10^{-3}$ m (Figure 4.10c and Figure

4.10f) we observe a prominent low-degree structure that corresponds to 2 broad topographic lows of -2.1 m. On the other hand, the geoid only contains one prominent low in the eastern hemisphere that corresponds to the topographic low in the same hemisphere. However, there is a geoid high in the western hemisphere that anti-correlates to the topography low. This solution is less convective than $5x10^{-4}$ m and much closer to the critical convective curve having much smaller values. At steady-state (Figure 4.11c and Figure 4.11f), the topography is exactly the same as the topography for $5x10^{-4}$ m; however, the geoid has two highs and broad one low compared to two highs and two lows for $5x10^{-4}$ m. Similar to the 250 km shell thickness model, increasing the grain size to $3x10^{-3}$ m leads to a conductive solution.

Interestingly, increasing the grain size to $1x10^{-3}$ m, for the thickest shell, leads to a low degree, small geoid and topography structure early on in the model compared to a much larger geoid and topography value, less prominent low degree structure for a grain size of $5x10^{-4}$ m.

4.4 Discussion

For most of our models, the geoid and topography are strongly correlated, much more for the early stages than the late stages of the model. For the late stage, in the case of a strong convecting mantle (grain size, $5x10^{-4}$m) for a shell thickness of 112 km, the geoid and topography do not completely correlate with each other, the geoid has three prominent highs and a low trough while the topography has many isolated highs and no clear trough. The geoid highs correlate with topography highs for both the 250 km and 375 km mantle shell thickness. However, the same cannot be said about the lows.

Varying shell thickness while holding grain size constant, the geoid and topography maxima increase with the thickest shell. As the models evolve, the geoid and topography values decrease relative to the early stages. The geoid and topography values decrease from the thinnest shell to the thickest shell model.

Ceres is mostly relaxed due to inadequate large-scale topographic structures on the surface (*Thomas et al.,* 2005; *Carry et al.,* 2008; *Castillo-Rogez and McCord*, 2010).

Due to the absence of large-scale topographic structures on the surface and resurfacing, we expect a low geoid and topography structure. Based on our modeling calculations, i.e, geoid and topography values for the thickest shell model, it seems unlikely that the mantle contains all the ice and silicate.

Isothermal structures vary from a ridge-like structure to a multiple plume structure to a low degree structure with changing shell thickness at the same grain size. There is a clear transition between the thin shell models, with roll-like structures in the geoid and topography and the thicker shell models with plume structures, consistent with the transition between roles and plumes seen in calculations for Mercury (*King,* 2008*; King,* 2010). While gravity models are often used in conjunction with moment of inertia to constrain internal structure (e.g., *Zuber et al.,* 2000; *Zuber*, 2001), our results provide a unique opportunity to constrain internal structure because the transition between roll-like structures and plume structures depends on shell thickness. Therefore, while the traditional observations of shape and moment of inertia from Dawn will be used to constrain internal structure of Ceres, the gravity field could provide a unique and independent constraint on the internal structure.

Previous studies on the asteroid Vesta by Dawn enabled calculations of mass, volume and gravitational field. Results show that Vesta's core has an average radius of 107 km to 113 km, suggesting the possibility of internal heat and differentiation of the planet (*Russell et al.,* 2012). Similar studies by Dawn will shed light on the internal structure of the dwarf planet. Dawn will determine the bulk density to better than 1% with accuracies near 0.1% (*Rayman et al.,* 2006). The current accuracy on the density of Ceres is about 2%, based on perturbations with neighboring asteroids (*Hilton*, 1999; *Konopliv et al.,* 2002). In addition, the gravity field will be studied with half a wavelength resolution ≤ 300 km (*Rayman et al.,* 2006). Surface maps with color filters will be obtained along with a topographic map covering more than 80% of the surface with a horizontal resolution ≤ 100m and a vertical resolution ≤ 10m. (*Rayman et al.,* 2006). One Dawn mission goal is to produce a global gravity field to the 5^{th} harmonic degree and order for Ceres (*Russell et al.,* 2007). We filtered our geoid results, for a convective grain size of $5x10^{-4}$ m, to degree and order 5 for gravity from Figure 4.9 and

show the results in Figure 4.12. At this low degree filtering, it is still unclear what kind of pattern the geoid holds for our models.

Recent activity could have removed the older craters (*Castillo-Rogez and McCord*, 2010) and the past history of the dwarf planet. Understanding the surface composition of the dwarf planet will be important to understand the internal structure and the presence of hydrothermal and geologic activity. Comparing our results and the data collected by Dawn would also help predict the thickness of the ice shell thickness and the composition of the mantle.

4.5 Conclusion

We investigate the dynamics of the interior of Ceres using calculations of spherical shell convection with a non-Newtonian rheology based on grain boundary sliding and find that the transition between convection and conduction occurs at ice crystal grain size of 8×10^{-4} m for the 112-km shell and 3×10^{-3} m for the two thicker shells. Our calculations are similar to the derivation of the critical grain-size by *Barr et al.* (2004). In the case of Ceres, convection will cease to exist for grain size greater than 3, i.e. $d_{critical} > 3$mm. Regardless of the mantle shell thickness, if the grain size is smaller than 8×10^{-4} m, we anticipate convection within the icy shell of Ceres has existed for a significant fraction of the age solar system and may exist at present. This provides a mechanism that explains the observations of hydrothermally altered minerals such as brucite and serpentine at the surface and may even provide a mechanism to explain recent observations of water vapor (*Kuppers et al.*, 2014) and the relaxed surface topography.

Our calculations show that the gravity field may provide an additional constraint on the internal structure of Ceres. If the silicate core is greater than 335 km, then we anticipate role-like structures and linear features in the geoid and topography, otherwise we expect plume-like structures that result in circular domes in the geoid and topography. The order of magnitude of the geoid anomalies in our calculations is small and based on the results of Vesta from Dawn, we anticipate that the gravitational potential field of Ceres should resolve features of this magnitude.

References

Barr, A. C., R. T. Pappalardo, and S. Zhong (2004), Convective instability in ice I with non-Newtonian rheology: Application to the icy Galilean satellites, *Journal of Geophysical Research* Vol 109, E12008.

Barr, A. C. (2008). Mobile lid convection beneath Enceladus' south polar terrain, *Journal of Geophysical Research* Vol. 113, E07009, doi:10.1029/2008JE003114.

Britt, D.T. and G.J. Consolmagno (2000). The porosity of dark meteorites and the structure of low-albedo asteroids. *Icarus*, Vol 146, 213–219.

Carry, B. et al (2008). Near-infrared mapping and physical properties of the dwarf-planet Ceres. *Astronomy and Astrophysics*, Vol 478, 235–244.

Castillo-Rogez, J.C and T.B. McCord (2010), Ceres' evolution and present state constrained by shape data. *Icarus,* Vol 205, 443-459.

Chandrasekhar. S (1961). Hydrodynamic and hydromagnetic stability.

Drummond, J. D et al. (1998). Icarus, Vol132, 80

Dumas, C. et al. (2003). Bulletin of the American Astronomical Society, 956

Durham,W. B., and L. A. Stern (2001), Rheological properties of water ice -Applications to satellites of the outer planets, *Annu. Rev. Earth Planet. Sci*., Vol. 29, 295– 330.

Fanale, F. and J.R. Salvail (1989). The water regime of Asteroid (1) Ceres. *Icarus,* Vol 82, 97– 110.

Ghosh, A. and H.Y. McSween (1998). A thermal model for the differentiation of Asteroid 4 Vesta, based on radiogenic heating. *Icarus* Vol 134, 187–206.

Goldsby, D. L., and D. L. Kohlstedt (2001), Superplastic deformation of ice: Experimental observations, J. Geophys. Res., 106, 11,017 – 11,030.

Gomes, R. et al (2005). Origin of the cataclysmic Late Heavy Bombardment period of the terrestrial planets. *Nature* Vol. 435, 466– 469.

Grimm, R.E. and H.Y. McSween (1989). Water and the thermal evolution of carbonaceous chondrite parent bodies. *Icarus,* Vol 82, 244–280.

Hilton, J.L. (1999). US Naval Observatory Ephemerides of the largest asteroids. *The Astronomical Journal,* Vol. 117, 1077.

Johnson, T.V. and F.P. Fanale (1973). Optical properties of carbonaceous chondrites and their relationship to asteroids, *Journal of Geophysical Research*, Vol 78, 8507–8578.

Jones, T. D. et al. (1990). *Icarus*, Vol 88, 172

King, S.D. (2008). Pattern of lobate scarps on Mercury's surface reproduced by a model of mantle convection. *Nature Geoscience,* Vol 1, 229 – 232.

King S.D. (2010). The Influence of core radius on the planform of stagnant lid convection. *Lunar and Planetary Science Conference (LPSC).*

Konopliv, A.S. et al (2002). A Global Solution for the Gravity Field, Rotation, Landmarks, and Ephemeris of Eros *Icarus,* Vol 160, 289–299.

Kovacevic, A. and M. Kuzmanoski (2007). Earth Moon and Planets, Vol. 100, 117.

Krasinsky, G.A et al (2002). Hidden mass in the Asteroid Belt. *Icarus* 158, 98–105.

Krot, A. N. et al (1999). Mineralogy, petrography, bulk chemical, iodine-xenon,and oxygen-isotopic compositions of dark inclusions in the reduced CV3 chondrite Efremovka, *Meteorit. Planet. Sci.,* Vol 34, 67– 90.

Kuppers, M., et al (2014). Localized sources of water vapour on the dwarf planet (1) Ceres, *Nature, 505,* 525-527.

Lebofsky, L. A. (1978), Asteroid 1 Ceres: Evidence for water of hydration, *Mon. Not. R. Astron. Soc*., Vol 182, 17– 21.

Lejeune, A.M. and P. Richet (1995). Rheology of crystal-bearing silicate melts: An experimental study at high viscosities. *Journal of Geophysical Research*. Vol 100, B3, 4215-4229.

Li, J.-Y. et al (2006). Photometric analysis of 1 Ceres and surface mapping from HST observations. *Icarus,* Vol 182, 143–160.

McCord, T.B. and C. Sotin (2005). Ceres: Evolution and current state. *Journal of Geophysical Research* Vol 110. E05009.

McCord, T.B., Castillo-Rogez. J. and A. Rivkin (2011). Ceres: Its Origin, Evolution and Structure and Dawn's Potential Contribution, *Space Sci Rev*, doi: 10.1007/s11214-010-9729-9.

McKinnon, W.B. (2008). Could Ceres be a refugee from the Kuiper Belt? In: *Asteroids, Comets, Meteors*, Baltimore, MD. LPI Contribution No. 1405, p. 8389.

Michalak, G. (2000), Determination of asteroid masses I. (1) Ceres, (2) Pallas and (4) Vesta, Astron. Astrophys, 360, 363– 374.

Milliken, R.E. and A.S. Rivkin (2009). Brucite and carbonate assemblages from alteration of olivine-rich materials on Ceres. *Nat. Geosci*. Vol 2, 258–261.

Millis, R.L. et al (1985). Observations of the Occultation of BD + 8°471 by Ceres. Presented at the 97th Annual Scientific and Membership Meeting of the Astronomical Society of the Pacific, June. Flagstaff, Arizona.

Mousis, O. and Y. Alibert (2005). Monthly Notices of the Royal Astronomical Society,

358, 188.

O'Brien, D.P. et al (2010). Early giant planet migration in the solar system: geochemical and cosmochemical implications for terrestrial planet formation.Bull. Am. Astron. Soc. 42, 948.

Parker, J.W et al (2006). Ceres: High-resolution imaging with HST and the determination of physical properties. Adv. Space Res. Vol 38, 2039–2042.

Pitjeva, E (2005). The dynamic estimation of the mass of the main asteroid belt, in Highlights of Astronomy, vol.13, ed. by O. Engvold. Presented at the XXVth General Assembly of the IAU—2003, Sydney, Australia, (Astronomical Society of the Pacific, San Francisco, 2005), pp. 772–773. ISBN 1-58381-086-2

Ratcliff, J.T., Schubert, G and A Zebib (1996a). Steady tetrahedral and cubic patterns of spherical shell convection with temperature-dependant viscosity. *Journal of Geophysical Research,* Vol 11, 25,473– 25,484.

Rayman, M.D et al (2006). Dawn:Amission in development for exploration of main belt asteroids Vesta and Ceres. *Acta Astronautica* Vol. 58, 605 – 616.

Rivkin, A.S., Volquardsen, E.L and B.E. Clark (2006). The surface composition of Ceres: Discovery of carbonates and iron-rich clays. *Icarus,* Vol 185, 563–567.

Rivkin, A.S. and E.L. Volquardsen (2008). Sitting around watching the world Ceres: A rotational study of the innermost dwarf planet. *LPS* Vol. 39, 1920.

Russell, C.T., et al (2007). Dawn Mission to Vesta and Ceres Symbiosis between Terrestrial Observations and Robotic Exploration. *Earth Moon Planet* Vol 101, 65–91.

Russell, C.T., et al. (2012). Dawn at Vesta: Testing the Protoplanetary Paradigm. *Science* Vol. 336, 684.

Sato, K., Miyamoto, M., and Zolensky, M. E. (1997). *Meteoritics and Planetary Science*, Vol. 32, 503

Schubert, G; Turcotte, D.L. and P Olson (2001). Mantle convection in the Earth and Planets.

Solomatov, V. S. (1995), Scaling of temperature- and stress-dependent viscosity convection, *Phys. Fluids*, Vol. 7, 266– 274.

Sotin, C., Grasset, O. and S. Beauchesne (1997), Thermodynamic properties of high pressure ices: Implications for the dynamics and internal structure of large icy satellites, in Solar System Ices, pp. 79– 96.

Srinivasan, G., Goswami, J. N. and N. Bhandari (1999), 26Al in eucrites Piplia Kalan: Plausible heat source and formation chronology, *Science*, 284, 1348–1350

Standish, E. M. (2001), JPL interoffice memorandum, 312, F-01-006, *Jet Propul. Lab*., Pasadena, Calif., 11 April.

Tan, E., Choi et al (2006) .Geo Framework: Coupling multiple models of mantle convection within a computational framework , *Geochemistry Geophysics Geosystems* 7 (6).

Thomas, C. et al (2005). Differentiation of the asteroid Ceres as revealed by its shape. *Nature* Vol. 437, 224–226.

Turrini, D., Magni, G. and A. Coradini (2009) Probing the history of Solar system through the cratering records on Vesta and Ceres. arXiv:0902.3579v1

Viateau, B., and M. Rapaport (1998), The mass of (1) Ceres from its gravitational perturbations on the orbits of 9 asteroids, *Astron. Astrophys*., Vol. 334, 729– 735.

Walsh, K.J. et al (2010). Origin of the Asteroid Belt and Mars' small mass. *Bull. Am. Astron. Soc*. Vol. 42, 947.

Wilson, L. et al (1999). Early aqueous alteration, explosive disruption, and re-processing of asteroids. *Meteorit. Planet. Sci*. Vol. 34, 541–557.

Zolotov, M.Yu. (2009). On the composition and differentiation of Ceres. *Icarus*. doi:10.1016/j.Icarus.2009.06.011.

Zhong, S. et al (2000). Role of temperature-dependent viscosity and surface plates in spherical shell models of mantle convection, *Journal of Geophysical Research*. Vol 105 (B5), 11063–11082.

Zhong, S. et al (2008). A benchmark study on mantle convection in a 3-D spherical shell using CitcomS, *Geochem.Geophys. Geosyst*., 9.

Zuber, M.T. (2001). The crust and mantle of Mars, *Nature*, Vol 412, 237-244.

Zuber, M.T. et al (2000). Internal structure and early thermal evolution of Mars from Mars Global surveyor topography and gravity. *Science* 287, 1788–1793.

Figures

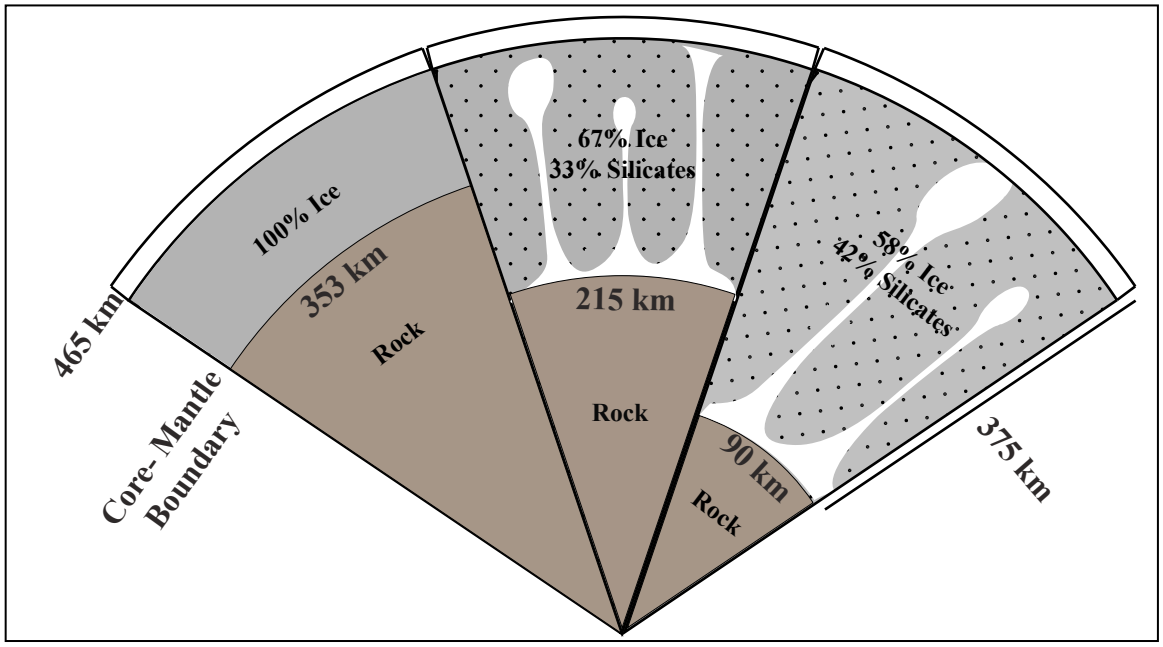

Figure 4.1 Different mantle shell thickness models with varying ratios of ice and silicate in the mantle.

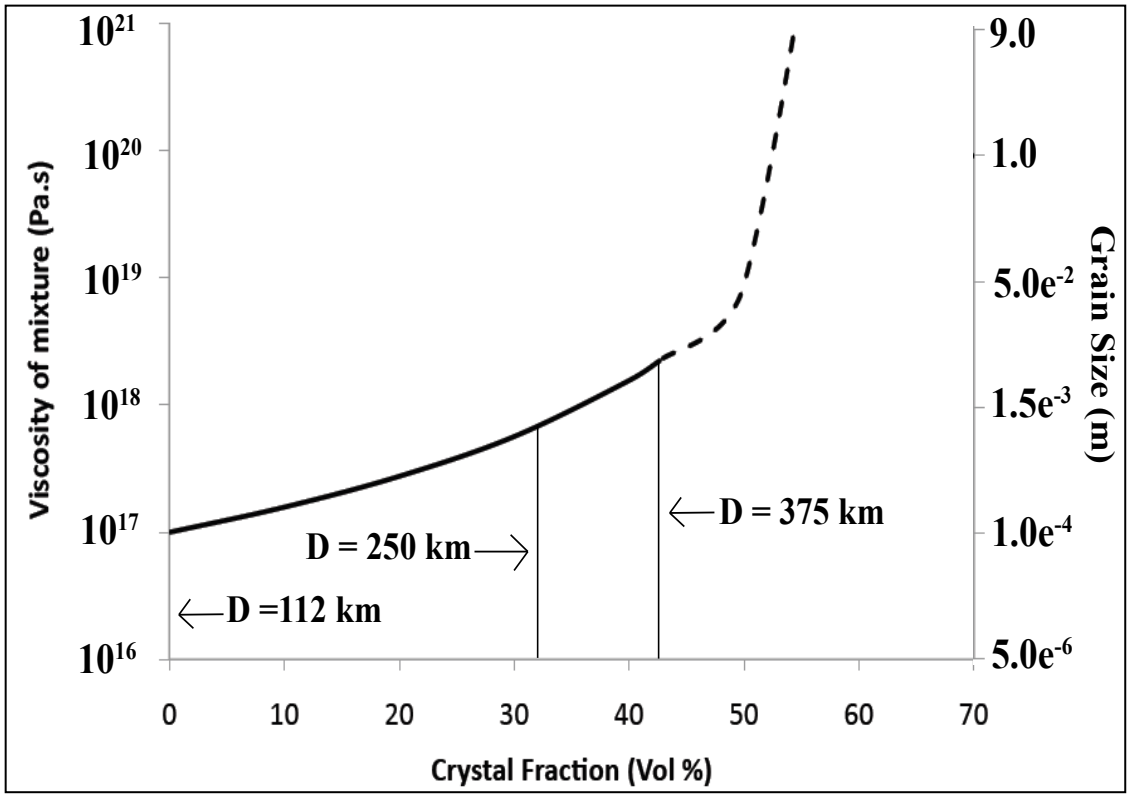

Figure 4.2 Viscosity of the ice-silicate mixture, following *LeJeune and Richet* (1995) viscosity law.

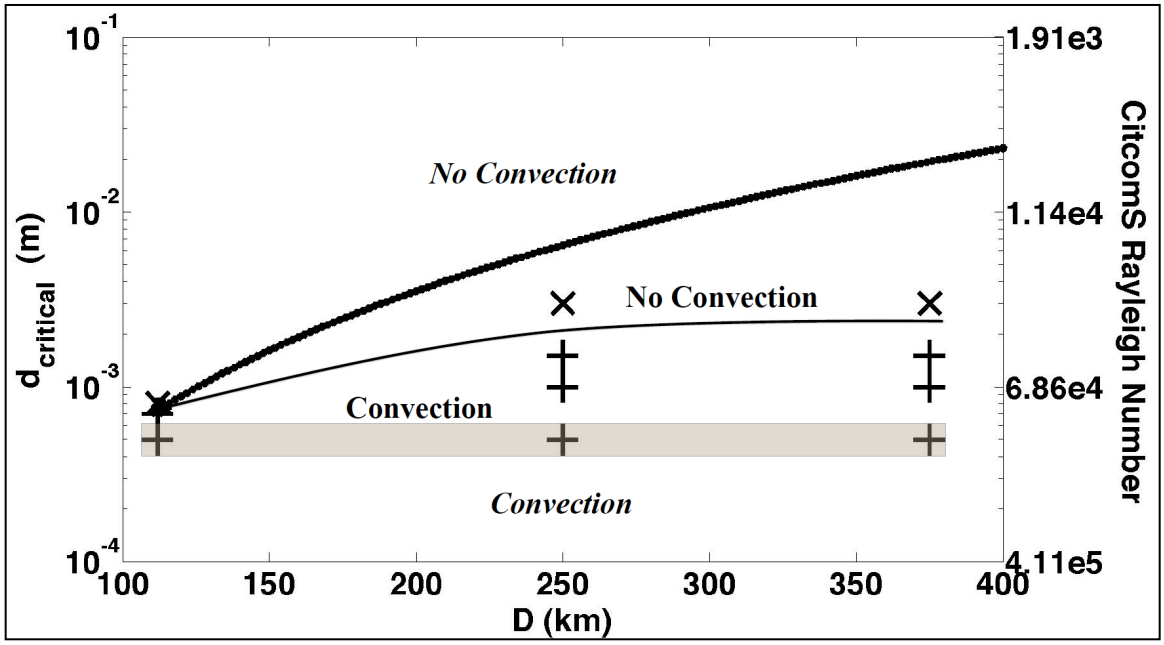

Figure 4.3 Critical grain size (Rayleigh number) versus mantle shell thickness. The Rayleigh number in this case is the CitcomS Rayleigh number. The analytical Rayleigh number is given in Table 4.3. The dark dotted line is the analytical solution of critical Rayleigh number based on the analysis of *Solomatov* (1995). The light curve is the best fit critical Rayleigh number based on our modeling calculations. The '+' are the convective models while 'x' are the conductive solutions. The shaded region is the region of consideration in this study. The "Convection" and "No Convection" solutions are based on our modeling calculations. The "*Convection"* and *"No Convection"* solutions are based on the extrapolation of *Solomatov* analytical work (1995).

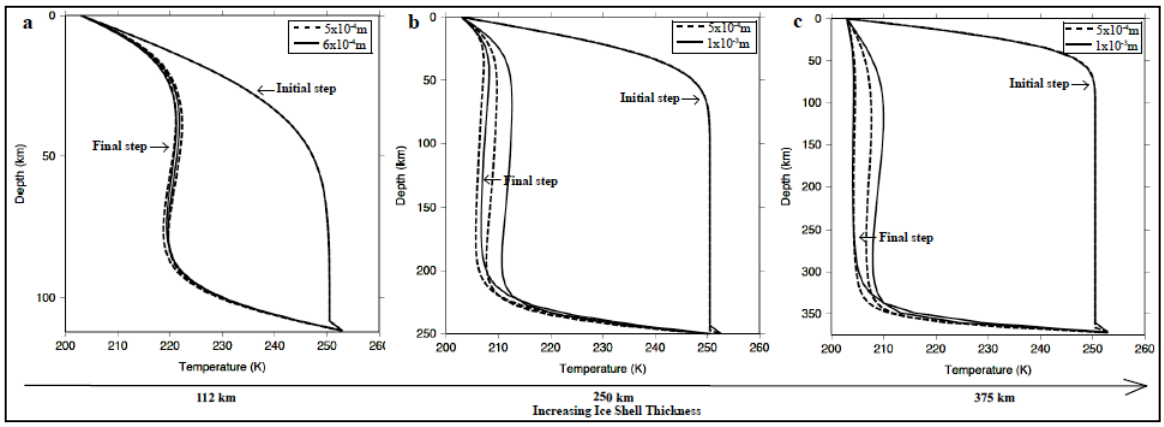

Figure 4.4 Radial temperature profiles for different grain sizes and different mantle shell thickness. The initial and final steps are shown for all the models.

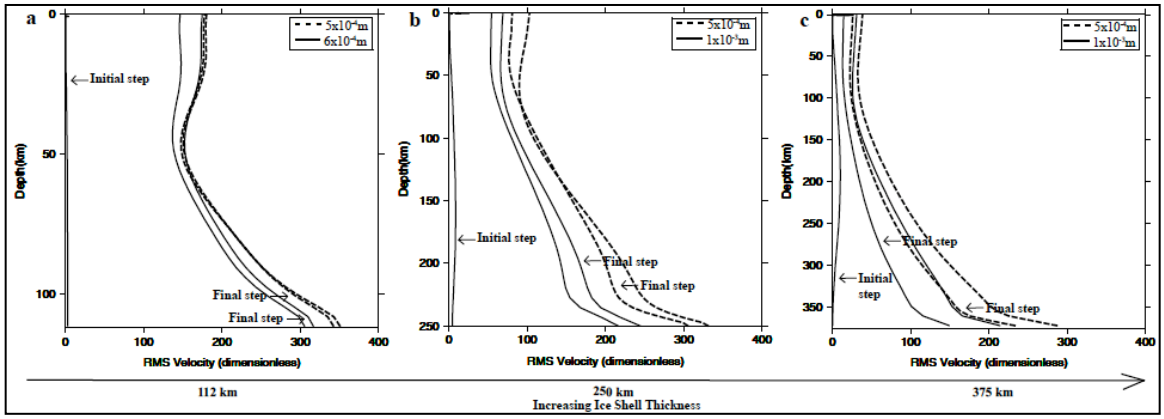

Figure 4.5 Velocity plots versus depth for different grain sizes and different mantle shell thickness. The initial and final steps are shown for all the models.

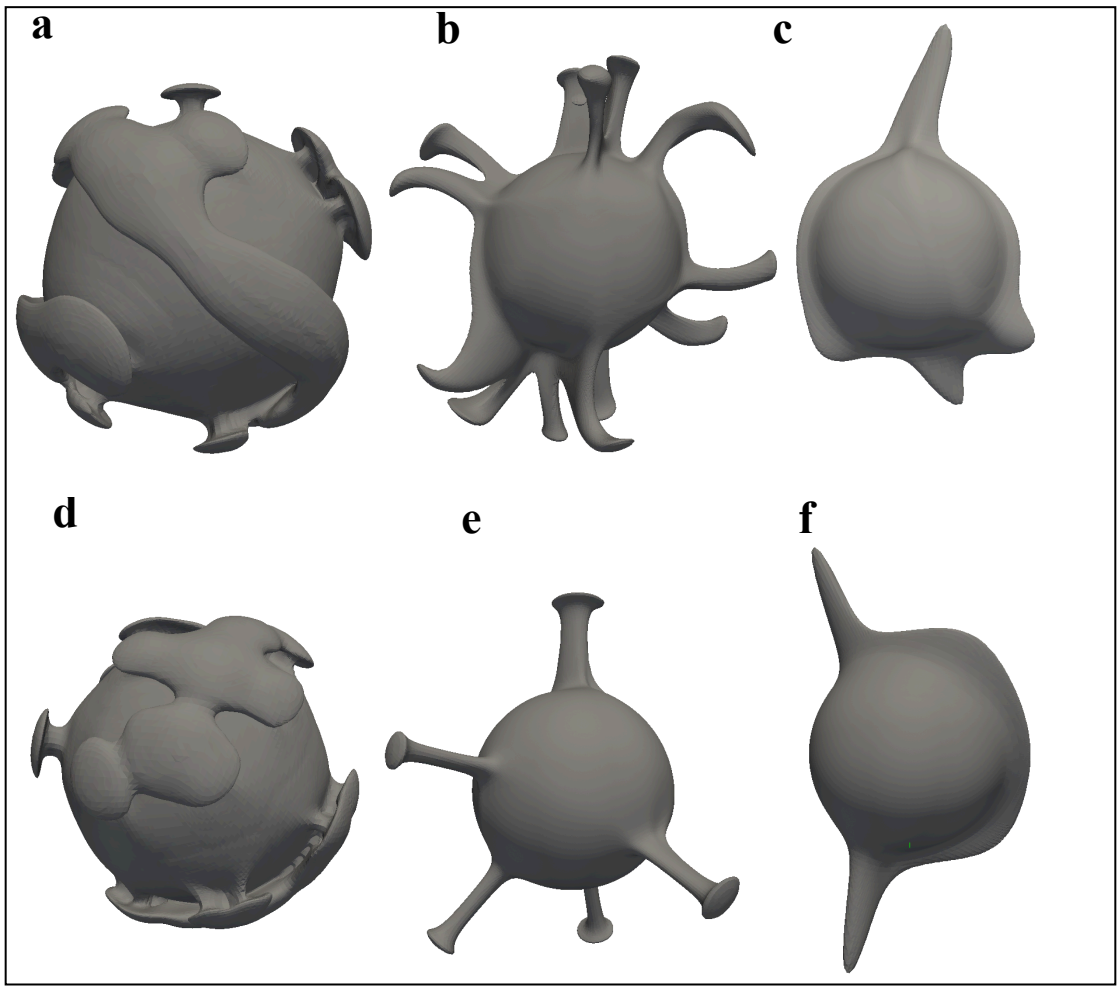

Figure 4.6 Early and Late stages for varying mantle shell thickness of 112 km, 250 km and 375 km for the same grain size of $5x10^{-4}$ m.

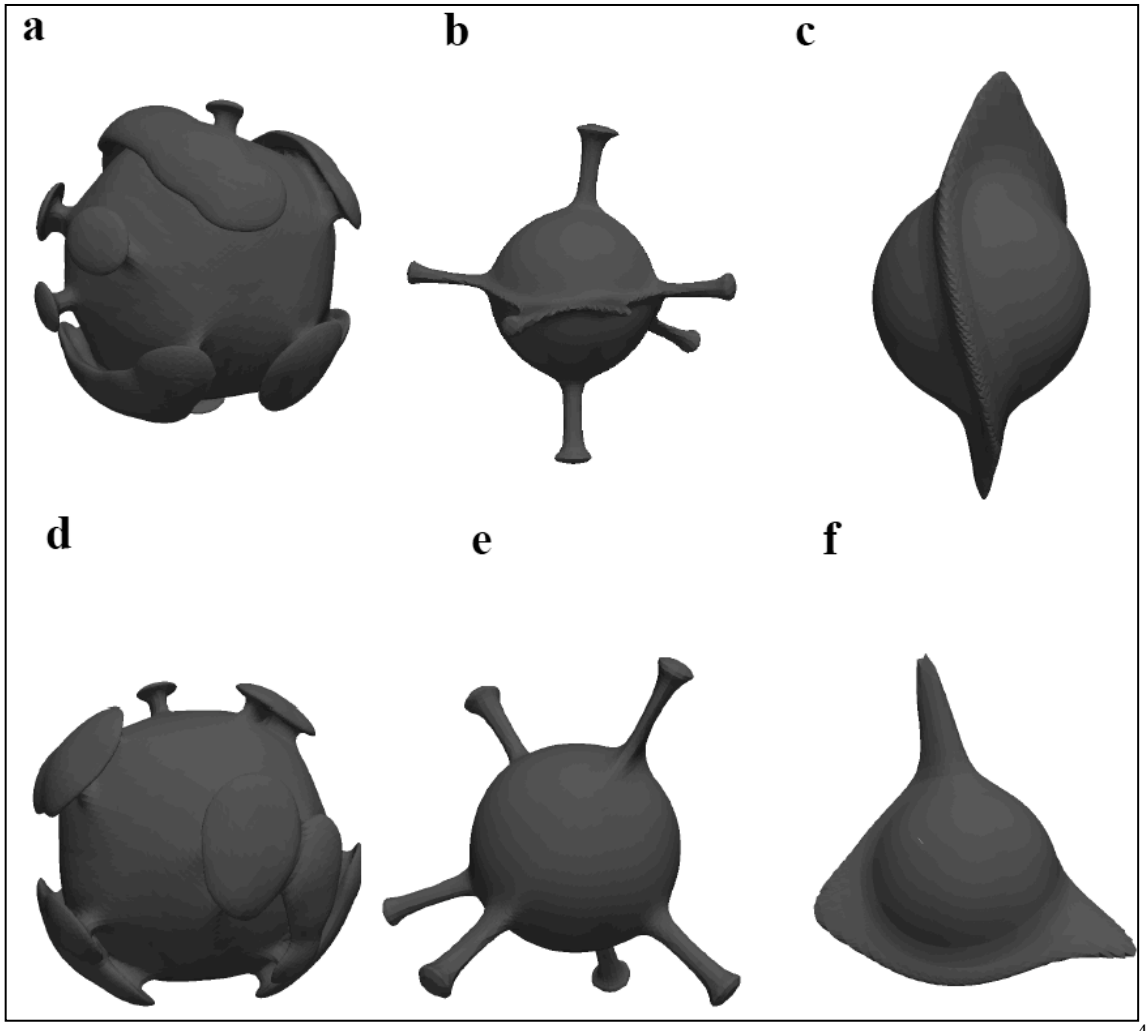

Figure 4.7 Early and Late stages for varying mantle shell thickness of 112 km ($6x10^{-4}$ m), 250 km ($1x10^{-3}$ m) and 375 km ($1x10^{-3}$ m).

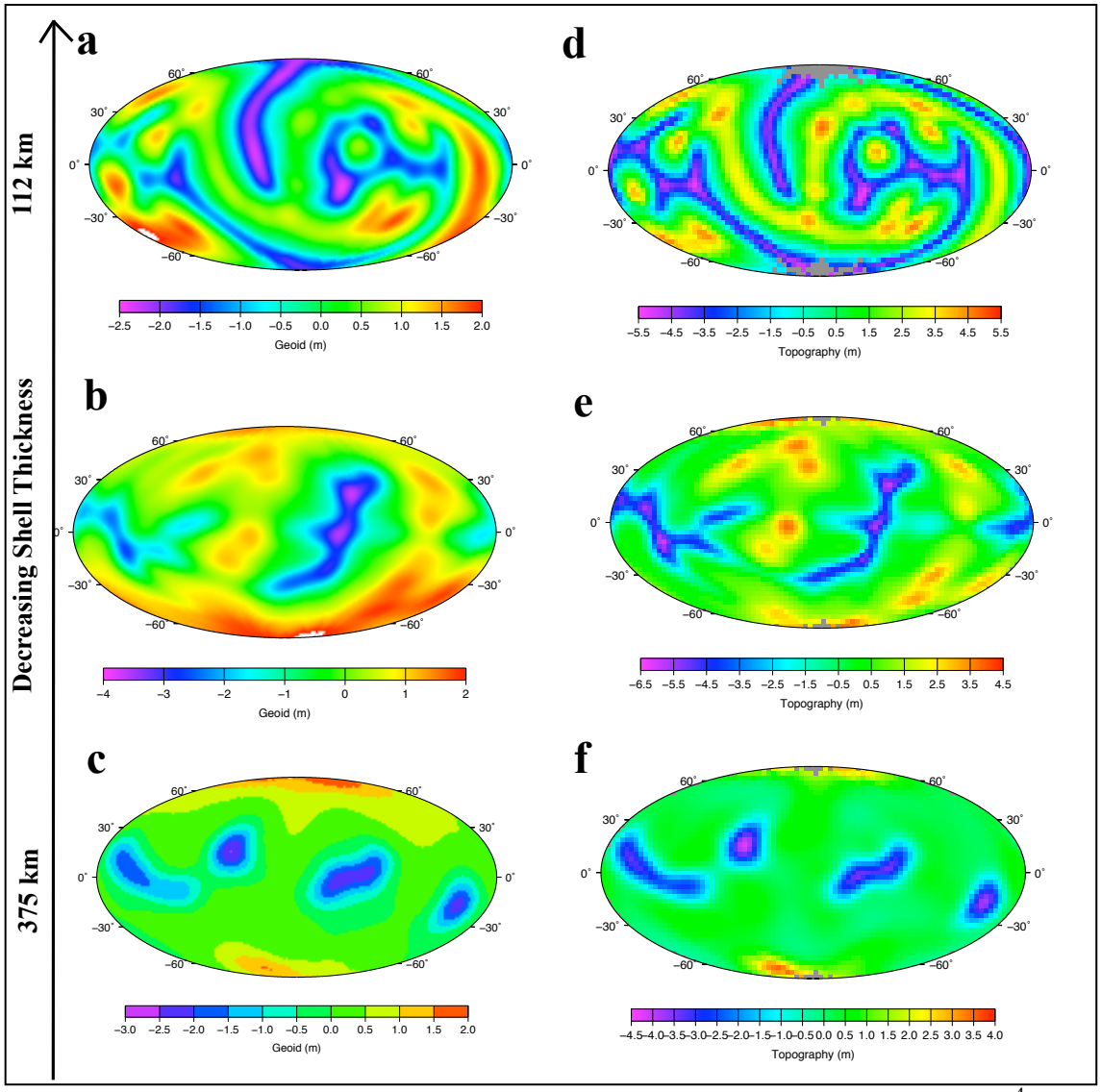

Figure 4.8 Early stages of the geoid and topography for the same grain size, $5x10^{-4}$ m but varying mantle shell thickness.

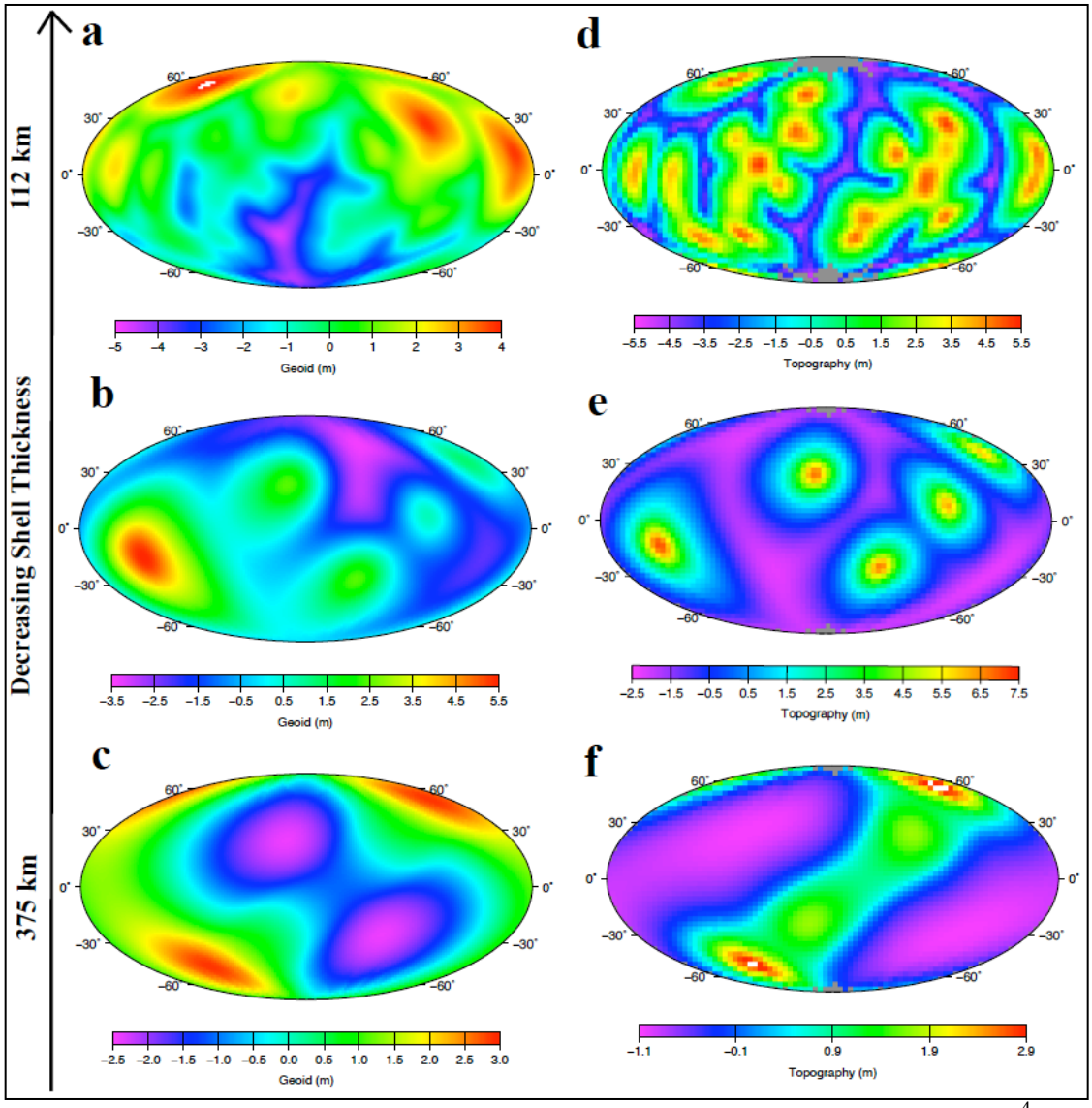

Figure 4.9 Late stages of the geoid and topography for the same grain size, $5x10^{-4}$ m but varying mantle shell thickness.

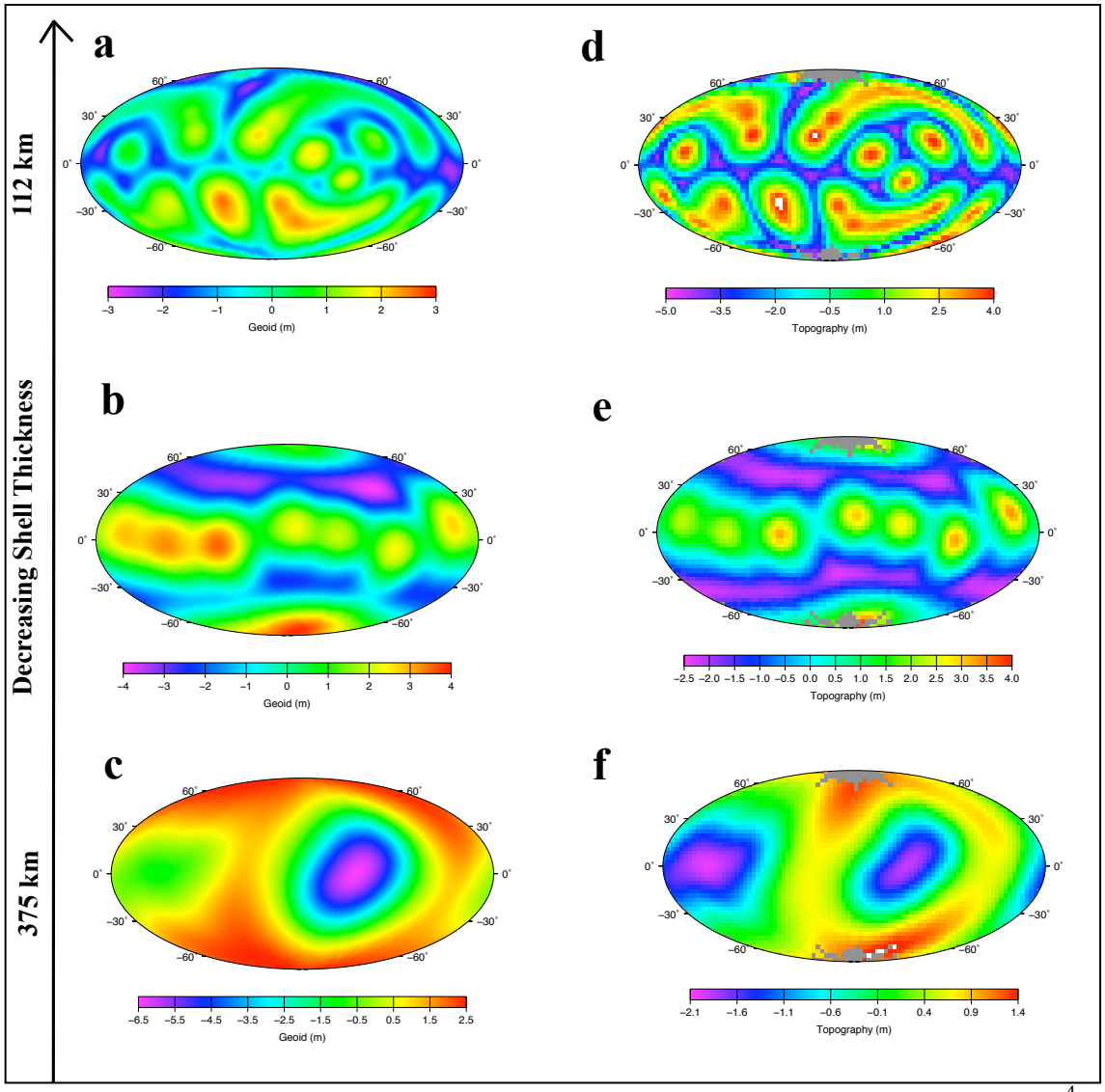

Figure 4.10 Early stages of the geoid and topography for the varying grain size, $6x10^{-4}$ m for 112 km shell thickness and $1x10^{-3}$ m for the remaining two shell thicknesses.

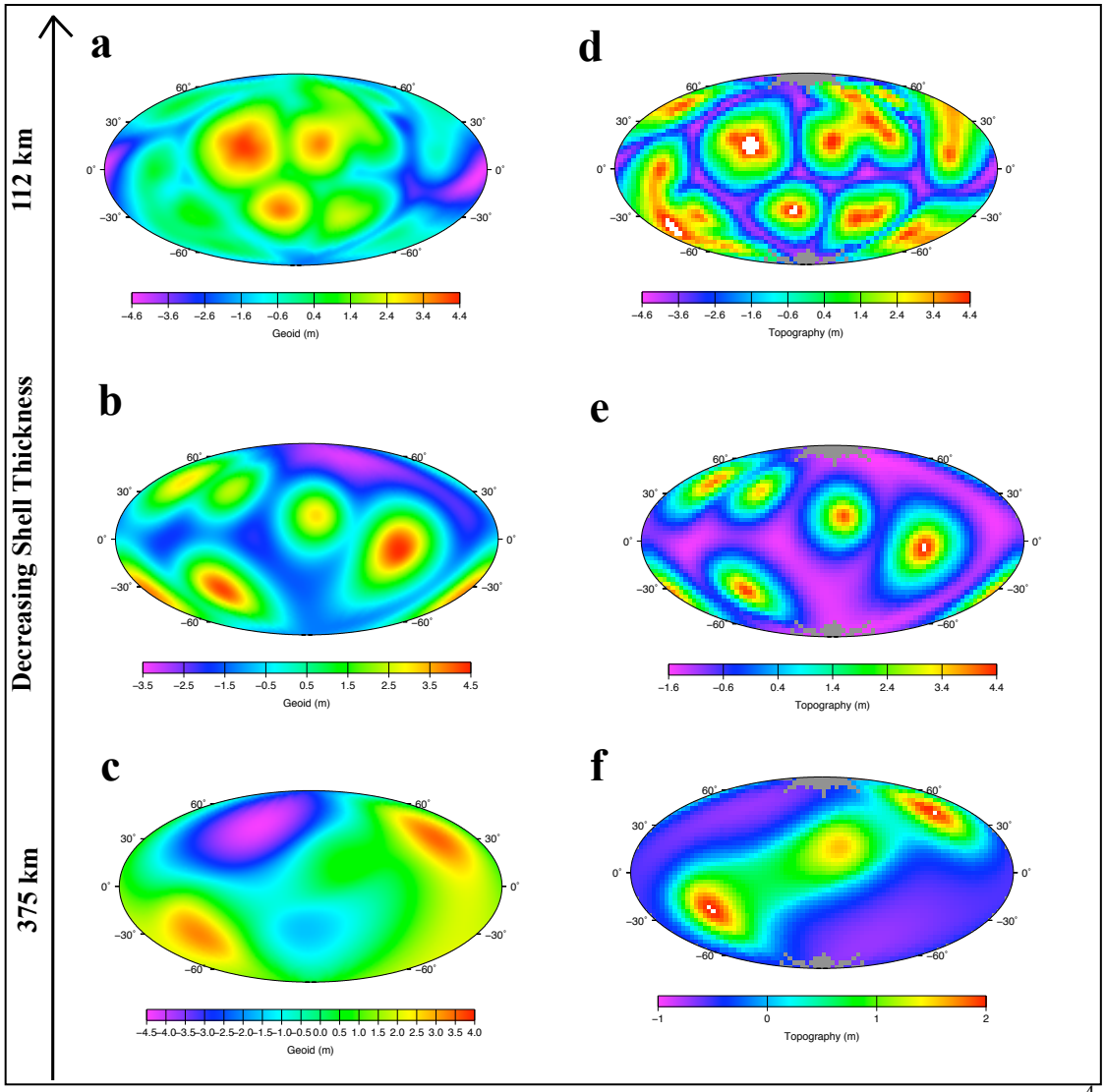

Figure 4.11 Late stages of the geoid and topography for the varying grain size, $6x10^{-4}$ m for 112 km shell thickness and $1x10^{-3}$ m for the remaining two shell thicknesses.

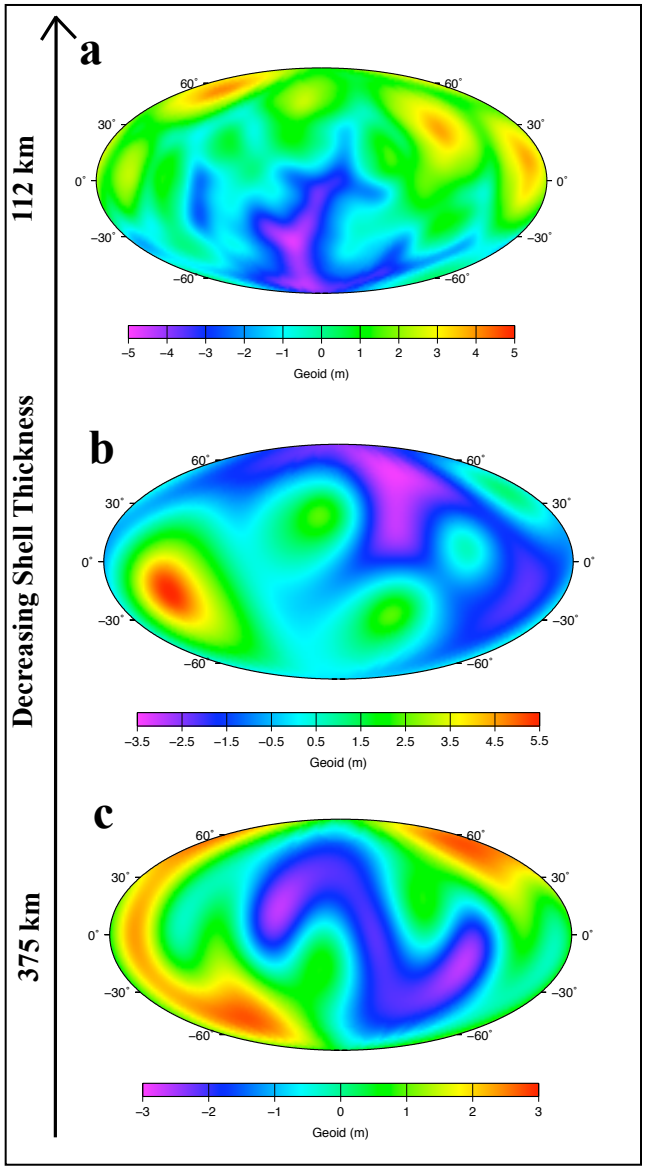

Figure 4.12 Late stages of the geoid and topography, only for a maximum degree and order of 5, for the same grain size, 5×10^{-4} m but varying mantle shell thickness.

Tables

Parameter	Symbol	Value
Pre exponential Parameter	A	$6.2 \times 10^{-14}\ m^{P}\ Pa^{-n}\ s^{-1}$
Stress component	n	1.8
Grain size exponent	p	1.4
Activation Energy	Q*	$49\ kJ\ mol^{-1}$
Universal Gas Constant	R	$8.3144\ J\ K^{-1}\ mol^{-1}$
Melting temperature of ice shell	T_m	273 K

Table 4.1 Rheological parameters for Grain Boundary Sliding

Parameter	Symbol	Value
Planetary radius	R_p	465×10^{3} m
Density of ice	ρ	$916.2\ kg\ m^{-3}$
Themal Diffusivity of ice	κ	$1.18 \times 10^{-6}\ m^{2}\ s^{-1}$
Gravitational Acceleration	g	$0.27\ m\ s^{-2}$
Specific heat of ice	C	$2050\ J\ K^{-1}\ kg^{-1}$
Thermal expansion co-efficient of ice	α	$5.0 \times 10^{-5}\ K^{-1}$
Surface Temperature	T_s	201 K
Adiabatic temperature difference across the mantle	ΔT	50 K

Table 4.2 Model Parameters

Mantle Shell Thickness (km)	Ice- Silicate Ratio (Mass percent)	Ice- Silicate Ratio (Volume percent)	Grain Size, d (m)	Viscosity η, (Pa.s)	Actual Ra
112	100-0	100-0	$^{\lozenge}5 \times 10^{-4}$ 6×10^{-4} $\ddagger 8 \times 10^{-4}$	$^{\lozenge}1.3 \times 10^{17}$ 1.5×10^{17} $\ddagger 1.8 \times 10^{17}$	$^{\lozenge}5.8 \times 10^{3}$ 5.0×10^{3} $\ddagger 4.0 \times 10^{3}$
250	43 -57	67 - 33	$^{\lozenge}5 \times 10^{-4}$ 8×10^{-4} 1×10^{-3} $\ddagger 3 \times 10^{-3}$	$^{\lozenge}2.6 \times 10^{17}$ 3.7×10^{17} 4.4×10^{17} $\ddagger 1.0 \times 10^{18}$	$^{\lozenge}3.2 \times 10^{4}$ 2.2×10^{4} 1.8×10^{4} $\ddagger 7.9 \times 10^{3}$
375	26-74	58 - 42	$^{\lozenge}5 \times 10^{-4}$ 8×10^{-4} 1×10^{-3} $\ddagger 3 \times 10^{-3}$	$^{\lozenge}3.7 \times 10^{17}$ 5.3×10^{17} 6.3×10^{17} $\ddagger 1.5 \times 10^{18}$	$^{\lozenge}7.5 \times 10^{4}$ 5.2×10^{4} 4.4×10^{4} $\ddagger 1.8 \times 10^{4}$

Table 4.3 Models with different grain sizes, viscosities and Rayleigh number for varying mantle shell thicknesses. $^{\lozenge}$Convective Solutions for the three different mantle shell thicknesses under consideration in this study. ‡Conductive Solutions

Chapter 5

Conclusion and Future Work

5.1 Conclusion

5.1.1 Melt Formulation

In this work, the production of a low degree-structure early on to explain the formation of Tharsis seems to be a challenge. Even if there is a low degree structure, melt is not necessarily produced on all plume heads. So, is the hypothesis that a low degree structure is required early on to create Tharsis and the crustal dichotomy a necessity? Magma overturn (*Elkins-Tanton et al.,* 2003, 2005) due to a stable stratified mantle could delay the instabilities formed at the core mantle boundary and this could inturn affect the convection planform and even the melt production.

In addition, none of the Mars models that produce abundant melt clearly support the formation of Tharsis. There are models that produce too much melt and some that do not produce enough. However, the melt formulation used in my Mars melting calculation is a simplified one. *Ruedas et al.* (2013a, 2013b) implemented a more complex melting model by integrating thermoelastic and petrological calculations into a compressive convection algorithm; the algorithm being previously implemented by *Tackley* (2008). It would be useful to revisit this problem with a more complicated melt formulation. It would be profitable to observe how the melt production changes based on a more complex melt formulation. Extraction of melt has been a known problem in these kinds of melt calculations. The pathway of melt and how much actually makes it to the surface is unknown and is beyond the scope of this work.

5.1.2 Kaula's Rule and Ensemble Averaging

For geoid and topography studies on Mars, the next step would be to run more models to cover the wide spectrum of different parameters. It will be interesting to see why Kaula's power rule is special and holds for some models and not others. Further

technique such as ensemble averaging will be studied. While the technique of ensemble averaging solutions has not been used previously in geodynamics, it has become fairly common in climate studies and weather forecasting (*Hagedorn et al.,* 2005). It will isolate the effect of each parameter on power spectrum calculations for geoid and topography. Ensemble Averaging can be used for better understanding of the parameters that contribute to the geoid and topography of the planet. It will eliminate uncertainties resulting from initial conditions, core radius and Rayleigh number. The next step would be to analyze the contribution of gravity from Moho and internal density, which has been difficult to resolve.

5.1.3 Grain Size of Ice-1 Rheology

My calculations provide information on the critical grain size of Ice-1 particles and the corresponding critical mantle shell thickness required for convection to occur. The grain size of ice particles for other icy bodies in the solar system, in order for convection to happen depends on the shell thickness. Grain sizes can very between 1mm and 10 cm for ice shells of large water ice satellites (*Barr and McKinnon,* 2007). It is interesting to note that a small body such as Ceres can sustain a convecting mantle. The different mantle shell thickness models produce ridge-like to plume-like shapes on the surface that is studied by geoid and topography calculations. Analysis of the gravity field to the 5th harmonic degree and order in my calculations, which is the maximum resolution anticipated by Dawn (*Russell et al.,* 2007) is the next step. However, based on Dawn's Vesta studies, a higher resolution of the gravity field is a possibility and our modeling technique will help in understanding Ceres.

5.2 Future work

Future missions to Mars and Ceres will definitely help pave the way for a much better understanding of the internal structure and surface features of the planet. On earth, seismic studies provide robust information about the internal structure and the composition of the planet. Unfortunately, on other planetary bodies such as Mars and Ceres, we do not have access to such data and hence geophysical modeling techniques are used to study the planet. Future NASA missions such as InSight (*Panning et al.,*

2012), a Discovery mission, proposes to use a broadband seismological probe to study Mars's interior. The data collected by such a mission will provide information on the composition and help constrain crustal thickness and even identify upper mantle discontinuities in the planet (*Panning et al.,* 2012).

In the case of Ceres, there is an ongoing mission, Dawn, which will provide information on gravity and shed more light on surface topography (*Rayman et al.,* 2006). The gravity and topography observations made by Dawn will help understand the surface and the shapes and structures can be related to our modeling studies. Even though Dawn is a space probe, studies on the moment of inertia will shed more light on the internal structure. Understanding the internal structure (i.e., differentiated or undifferentiated) will constrain future modeling studies. Therefore, planetary missions provide actual data and evidence that will support geophysical modeling and also help constrain future modeling techniques.

References

Barr, A. C. and W. B. McKinnon (2007), Convection in ice I shells and mantles with self-consistent grain size, *Journal of Geophysical Research,* Vol. 112, E02012, doi:10.1029/2006JE002781.

Elkins-Tanton, L. T., Parmentier, E.M. and P.C. Hess (2003). Magma ocean fractional crystallization and cumulate overturn in terrestrial planets: Implications for Mars, *Meteorit. Planet Sci.* Vol 38 (12), 1753–1771.

Elkins-Tanton, L. T., Hess, P.C., and E.M. Parmentier (2005). Possible formation of ancient crust on Mars through Magma Ocean processes, *Journal of Geophysical Research* Vol. 110.

Hagedorn, R., F. J. Doblas-Reyes and T. N. Palmer (2005) The rationale behind the success of multi-model ensembles in seasonal forecasting - 1. Basic concept, Tellus , 57A, 219-233.

Panning, P et al (2012). InSight: Single station broadband seismology for probing Mars' interior. *Lunar and Planetary Science Conference (LPSC).*

Rayman, M. D et al (2006). Dawn: A mission in development for exploration of main belt asteroids Vesta and Ceres. *Acta Astronautica* Vol 58. 605 – 616.

Ruedas, T., Tackley. P. J. and S.C. Solomon (2013a). Thermal and compositional evolution of the Martian mantle: Effects of water, *Phys. Earth Planet. Inter*. 220, 50-72, doi:10.1016/j.pepi.2013.04.006.

Ruedas, T., Tackley. P. J. and S.C. Solomon (2013b). Thermal and compositional evolution of the Martian mantle: Effects of phase transitions and melting, Phys. Earth Planet. Inter. 216, 32-58, doi:10.1016/j.pepi.2012.12.002

Russell, C.T., et al (2007). Dawn Mission to Vesta and Ceres Symbiosis between Terrestrial Observations and Robotic Exploration. *Earth Moon Planet* Vol 101:65–91.

Tackley, P.J. (2008). Modeling compressible mantle convection with large viscosity contrasts in a three-dimensional spherical shell using the yin-yang grid. *Phys. Earth Planet. Inter*. Vol 171, 7–18.

Appendix A

Advection_diffusion.c from CitcomS-3.1.1 is given below. The modified code is given in red. The comments are given in blue. The following are implemented in the modified code

1) Implementation of radiogenic elements and partitioning of radiogenic elements between the mantle and crust

2) Latent heat of melt

3) Core cooling

4) Melt calculation

```
/*
 *~~~~~~~~~~~~~~~~~~~~~~~~~~~~~~~~~~~~~~~~~~~~~~~~~~~~~~~~~~~~~~~~~~~~~~~~~~~~~~~~
 *
 *<LicenseText>
 *
 * CitcomS by Louis Moresi, Shijie Zhong, Lijie Han, Eh Tan,
 * Clint Conrad, Michael Gurnis, and Eun-seo Choi.
 * Copyright (C) 1994-2005, California Institute of Technology.
 *
 * This program is free software; you can redistribute it and/or modify
 * it under the terms of the GNU General Public License as published by
 * the Free Software Foundation; either version 2 of the License, or
 * (at your option) any later version.
 *
 * This program is distributed in the hope that it will be useful,
 * but WITHOUT ANY WARRANTY; without even the implied warranty of
 * MERCHANTABILITY or FITNESS FOR A PARTICULAR PURPOSE.  See the
 * GNU General Public License for more details.
 *
 * You should have received a copy of the GNU General Public License
 * along with this program; if not, write to the Free Software
 * Foundation, Inc., 59 Temple Place, Suite 330, Boston, MA  02111-1307  USA
 *
 *</LicenseText>
 *
 *~~~~~~~~~~~~~~~~~~~~~~~~~~~~~~~~~~~~~~~~~~~~~~~~~~~~~~~~~~~~~~~~~~~~~~~~~~~~~~~~
 */
/*   Functions which solve the heat transport equations using Petrov-Galerkin
     streamline-upwind methods. The process is basically as described in Alex
     Brooks PhD thesis (Caltech) which refers back to Hughes, Liu and Brooks.  */

#include <sys/types.h>

#include "element_definitions.h"
#include "global_defs.h"
#include <math.h>
#include "advection_diffusion.h"
#include "parsing.h"

static void set_diffusion_timestep(struct All_variables *E);
static void predictor(struct All_variables *E, double **field,
                      double **fielddot);
static void corrector(struct All_variables *E, double **field,
                      double **fielddot, double **Dfielddot);
static void pg_solver(struct All_variables *E,
                      double **T, double **Tdot, double **DTdot,
                      struct SOURCES *Q0,
                      double diff, int bc, unsigned int **FLAGS);
static void pg_shape_fn(struct All_variables *E, int el,
                        struct Shape_function *PG,
                        struct Shape_function_dx *GNx,
                        float VV[4][9], double rtf[4][9],
                        double diffusion, int m);
static double element_residual(struct All_variables *E, int el,
                               struct Shape_function *PG,
```

```
                              struct Shape_function_dx *GNx,
                              struct Shape_function_dA *dOmega,
                              float VV[4][9],
                              double **field, double **fielddot,
                              struct SOURCES *Q0,
                              double Eres[9], double rtf[4][9],
                              double diff, float **BC,
                              unsigned int **FLAGS, int m);
static void filter(struct All_variables *E);
static void process_heating(struct All_variables *E, int psc_pass_1);
int psc_pass;/*Global Variable*/


/* ============================================
   Generic adv-diffusion for temperature field.
   ============================================ */


/************************************************************/

void advection_diffusion_parameters(struct All_variables *E)
{

    /* Set intial values, defaults & read parameters*/
    int m=E->parallel.me;

    input_boolean("ADV",&(E->advection.ADVECTION),"on",m);
    input_boolean("filter_temp",&(E->advection.filter_temperature),"off",m);
    input_boolean("monitor_max_T",&(E->advection.monitor_max_T),"on",m);

    input_int("minstep",&(E->advection.min_timesteps),"1",m);
    input_int("maxstep",&(E->advection.max_timesteps),"1000",m);
    input_int("maxtotstep",&(E->advection.max_total_timesteps),"1000000",m);
    input_float("finetunedt",&(E->advection.fine_tune_dt),"0.9",m);
    input_float("fixed_timestep",&(E->advection.fixed_timestep),"0.0",m);
    input_float("adv_gamma",&(E->advection.gamma),"0.5",m);
    input_int("adv_sub_iterations",&(E->advection.temp_iterations),"2,1,nomax",m);

    input_float("inputdiffusivity",&(E->control.inputdiff),"1.0",m);


    return;
}


void advection_diffusion_allocate_memory(struct All_variables *E)
{
  int i,m;

  for(m=1;m<=E->sphere.caps_per_proc;m++)  {
    E->Tdot[m]= (double *)malloc((E->lmesh.nno+1)*sizeof(double));

    for(i=1;i<=E->lmesh.nno;i++)
      E->Tdot[m][i]=0.0;
    }
```

```
  return;
}


void PG_timestep_init(struct All_variables *E)
{

  set_diffusion_timestep(E);

  return;
}


void PG_timestep(struct All_variables *E)
{
    void std_timestep();
    void PG_timestep_solve();

    std_timestep(E);

    PG_timestep_solve(E);

    return;
}



/* ======================================================
   Obtain largest possible timestep (no melt considered)
   ======================================================  */


void std_timestep(struct All_variables *E)
{
    int i,d,n,nel,el,node,m;

    float global_fmin();
    void velo_from_element();

    float adv_timestep;
    float ts,uc1,uc2,uc3,uc,size,step,VV[4][9];

    const int dims=E->mesh.nsd;
    const int dofs=E->mesh.dof;
    const int nno=E->lmesh.nno;
    const int lev=E->mesh.levmax;
    const int ends=enodes[dims];
    const int sphere_key = 1;

    nel=E->lmesh.nel;

    if(E->advection.fixed_timestep != 0.0) {
      E->advection.timestep = E->advection.fixed_timestep;
      return;
```

```
    }

    adv_timestep = 1.0e8;
    for(m=1;m<=E->sphere.caps_per_proc;m++)
      for(el=1;el<=nel;el++) {

  velo_from_element(E,VV,m,el,sphere_key);

  uc=uc1=uc2=uc3=0.0;
  for(i=1;i<=ENODES3D;i++) {
    uc1 += E->N.ppt[GNPINDEX(i,1)]*VV[1][i];
    uc2 += E->N.ppt[GNPINDEX(i,1)]*VV[2][i];
    uc3 += E->N.ppt[GNPINDEX(i,1)]*VV[3][i];
        }
   uc = fabs(uc1)/E->eco[m][el].size[1] + fabs(uc2)/E->eco[m][el].size[2] + fabs(uc3)/E-
>eco[m][el].size[3];

  step = (0.5/uc);
  adv_timestep = min(adv_timestep,step);
      }

    adv_timestep = E->advection.dt_reduced * adv_timestep;

    adv_timestep = 1.0e-32 + min(E->advection.fine_tune_dt*adv_timestep,
        E->advection.diff_timestep);

    E->advection.timestep = global_fmin(E,adv_timestep);

/*     if (E->parallel.me==0) */
/*       fprintf(stderr, "adv_timestep=%g diff_timestep=%g\n",adv_timestep,E-
>advection.diff_timestep); */

    return;
}


void PG_timestep_solve(struct All_variables *E)
{

  double Tmaxd();
  void temperatures_conform_bcs();
  void lith_age_conform_tbc();
  void assimilate_lith_conform_bcs();
  int i,m,iredo;
  /*int psc_pass;*/
  double time0,time1,T_interior1;
  double *DTdot[NCS], *T1[NCS], *Tdot1[NCS];
  void cmb_temperature_bc();

  E->advection.timesteps++;

  for(m=1;m<=E->sphere.caps_per_proc;m++)
    DTdot[m]= (double *)malloc((E->lmesh.nno+1)*sizeof(double));
```

```
  if(E->advection.monitor_max_T) {
     for(m=1;m<=E->sphere.caps_per_proc;m++)  {
         T1[m]= (double *)malloc((E->lmesh.nno+1)*sizeof(double));
         Tdot1[m]= (double *)malloc((E->lmesh.nno+1)*sizeof(double));
     }

     for(m=1;m<=E->sphere.caps_per_proc;m++)
         for (i=1;i<=E->lmesh.nno;i++)   {
             T1[m][i] = E->T[m][i];
             Tdot1[m][i] = E->Tdot[m][i];
         }

     /* get the max temperature for old T */
     T_interior1 = Tmaxd(E,E->T);
  }

  E->advection.dt_reduced = 1.0;
  E->advection.last_sub_iterations = 1;


  do {
    E->advection.timestep *= E->advection.dt_reduced;

    iredo = 0;
    if (E->advection.ADVECTION) {

      predictor(E,E->T,E->Tdot);

      for(psc_pass=0;psc_pass<E->advection.temp_iterations;psc_pass++)   {
        /* adiabatic, dissipative and latent heating*/
        if(E->control.disptn_number != 0)
          process_heating(E, psc_pass);

        /* XXX: replace inputdiff with refstate.thermal_conductivity */
      pg_solver(E,E->T,E->Tdot,DTdot,&(E->convection.heat_sources),E->control.inputdiff,
1,E->node);
      corrector(E,E->T,E->Tdot,DTdot);
      temperatures_conform_bcs(E);
      }

      if(E->advection.monitor_max_T) {
          /* get the max temperature for new T */
          E->monitor.T_interior = Tmaxd(E,E->T);

          /* if the max temperature changes too much, restore the old
           * temperature field, calling the temperature solver using
           * half of the timestep size */
          if (E->monitor.T_interior/T_interior1 > E->monitor.T_maxvaried) {
              if(E->parallel.me==0) {
                  fprintf(stderr, "max T varied from %e to %e\n",
                          T_interior1, E->monitor.T_interior);
                  fprintf(E->fp, "max T varied from %e to %e\n",
                          T_interior1, E->monitor.T_interior);
              }
              for(m=1;m<=E->sphere.caps_per_proc;m++)
```

```
                for (i=1;i<=E->lmesh.nno;i++)   {
                    E->T[m][i] = T1[m][i];
                    E->Tdot[m][i] = Tdot1[m][i];
                }
            iredo = 1;
            E->advection.dt_reduced *= 0.5;
            E->advection.last_sub_iterations ++;
        }
      }
    }

  }  while ( iredo==1 && E->advection.last_sub_iterations <= 5);


  /* filter temperature to remove over-/under-shoot */
  if(E->advection.filter_temperature)
    filter(E);


  E->advection.total_timesteps++;
  E->monitor.elapsed_time += E->advection.timestep;

  if (E->advection.last_sub_iterations==5)
    E->control.keep_going = 0;

  for(m=1;m<=E->sphere.caps_per_proc;m++) {
    free((void *) DTdot[m] );
  }

  if(E->advection.monitor_max_T) {
      for(m=1;m<=E->sphere.caps_per_proc;m++) {
          free((void *) T1[m] );
          free((void *) Tdot1[m] );
      }
  }

  if(E->control.lith_age) {
      if(E->parallel.me==0) fprintf(stderr,"PG_timestep_solve\n");
      lith_age_conform_tbc(E);
      assimilate_lith_conform_bcs(E);
  }

    /*Added cmb boundary condition*/
    cmb_temperature_bc(E,&(E->convection.heat_sources));

  return;
}


/*********************************************************************/

static void set_diffusion_timestep(struct All_variables *E)
{
  float diff_timestep, ts;
  int m, el, d;
```

```
  float global_fmin();

  diff_timestep = 1.0e8;
  for(m=1;m<=E->sphere.caps_per_proc;m++)
    for(el=1;el<=E->lmesh.nel;el++)  {
      for(d=1;d<=E->mesh.nsd;d++)    {
     ts = E->eco[m][el].size[d] * E->eco[m][el].size[d];
     diff_timestep = min(diff_timestep,ts);
      }
    }

  diff_timestep = global_fmin(E,diff_timestep);
  E->advection.diff_timestep = 0.5 * diff_timestep;

  return;
}


/* ==============================
   predictor and corrector steps.
   ============================== */

static void predictor(struct All_variables *E, double **field,
                      double **fielddot)
{
  int node,m;
  double multiplier;

  multiplier = (1.0-E->advection.gamma) * E->advection.timestep;

  for (m=1;m<=E->sphere.caps_per_proc;m++)
    for(node=1;node<=E->lmesh.nno;node++)  {
      field[m][node] += multiplier * fielddot[m][node] ;
      fielddot[m][node] = 0.0;
    }

  return;
}


static void corrector(struct All_variables *E, double **field,
                      double **fielddot, double **Dfielddot)
{
  int node,m;
  double multiplier;

  multiplier = E->advection.gamma * E->advection.timestep;

  for (m=1;m<=E->sphere.caps_per_proc;m++)
    for(node=1;node<=E->lmesh.nno;node++) {
      field[m][node] += multiplier * Dfielddot[m][node];
      fielddot[m][node] +=  Dfielddot[m][node];
    }
```

```
  return;
}


/* ================================================
   The solution step -- determine residual vector from
   advective-diffusive terms and solve for delta Tdot
   Two versions are available -- one for Cray-style
   vector optimizations etc and one optimized for
   workstations.
   ================================================ */


static void pg_solver(struct All_variables *E,
                      double **T, double **Tdot, double **DTdot,
                      struct SOURCES *Q0,
                      double diff, int bc, unsigned int **FLAGS)
{
    void get_rtf_at_vpts();
    void velo_from_element();

    int el,e,a,i,a1,m;
    double Eres[9],rtf[4][9];  /* correction to the (scalar) Tdot field */
    double Qtotal, element_melt, total_melt, global_melt, time, time_original, Time;
    double timediff,rate_melting;
    float VV[4][9];

    struct Shape_function PG;

    const int dims=E->mesh.nsd;
    const int dofs=E->mesh.dof;
    const int ends=enodes[dims];
    const int sphere_key = 1;
    const int lev=E->mesh.levmax;

    total_melt=0.0;
    global_melt = 0.0;
    element_melt = 0.0;
    rate_melting = 0.0;

    for (m=1;m<=E->sphere.caps_per_proc;m++)
      for(i=1;i<=E->lmesh.nno;i++)
      DTdot[m][i] = 0.0;

    for (m=1;m<=E->sphere.caps_per_proc;m++)
       for(el=1;el<=E->lmesh.nel;el++)    {

          velo_from_element(E,VV,m,el,sphere_key);

          get_rtf_at_vpts(E, m, lev, el, rtf);

          /* XXX: replace diff with refstate.thermal_conductivity */
          pg_shape_fn(E, el, &PG, &(E->gNX[m][el]), VV,
                      rtf, diff, m);
          element_melt = element_residual(E, el, &PG, &(E->gNX[m][el]), &(E->gDA[m][el]),
```

```
                        VV, T, Tdot,
                        Q0, Eres, rtf, diff, E->sphere.cap[m].TB,
                        FLAGS, m);

          total_melt += element_melt;

        for(a=1;a<=ends;a++) {
        a1 = E->ien[m][el].node[a];
        DTdot[m][a1] += Eres[a];
           }

        } /* next element */

        /* sum up for all processors - Latent heat*/
        MPI_Allreduce(&total_melt, &global_melt, 1,
                      MPI_DOUBLE, MPI_SUM, E->parallel.world);

        time_original = 4.3e9;/*We are using a older lithosphere of 250 instead of 50*/
        time = (1.71e11*(E->monitor.elapsed_time+Q0->t_offset));
        Time = time_original - time;
        timediff = (1.71e11*E->advection.timestep); /*Difference in time step in years*/
        rate_melting = global_melt/timediff;

        if (psc_pass == 0){
        if(E->parallel.me == 0) {
          fprintf(stdout,"%e %e %e\n", Time, global_melt, rate_melting);
          }
         }

    (E->exchange_node_d)(E,DTdot,lev);

    for (m=1;m<=E->sphere.caps_per_proc;m++)
      for(i=1;i<=E->lmesh.nno;i++) {
        if(!(E->node[m][i] & (TBX | TBY | TBZ))){
    DTdot[m][i] *= E->TMass[m][i];         /* lumped mass matrix */
  } else
    DTdot[m][i] = 0.0;         /* lumped mass matrix */
      }

    return;
}



/* ==================================================
   Petrov-Galerkin shape functions for a given element
   ================================================== */

static void pg_shape_fn(struct All_variables *E, int el,
                        struct Shape_function *PG,
                        struct Shape_function_dx *GNx,
                        float VV[4][9], double rtf[4][9],
                        double diffusion, int m)
{
    int i,j;
```

```
    int *ienm;

    double uc1,uc2,uc3;
    double u1,u2,u3,sint[9];
    double uxse,ueta,ufai,xse,eta,fai,adiff;

    double prod1,unorm,twodiff;

    ienm=E->ien[m][el].node;

    twodiff = 2.0*diffusion;

    uc1 =  uc2 = uc3 = 0.0;

    for(i=1;i<=ENODES3D;i++) {
      uc1 +=  E->N.ppt[GNPINDEX(i,1)]*VV[1][i];
      uc2 +=  E->N.ppt[GNPINDEX(i,1)]*VV[2][i];
      uc3 +=  E->N.ppt[GNPINDEX(i,1)]*VV[3][i];
      }

    uxse = fabs(uc1*E->eco[m][el].size[1]);
    ueta = fabs(uc2*E->eco[m][el].size[2]);
    ufai = fabs(uc3*E->eco[m][el].size[3]);

    xse = (uxse>twodiff)? (1.0-twodiff/uxse):0.0;
    eta = (ueta>twodiff)? (1.0-twodiff/ueta):0.0;
    fai = (ufai>twodiff)? (1.0-twodiff/ufai):0.0;


    unorm = uc1*uc1 + uc2*uc2 + uc3*uc3;

    adiff = (unorm>0.000001)?( (uxse*xse+ueta*eta+ufai*fai)/(2.0*unorm) ):0.0;

    for(i=1;i<=VPOINTS3D;i++)
       sint[i] = rtf[3][i]/sin(rtf[1][i]);

    for(i=1;i<=VPOINTS3D;i++) {
       u1 = u2 = u3 = 0.0;
       for(j=1;j<=ENODES3D;j++)  /* this line heavily used */ {
       u1 += VV[1][j] * E->N.vpt[GNVINDEX(j,i)];
       u2 += VV[2][j] * E->N.vpt[GNVINDEX(j,i)];
       u3 += VV[3][j] * E->N.vpt[GNVINDEX(j,i)];
      }

       for(j=1;j<=ENODES3D;j++) {
            prod1 = (u1 * GNx->vpt[GNVXINDEX(0,j,i)]*rtf[3][i] +
                     u2 * GNx->vpt[GNVXINDEX(1,j,i)]*sint[i] +
                     u3 * GNx->vpt[GNVXINDEX(2,j,i)] ) ;

      PG->vpt[GNVINDEX(j,i)] = E->N.vpt[GNVINDEX(j,i)] + adiff * prod1;
         }
       }

   return;
}
```

```
/* ========================================
   Residual force vector from heat-transport.
   Used to correct the Tdot term.
   ========================================  */

static double element_residual(struct All_variables *E, int el,
                               struct Shape_function *PG,
                               struct Shape_function_dx *GNx,
                               struct Shape_function_dA *dOmega,
                               float VV[4][9],
                               double **field, double **fielddot,
                               struct SOURCES *Q0,
                               double Eres[9], double rtf[4][9],
                               double diff, float **BC,
                               unsigned int **FLAGS, int m)
{
    int i,j,a,k,node,nodes[5],d,aid,back_front,onedfns;
    /*double Q;*/
    double Q[4];
    double Qtotal;
    double dT[9];
    double T_intp[9],Radius[9],Radius_intp[9];
    double R;
    double tx1[9],tx2[9],tx3[9],sint[9];
    double v1[9],v2[9],v3[9];
    double adv_dT,t2[4];
    double T,DT;
    double element_melt,deltat;
    double total_melt, time, time_original, Time;
    double Cu238,Cu235,Ct232,Ck,Hu238,Hu235,Ht232,Hk,toe_u238,toe_u235,toe_t232,toe_k,ln2;
    double lambda[4];
    float meltrate[9];

    /*Latent heat*/
    double L_H,La_he[9],Lat_hea[9],Late_heat[9];
    float GRAV,surface_rad,nondim_radius,dim_depth,Pressure;
    float temp_nd,surf_temperature,superadiabatic_tempdiff,adiabatic_gradient,
    float Temperature1,Temperature2,Temperature;
    float P3,P2,P1,A1,B1,C1,D1,Tmelt,Melt[9];
    float marsrho;

    double prod,sfn;
    struct Shape_function1 GM;
    struct Shape_function1_dA dGamma;
    double temp,rho,cp,heating,total_heating,crust_heating;
    double mytime,mytime_original;
    double Internal_heat,depth,Vmc,Vm,Vc;
    int nz;

    void get_global_1d_shape_fn();

    const int dims=E->mesh.nsd;
```

```
const int dofs=E->mesh.dof;
const int nno=E->lmesh.nno;
const int lev=E->mesh.levmax;
const int ends=enodes[dims];
const int vpts=vpoints[dims];
const int diffusion = (diff != 0.0);

for(i=1;i<=vpts;i++) {
  dT[i]=0.0;
  T_intp[i]=0.0;
  Radius[i] = 0.0;
  Radius_intp[i]=0.0;
  v1[i] = tx1[i]=  0.0;
  v2[i] = tx2[i]=  0.0;
  v3[i] = tx3[i]=  0.0;
  }

for(i=1;i<=vpts;i++)
    sint[i] = rtf[3][i]/sin(rtf[1][i]);

for(j=1;j<=ends;j++)       {
  node = E->ien[m][el].node[j];
  T = field[m][node];
  if(E->node[m][node] & (TBX | TBY | TBZ))
  DT=0.0;
  else
  DT = fielddot[m][node];

  for(i=1;i<=vpts;i++)  {
      dT[i] += DT * E->N.vpt[GNVINDEX(j,i)];
      tx1[i] += GNx->vpt[GNVXINDEX(0,j,i)] * T * rtf[3][i];
      tx2[i] += GNx->vpt[GNVXINDEX(1,j,i)] * T * sint[i];
      tx3[i] += GNx->vpt[GNVXINDEX(2,j,i)] * T;
      sfn = E->N.vpt[GNVINDEX(j,i)];
      v1[i] += VV[1][j] * sfn;
      v2[i] += VV[2][j] * sfn;
      v3[i] += VV[3][j] * sfn;
  }
}

     /*These are values for Mars - Lodders and Fegley (decaying heat sources)*/
     Cu238=1.6e-8;
     Cu235=1.6e-8;
     Ct232=5.6e-8;
     Ck=9.2e-4;
     Hu238=9.46e-5;
     Hu235=5.69e-4;
     Ht232=2.64e-5;
     Hk=2.92e-5;
     toe_u238=4.47e9;
     toe_u235=7.04e8;
     toe_t232=1.40e10;
     toe_k=1.25e9;
     ln2=0.69314718;
```

```
          /*Density of Mars mantle*/
          marsrho=3.400e3;

          Q[0]=(0.9928*Cu238*Hu238);
          Q[1]=(0.0071*Cu235*Hu235);
          Q[2]=(Ct232*Ht232);
          Q[3]=(1.19e-4*Ck*Hk);

          lambda[0]=ln2/toe_u238;
          lambda[1]=ln2/toe_u235;
          lambda[2]=ln2/toe_t232;
          lambda[3]=ln2/toe_k;

          /*My change to the time to make it a non-dimensional value*/
          mytime_original = 4.3e9;/*We are using a older lithosphere of 250 instead of 50*/
          /*To convert to dimentional time*/
          mytime=(1.71e11*(E->monitor.elapsed_time+Q0->t_offset));

          Qtotal=0.0;
          for(i=0;i<4;i++)
          {
          Qtotal+=Q[i] * exp(lambda[i] * (mytime_original-mytime));
          }

/*    Q=0.0;
    for(i=0;i<Q0.number;i++)
    Q += Q0->Q[i] * exp(-Q0->lambda[i] * (E->monitor.elapsed_time+Q0->t_offset));
*/

    /* heat production */
    /*Q = E->control.Q0;undo*/

    /* should we add a compositional contribution? */
    /*if(E->control.tracer_enriched){undo*/
      /* XXX: change Q and Q0 to be a vector of ncomp elements */

      /* Q = Q0 for C = 0, Q = Q0ER for C = 1, and linearly in
   between  */
      /*Q *= (1.0 - E->composition.comp_el[m][0][el]);
      Q += E->composition.comp_el[m][0][el] * E->control.Q0ER;
    }*/

    nz = ((el-1) % E->lmesh.elz) + 1;
    rho = 0.5 * (E->refstate.rho[nz] + E->refstate.rho[nz+1]);
    cp = 0.5 * (E->refstate.heat_capacity[nz] + E->refstate.heat_capacity[nz+1]);

    /*if(E->control.disptn_number == 0)
        heating = rho * Q;
    else undo*/
        /* E->heating_latent is actually the inverse of latent heating */
        /*heating = (rho * Q - E->heating_adi[m][el] + E->heating_visc[m][el])
            * E->heating_latent[m][el];undo*/

     Internal_heat = (marsrho * Qtotal);
     total_heating =(Internal_heat*670400292.9);
```

```
 /* Volume - non-dimentional *//*Rplanet = 1; Rcmb = 0.48; Rcrust = 0.9838*/
 /*Volume of mantle & crust = 4/3*pi*(Rplanet^3 - Rcmb^3)*/
  Vmc = (1.333)*3.14*(1-0.110592);
  /*Volume of mantle = 4/3*pi*(Rcrust^3 - Rcmb^3)*/
 Vm = (1.333)*3.14*(0.952183-0.110592);
  /*Volume of crust = 4/3*pi*(Rplanet^3 - Rcrust^3)*/
  Vc = (1.333)*3.14*(1-0.952183);
 /* Partitioning of radioactivity with respect to depth*/
 node = E->ien[m][el].node[1];
 depth = 1.-(E->sx[m][3][node]);

 /*For no partition , remove these */
 if(depth < 0.0162)  /* crust is 55km, so that 2 cubes of 64 comprises the crust,depth
                     is 1-value, so (0-surface) is the actual value (1- 0.9838) =
                     0.0162 is the value for crust*/
 {
 heating = 0.0 * total_heating * (Vmc/Vc); /*Crustal_heating*/
 }
 else
 {
 heating = 1.0 * total_heating * (Vmc/Vm); /*Mantle_heating*/
 }
 /*heating = total_heating; *//*no partitioning*/

 /* construct residual from this information */

/* Bringing melt algorithm into CitcomS - Latent heat*/
element_melt = 0.0;
for(j=1;j<=ends;j++)       {
  node = E->ien[m][el].node[j];
  T = field[m][node];
  R = E->sx[m][3][node];

 for(i=1;i<=vpts;i++)  {
      T_intp[i] += T * E->N.vpt[GNVINDEX(j,i)];
      Radius_intp[i] += (R * E->N.vpt[GNVINDEX(j,i)]);
            }
    }

    /*Initial condition for Totalmelt*/
      GRAV=3.73;

    for(i=1;i<=vpts;i++)  {
      Radius[i] = (1.0 - Radius_intp[i]);/* for depth, zz = 1 - r, same as depth */
      dim_depth = Radius[i]*3390;
      Pressure = ((marsrho*GRAV*dim_depth)*1000)*(1.0e-9);

      /*To calculate the temperature*/
      surf_temperature=220;
      superadiabatic_tempdiff=1600;
      adiabatic_gradient=0.18;

      Temperature1=T_intp[i]*superadiabatic_tempdiff;
      Temperature2=dim_depth*adiabatic_gradient;
```

```
      Temperature=(surf_temperature+Temperature1+Temperature2);

      /*To calculate the melt percentage*/
      P3=Pressure*Pressure*Pressure;
      P2=Pressure*Pressure;
      P1=Pressure;
      A1=0.4863;
      B1=10.025;
      C1=130.17;
      D1=1467.7;
      Tmelt=(A1*P3)-(B1*P2)+(C1*P1)+D1;

      /*To calculate the total melt*/
      if (Temperature > Tmelt)
            Melt[i]=(Temperature-Tmelt)*0.005;
      else
            Melt[i]=0;

      /*Melt[i]= 1.0;*/

      /*To calculate JUST the volume*/
      element_melt += Melt[i]*(dOmega->vpt[i]*(3.8958219e10));/*Correct dimensional
                        value - dOmega->vpt[i] is the non-dimensional volume, 3.8e10 is
                        the dimensional term to make the volume dimentional
                        (4/3*pi*(1-r)3)*/
      time_original = 4.3e9;/*REPEAT*//*We are using a older lithosphere of 250*/
      time = (1.71e11*(E->monitor.elapsed_time+Q0->t_offset));/*REPEAT*/
      Time = time_original-time;
      /* This is how CitcomS calculates the time step we scale dimensionally */
      deltat = (1.71e11*31536000*E->advection.timestep);
      meltrate[i]=(Melt[i])/deltat;

      /*Latent heat changes*/
      L_H = 6.5e5;/*J/Kg*/
      La_he[i]=(L_H)*(meltrate[i]);/*W/kg*/
      Lat_hea[i] = (marsrho * La_he[i]);/*W/m3*/
      Late_heat[i] =(Lat_hea[i]*670400292.9);/*No unit*/
   }

if(diffusion){
  for(j=1;j<=ends;j++) {
 Eres[j]=0.0;
 for(i=1;i<=vpts;i++)
 Eres[j] -=
 PG->vpt[GNVINDEX(j,i)] * dOmega->vpt[i]
         * ((dT[i] + v1[i]*tx1[i] + v2[i]*tx2[i] + v3[i]*tx3[i])*rho*cp
            - heating + Late_heat[i])
         + diff * dOmega->vpt[i] * E->heating_latent[m][el]
         * (GNx->vpt[GNVXINDEX(0,j,i)]*tx1[i]*rtf[3][i] +
            GNx->vpt[GNVXINDEX(1,j,i)]*tx2[i]*sint[i] +
            GNx->vpt[GNVXINDEX(2,j,i)]*tx3[i] );
  }
}

else { /* no diffusion term */
```

```
      for(j=1;j<=ends;j++) {
     Eres[j]=0.0;
       for(i=1;i<=vpts;i++)
           Eres[j] -= PG->vpt[GNVINDEX(j,i)] * dOmega->vpt[i]
              * (dT[i] - heating + v1[i]*tx1[i] + v2[i]*tx2[i] + v3[i]*tx3[i]);
       }
     }

    /* See brooks etc: the diffusive term is excused upwinding for
       rectangular elements  */

    /* include BC's for fluxes at (nominally horizontal) edges (X-Y plane) */

    if(FLAGS!=NULL) {
      onedfns=0;
      for(a=1;a<=ends;a++)
    if (FLAGS[m][E->ien[m][el].node[a]] & FBZ) {
        if (!onedfns++) get_global_1d_shape_fn(E,el,&GM,&dGamma,1,m);

    nodes[1] = loc[loc[a].node_nebrs[0][0]].node_nebrs[2][0];
    nodes[2] = loc[loc[a].node_nebrs[0][1]].node_nebrs[2][0];
    nodes[4] = loc[loc[a].node_nebrs[0][0]].node_nebrs[2][1];
    nodes[3] = loc[loc[a].node_nebrs[0][1]].node_nebrs[2][1];

    for(aid=0,j=1;j<=onedvpoints[E->mesh.nsd];j++)
      if (a==nodes[j])
        aid = j;
    if(aid==0)
      printf("%d: mixed up in pg-flux int: looking for %d\n",el,a);

    if (loc[a].plus[1] != 0)
      back_front = 0;
    else back_front = 1;

    for(j=1;j<=onedvpoints[dims];j++)
      for(k=1;k<=onedvpoints[dims];k++)
        Eres[a] += dGamma.vpt[GMVGAMMA(back_front,j)] *
    E->M.vpt[GMVINDEX(aid,j)] * g_1d[j].weight[dims-1] *
    BC[2][E->ien[m][el].node[a]] * E->M.vpt[GMVINDEX(k,j)];
      }
    }

    return element_melt;
}


/* This function filters the temperature field. The temperature above   */
/* Tmax0(==1.0) and Tmin0(==0.0) is removed, while conserving the total */
/* energy. See Lenardic and Kaula, JGR, 1993.                           */
static void filter(struct All_variables *E)
{
    double Tsum0,Tmin,Tmax,Tsum1,TDIST,TDIST1;
    int m,i;
    double Tmax1,Tmin1;
    double *rhocp, sum_rhocp, total_sum_rhocp;
```

```
int lev, nz;

/* min and max temperature for filtering */
const double Tmin0 = 0.0;
const double Tmax0 = 1.0;

Tsum0= Tsum1= 0.0;
Tmin= Tmax= 0.0;
Tmin1= Tmax1= 0.0;
TDIST= TDIST1= 0.0;
sum_rhocp = 0.0;

lev=E->mesh.levmax;

rhocp = (double *)malloc((E->lmesh.noz+1)*sizeof(double));
for(i=1;i<=E->lmesh.noz;i++)
    rhocp[i] = E->refstate.rho[i] * E->refstate.heat_capacity[i];

for(m=1;m<=E->sphere.caps_per_proc;m++)
    for(i=1;i<=E->lmesh.nno;i++)  {
        nz = ((i-1) % E->lmesh.noz) + 1;

        /* compute sum(rho*cp*T) before filtering, skipping nodes
           that's shared by another processor */
        if(!(E->NODE[lev][m][i] & SKIP))
            Tsum0 += E->T[m][i]*rhocp[nz];

        /* remove overshoot */
        if(E->T[m][i]<Tmin)  Tmin=E->T[m][i];
        if(E->T[m][i]<Tmin0) E->T[m][i]=Tmin0;
        if(E->T[m][i]>Tmax) Tmax=E->T[m][i];
        if(E->T[m][i]>Tmax0) E->T[m][i]=Tmax0;

    }

/* find global max/min of temperature */
MPI_Allreduce(&Tmin,&Tmin1,1,MPI_DOUBLE,MPI_MIN,E->parallel.world);
MPI_Allreduce(&Tmax,&Tmax1,1,MPI_DOUBLE,MPI_MAX,E->parallel.world);

for(m=1;m<=E->sphere.caps_per_proc;m++)
    for(i=1;i<=E->lmesh.nno;i++)  {
        nz = ((i-1) % E->lmesh.noz) + 1;

        /* remvoe undershoot */
        if(E->T[m][i]<=fabs(2*Tmin0-Tmin1))   E->T[m][i]=Tmin0;
        if(E->T[m][i]>=(2*Tmax0-Tmax1))   E->T[m][i]=Tmax0;

        /* sum(rho*cp*T) after filtering */
        if (!(E->NODE[lev][m][i] & SKIP))  {
            Tsum1 += E->T[m][i]*rhocp[nz];
            if(E->T[m][i]!=Tmin0 && E->T[m][i]!=Tmax0) {
                sum_rhocp += rhocp[nz];
            }

        }
```

```
        }

    /* find the difference of sum(rho*cp*T) before/after the filtering */
    TDIST=Tsum0-Tsum1;
    MPI_Allreduce(&TDIST,&TDIST1,1,MPI_DOUBLE,MPI_SUM,E->parallel.world);
    MPI_Allreduce(&sum_rhocp,&total_sum_rhocp,1,MPI_DOUBLE,MPI_SUM,E->parallel.world);
    TDIST=TDIST1/total_sum_rhocp;

    /* keep sum(rho*cp*T) the same before/after the filtering by distributing
       the difference back to nodes */
    for(m=1;m<=E->sphere.caps_per_proc;m++)
        for(i=1;i<=E->lmesh.nno;i++)   {
            if(E->T[m][i]!=Tmin0 && E->T[m][i]!=Tmax0)
                E->T[m][i] +=TDIST;
        }

    free(rhocp);
    return;
}


static void process_visc_heating(struct All_variables *E, int m,
                                 double *heating)
{
    void strain_rate_2_inv();
    int e, i;
    double visc, temp;
    float *strain_sqr;
    const int vpts = VPOINTS3D;

    strain_sqr = (float*) malloc((E->lmesh.nel+1)*sizeof(float));
    temp = E->control.disptn_number / E->control.Atemp / vpts;

    strain_rate_2_inv(E, m, strain_sqr, 0);

    for(e=1; e<=E->lmesh.nel; e++) {
        visc = 0.0;
        for(i = 1; i <= vpts; i++)
            visc += E->EVi[m][(e-1)*vpts + i];

        heating[e] = temp * visc * strain_sqr[e];
    }

    free(strain_sqr);

    return;
}


static void process_adi_heating(struct All_variables *E, int m,
                                double *heating)
{
    int e, ez, i, j;
    double matprop, temp1, temp2;
```

```
    const int ends = ENODES3D;

    temp2 = E->control.disptn_number / ends;
    for(e=1; e<=E->lmesh.nel; e++) {
        ez = (e - 1) % E->lmesh.elz + 1;
        matprop = 0.125
            * (E->refstate.thermal_expansivity[ez] +
               E->refstate.thermal_expansivity[ez + 1])
            * (E->refstate.rho[ez] + E->refstate.rho[ez + 1])
            * (E->refstate.gravity[ez] + E->refstate.gravity[ez + 1]);

        temp1 = 0.0;
        for(i=1; i<=ends; i++) {
            j = E->ien[m][e].node[i];
            temp1 += E->sphere.cap[m].V[3][j]
                * (E->T[m][j] + E->control.surface_temp);
        }

        heating[e] = matprop * temp1 * temp2;
    }

    return;
}


static void latent_heating(struct All_variables *E, int m,
                           double *heating_latent, double *heating_adi,
                           float **B, float Ra, float clapeyron,
                           float depth, float transT, float inv_width)
{
    double temp, temp0, temp1, temp2, temp3, matprop;
    int e, ez, i, j;
    const int ends = ENODES3D;

    temp0 = 2.0 * inv_width * clapeyron * E->control.disptn_number * Ra / E-
>control.Atemp / ends;
    temp1 = temp0 * clapeyron;

    for(e=1; e<=E->lmesh.nel; e++) {
        ez = (e - 1) % E->lmesh.elz + 1;
        matprop = 0.125
            * (E->refstate.thermal_expansivity[ez] +
               E->refstate.thermal_expansivity[ez + 1])
            * (E->refstate.rho[ez] + E->refstate.rho[ez + 1])
            * (E->refstate.gravity[ez] + E->refstate.gravity[ez + 1]);

        temp2 = 0;
        temp3 = 0;
        for(i=1; i<=ends; i++) {
            j = E->ien[m][e].node[i];
            temp = (1.0 - B[m][j]) * B[m][j]
                * (E->T[m][j] + E->control.surface_temp);
            temp2 += temp * E->sphere.cap[m].V[3][j];
            temp3 += temp;
        }
```

```
        /* correction on the adiabatic cooling term */
        heating_adi[e] += matprop * temp2 * temp0;

        /* correction on the DT/Dt term */
        heating_latent[e] += temp3 * temp1;
    }
    return;
}


static void process_latent_heating(struct All_variables *E, int m,
                                   double *heating_latent, double *heating_adi)
{
    int e;

    /* reset */
    for(e=1; e<=E->lmesh.nel; e++)
        heating_latent[e] = 1.0;

    if(E->control.Ra_410 != 0.0) {
        latent_heating(E, m, heating_latent, heating_adi,
                       E->Fas410, E->control.Ra_410,
                       E->control.clapeyron410, E->viscosity.z410,
                       E->control.transT410, E->control.inv_width410);

    }

    if(E->control.Ra_670 != 0.0) {
        latent_heating(E, m, heating_latent, heating_adi,
                       E->Fas670, E->control.Ra_670,
                       E->control.clapeyron670, E->viscosity.zlm,
                       E->control.transT670, E->control.inv_width670);
    }

    if(E->control.Ra_cmb != 0.0) {
        latent_heating(E, m, heating_latent, heating_adi,
                       E->Fascmb, E->control.Ra_cmb,
                       E->control.clapeyroncmb, E->viscosity.zcmb,
                       E->control.transTcmb, E->control.inv_widthcmb);
    }


    if(E->control.Ra_410 != 0 || E->control.Ra_670 != 0.0 ||
       E->control.Ra_cmb != 0) {
        for(e=1; e<=E->lmesh.nel; e++)
            heating_latent[e] = 1.0 / heating_latent[e];
    }

    return;
}


static double total_heating(struct All_variables *E, double **heating)
{
```

```
    int m, e;
    double sum, total;

    /* sum up within each processor */
    sum = 0;
    for(m=1; m<=E->sphere.caps_per_proc; m++) {
        for(e=1; e<=E->lmesh.nel; e++)
            sum += heating[m][e] * E->eco[m][e].area;
    }

    /* sum up for all processors */
    MPI_Allreduce(&sum, &total, 1,
                  MPI_DOUBLE, MPI_SUM, E->parallel.world);

    return total;
}

static void process_heating(struct All_variables *E, int psc_pass_1)
{
    int m;
    double total_visc_heating, total_adi_heating;

    for(m=1; m<=E->sphere.caps_per_proc; m++) {
        if(psc_pass_1 == 0) {
            /* visc heating does not change between psc_pass_1, compute only
             * at first psc_pass_1 */
            process_visc_heating(E, m, E->heating_visc[m]);
        }
        process_adi_heating(E, m, E->heating_adi[m]);
        process_latent_heating(E, m, E->heating_latent[m], E->heating_adi[m]);
    }

    /* compute total amount of visc/adi heating over all processors
     * only at last psc_pass_1 */
      if(psc_pass_1 == (E->advection.temp_iterations-1)) {
        total_visc_heating = total_heating(E, E->heating_visc);
        total_adi_heating = total_heating(E, E->heating_adi);

        if(E->parallel.me == 0) {
            fprintf(E->fp, "Step: %d, Total_heating(visc, adi): %g %g\n",
                    E->monitor.solution_cycles,
                    total_visc_heating, total_adi_heating);
            fprintf(stderr, "Step: %d, Total_heating(visc, adi): %g %g\n",
                    E->monitor.solution_cycles,
                    total_visc_heating, total_adi_heating);
        }
    }

    return;
}

    /* function to implement cooling core boundary */

    void cmb_temperature_bc(struct All_variables *E, struct SOURCES *Q0)
    {
```

```
        int i, j, k, m, node;
        int nox, noy, noz;
        double r1, rout, rin;
        double mytime_original, mytime, Time, tcmb, delta_t;
        const double e_4=1.0e-4;

        noy = E->lmesh.noy;
        nox = E->lmesh.nox;
        noz = E->lmesh.noz;
        rout = E->sphere.ro;
        rin = E->sphere.ri;

        delta_t = 0.15/(1.0-exp(1.0)); /*non dimensional temperature at present day */
        mytime_original = 4.3e9;
        mytime = (1.71e11*(E->monitor.elapsed_time+Q0->t_offset));
        Time = mytime_original-mytime;

        for(m=1;m<=E->sphere.caps_per_proc;m++)
         for(i=1;i<=noy;i++)
            for(j=1;j<=nox;j++)
              for(k=1;k<=noz;k++)  {
                 node=k+(j-1)*noz+(i-1)*nox*noz;
                  /*Since we are starting from 4.3e9 year*/
                  tcmb = 0.992-delta_t*(1.0-exp(1.0-Time/mytime_original));
                  r1 = E->sx[m][3][node];
                  /*if((fabs(r1 - rout) < e_4) || (fabs(r1 - rin) < e_4)){*/
                  if((fabs(r1 - rin) < e_4)){
                      E->sphere.cap[m].TB[3][node]= tcmb;

                  if((fabs(r1 - rout) < e_4)) {
                  /* at bottom or top of box, assign as TBC */
                  /*E->sphere.cap[m].TB[1][node]=E->T[m][node];
                  E->sphere.cap[m].TB[2][node]=E->T[m][node];*/
                  E->sphere.cap[m].TB[3][node]=E->T[m][node];
                       }
                    }
            }

   return;
}
```

Appendix B

The non-Newtonian rheology used in the finite element code CitcomS for Chapter 4 is given below:

Rayleigh number is given by (*Barr et al, 2004*),

$$Ra = \frac{\rho g \alpha \Delta T D^{(n+2)/n}}{(\kappa d^p A^{-1})^{1/n} exp\left(\frac{Q^*}{nRT_m}\right)} \tag{1}$$

Rearranging the terms,

$$Ra = \frac{\rho g \alpha \Delta T D D^{2/n}}{\kappa^{1/n} (\frac{d^p}{A})^{1/n} exp\left(\frac{Q^*}{nRT_m}\right)} \tag{2}$$

Dividing the numerator and denominator by $D^{2/n}$ and multiplying the numerator and denominator by D^2/κ

$$Ra = \frac{\rho g \alpha \Delta T D \frac{D^2}{\kappa}}{\left(\frac{\kappa}{D^2}\right)^{1/n} \frac{D^2}{\kappa} (\frac{d^p}{A})^{1/n} exp\left(\frac{Q^*}{nRT_m}\right)} \tag{3}$$

Rearranging the above equation, we get

$$Ra = \frac{\rho g \alpha \Delta T \frac{D^3}{\kappa}}{\left(\frac{\kappa}{D^2}\right)^{(1-n)/n} (\frac{d^p}{A})^{1/n} exp\left(\frac{Q^*}{nRT_m}\right)} \tag{4}$$

This is the form of Rayleigh number implemented in the non-Newtonian rheology in CitcomS.